UAB
Universitat Autònoma de Barcelona

Testing General Relativity Across Scales with Gravitational Waves with LIGO–Virgo–Kagra

Giada Caneva Santoro

Testing General Relativity Across Scales with Gravitational Waves with LIGO-Virgo-Kagra Data

Environments, Black Hole Spectroscopy and Cosmology

Giada Caneva Santoro

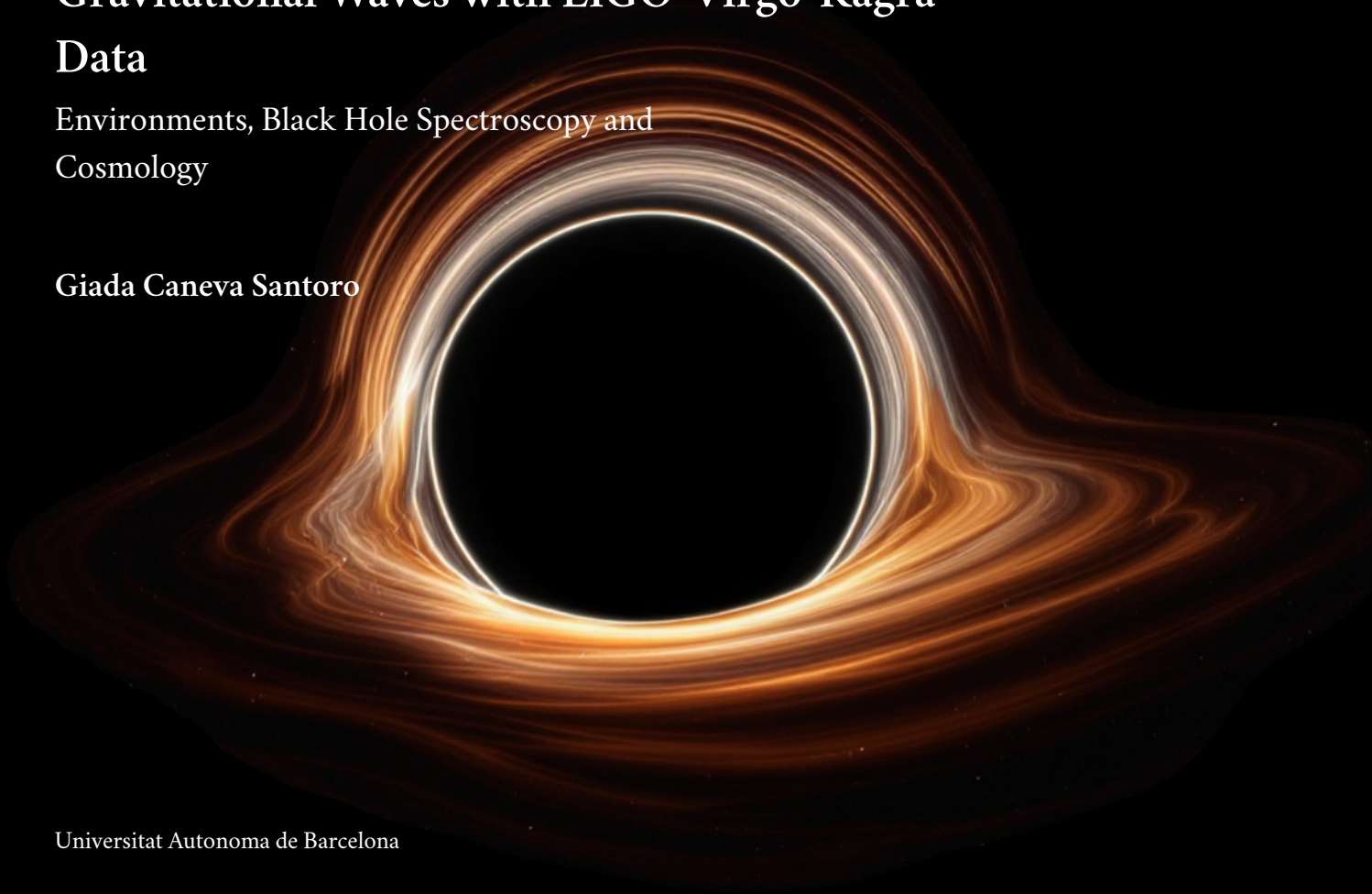

Universitat Autonoma de Barcelona

Barcelona, October 2025

Universitat Autònoma de Barcelona

Testing General Relativity Across Scales with Gravitational Waves with LIGO-Virgo-Kagra Data

Environments, Black Hole Spectroscopy and Cosmology

Giada Caneva Santoro

Supervisor: Mario Martinez

Universitat Autonoma de Barcelona

Dissertation

Barcelona, October 2025

Testing General Relativity Across Scales with Gravitational Waves with LIGO-Virgo-Kagra Data

Preparation of this work was facilitated by the use of the *IPLeiria-Thesis* template.

« Nous voulons, tant ce feu nous brûle le cerveau,
Plonger au fond du gouffre, Enfer ou Ciel, qu'importe ?
Au fond de l'Inconnu pour trouver du nouveau! »

— Charles Baudelaire, *Le Voyage*

Introduction and Thesis Overview

This thesis presents a cohesive body of work at the intersection of gravitational-wave (GW) astronomy and fundamental physics. The direct detection of GWs has provided a new laboratory for testing general relativity (GR) in the strong-field, dynamical regime. The research contained herein leverages the growing catalog of GW events to perform three distinct but complementary tests: probing the astrophysical environments of compact binaries, performing black hole spectroscopy via ringdown signals, and constraining cosmological modifications to gravity.

The structure of this thesis reflects this progression from validating foundational assumptions to exploring the frontiers of our theoretical understanding.

Chapter 1 establishes the theoretical foundation, reviewing the prediction of GWs and black holes in GR, the dynamics of compact binary coalescences, and the expanding universe, which form the bedrock upon which all subsequent data analysis rests.

Chapter 2 and Chapter 3 establish the essential experimental and methodological groundwork, detailing the principles of interferometric GW detection and the sophisticated statistical methods, such as matched filtering and Bayesian inference, used to extract faint signals from noisy data and infer source properties.

The original research begins in Chapter 4, which addresses a key assumption in GW modeling: that binaries evolve in isolation. This chapter presents a model-agnostic, Bayesian search for environmental effects like dynamical friction and accretion in LIGO-Virgo data. The null result, yielding the first upper limits on ambient density from an event catalog study, is published as *"First Constraints on Compact Binary Environments from LIGO-Virgo Data"* [1, 2].

Chapter 5 focuses on the final state of binary black hole mergers, using the ringdown phase to perform black hole spectroscopy. The analysis follows the data analysis framework for ringdown signals, as comprehensively reviewed in *Black hole spectroscopy: from theory to experiment"* [3]. The systematic analysis of the O4a dataset, which forms the event catalog basis for the tests in this chapter, is part of the LIGO-Virgo-KAGRA collaboration paper *Tests of GR with GWTC-4 III. Tests of the Remnants"* [4]. My application of this framework, which led to the first confident multi-mode detection in GW250114 and precision tests of the Kerr metric and Hawking's area law, resulted in

the publications *Black Hole Spectroscopy and Tests of General Relativity with GW250114"* and *GW250114: Testing Hawking's Area Law and the Kerr Nature of Black Holes"* [5, 6]. Investigations of special events GW230814 and GW231123 presented here also contributed to [7, 8].

Finally, Chapter 6 extends the tests of GR to cosmological scales. Using a hierarchical Bayesian framework implemented in the `icarogw` package [9], this chapter constrains theories of modified gravity by comparing the GW-inferred luminosity distance to the electromagnetic distance from galaxy catalogs, placing limits on parameters that describe a running Planck mass and extra-dimensional scenarios. This work has been published as [10].

The concluding chapter, Chapter 7, synthesizes these findings, highlighting the consistent agreement with GR across all probes and outlining the promising future of fundamental physics with next-generation GW observatories.

The methodologies developed and applied throughout this thesis, from environmental searches to ringdown analysis and cosmological inference, provide a robust toolkit for the future, where ever-more-sensitive observations will continue to stress-test our understanding of gravity.

List of Publications

This thesis is based upon the following publications:

- LIGO Scientific Collaboration, Virgo Collaboration, KAGRA Collaboration. "Tests of General Relativity with GWTC-4 III. Tests of the Remnants In preparation
- LIGO Scientific Collaboration, Virgo Collaboration, KAGRA Collaboration. "Black Hole Spectroscopy and Tests of General Relativity with GW250114". In: arXiv:2509.08099 [gr-qc] (2025). [In press]
- A. G. Abac et al. [KAGRA, Virgo, LIGO Scientific Collaborations]. "GW250114: Testing Hawking's Area Law and the Kerr Nature of Black Holes". In: Phys. Rev. Lett. 135.11 (2025), p. 111403. doi: 10.1103/kw5g-d732
- LIGO Scientific Collaboration, VIRGO Collaboration, KAGRA Collaboration. "GW230814: investigation of a loud gravitational-wave signal observed with a single detector". In: arXiv:2509.07348 [gr-qc] (2025). [In press]
- A. G. Abac et al. [LIGO Scientific, VIRGO, KAGRA Collaborations]. "GW231123: a Binary Black Hole Merger with Total Mass 190-265 $M_\odot$". In: arXiv:2507.08219 [astro-ph.HE] (2025). [In press]
- Emanuele Berti et al. "Black hole spectroscopy: from theory to experiment". In: arXiv:2505.23895 [gr-qc] (2025). [In press]
- Melissa Lopez, Giada Caneva Santoro et al. "Ameliorating transient noise bursts in gravitational-wave searches for intermediate-mass black holes". In: Phys. Rev. D 111.10 (2025), p. 103020. doi: 10.1103/PhysRevD.111.103020. arXiv: 2412.17169 [astro-ph.IM]
- Giada Caneva Santoro et al. "First Constraints on Compact Binary Environments from LIGO-Virgo Data". In: Phys. Rev. Lett. 132.25 (2024), p. 251401. doi: 10.1103/PhysRevLett.132.251401. arXiv: 2309.05061 [gr-qc]
- Simone Mastrogiovanni et al. "ICAROGW: A python package for inference of astrophysical population properties of noisy, heterogeneous, and incomplete observations". In: Astron. Astrophys. 682 (2024), p. A167. doi: 10.1051/0004-6361/202347007. arXiv: 2305.17973 [astro-ph.CO]
- Giada Caneva Santoro et al. "First constraints on binary black hole environments with LIGO-Virgo observations". In: PoS EPS-HEP2023 (2024), p. 068. doi: 10.22323/1.449.0068
- Simone Mastrogiovanni et al. "Joint population and cosmological properties in-

ference with gravitational waves standard sirens and galaxy surveys". In: Phys. Rev. D 108.4 (2023), p. 042002. doi: 10.1103/PhysRevD.108.042002. arXiv: 2305.10488 [astro-ph.CO]

Contents

This page intentionally left blank.

This page intentionally left blank.

This page intentionally left blank.

1

GR: Predictions and Tests

1.1 Gravitational Waves

1.1.1 Linearised Theory of Spacetime Dynamics

GWs are perturbations of spacetime, predicted by GR, which propagate at the speed of light and carry energy and information about dynamical systems. Unlike electromagnetic radiation, whose leading contribution comes from a varying dipole moment, GWs arise from the time variation of the mass-energy quadrupole. This reflects the tensorial nature of gravity, where spacetime curvature, rather than a force, mediates the interaction.

The theoretical framework for GW generation follows from considering small perturbations of a background spacetime within Einstein's field equations [11]:

$$G_{\mu\nu} = \frac{8\pi G}{c^4} T_{\mu\nu}. \tag{1.1}$$

Here, $G_{\mu\nu}$ is the Einstein tensor, defined as $G_{\mu\nu} = R_{\mu\nu} - \frac{1}{2} g_{\mu\nu} R$, where $R_{\mu\nu}$ is the Ricci curvature tensor and R is the Ricci scalar, $T_{\mu\nu}$ is the stress-energy tensor, G is Newton's constant, and c is the speed of light.

In the weak-field limit, where the gravitational field is weak, the spacetime metric can be treated as a small perturbation about the flat Minkowski metric [12]:

$$g_{\mu\nu} = \eta_{\mu\nu} + h_{\mu\nu}, \tag{1.2}$$

where $\eta_{\mu\nu} = \mathrm{diag}(-1, 1, 1, 1)$ and $|h_{\mu\nu}| \ll 1$. Substituting this ansatz into Einstein's equations and expanding to first order in $h_{\mu\nu}$ yields the linearized field equations.

The perturbations $h_{\mu\nu}$ are not uniquely defined due to gauge freedom: an infinitesimal coordinate transformation $x^\mu \to x^\mu + \xi^\mu$ modifies the perturbation as $h_{\mu\nu} \to h_{\mu\nu} - \partial_\mu \xi_\nu - \partial_\nu \xi_\mu$ without altering the underlying physics. To extract physical information, one must impose a gauge condition. The harmonic or de Donder gauge, defined by

$\partial^\mu \bar{h}_{\mu\nu} = 0$ with $\bar{h}_{\mu\nu} = h_{\mu\nu} - \frac{1}{2}\eta_{\mu\nu}h$, reduces the linearized Einstein equations to a wave equation of the form

$$\Box \bar{h}_{\mu\nu} = -\frac{16\pi G}{c^4} T_{\mu\nu}, \tag{1.3}$$

where $\Box = \partial_t^2/c^2 - \nabla^2$ is the d'Alembertian operator.

In vacuum regions far from matter sources, the transverse-traceless (TT) gauge provides a particularly useful choice. This gauge is defined by the conditions $h^{\mathrm{TT}}_{0\mu} = 0$ (vanishing time components), $\partial^i h^{\mathrm{TT}}_{ij} = 0$ (transverse condition), and $h^{\mathrm{TT}}_{ii} = 0$ (traceless condition). These conditions eliminate all gauge freedom, leaving two independent components h_+ and $h_\times$, which represent the physical polarization states of GWs. In this gauge, the linearized Einstein equations reduce to a simple wave equation:

$$\Box h^{\mathrm{TT}}_{\mu\nu} = 0. \tag{1.4}$$

This equation admits plane-wave solutions propagating at the speed of light. For a plane wave with wave vector $k^\mu = (\omega/c, \vec{k})$, the linearized field equations yield the dispersion relation $k^\mu k_\mu = 0$, which implies $\omega = \pm|\vec{k}|/c$, confirming that GWs travel at the speed of light.

For a wave traveling along the z-axis, the transversality condition implies that all components with z-dependence vanish in the divergence, leaving only the spatial x-y components as physically meaningful. The tensor perturbation takes the form

$$h^{\mathrm{TT}}_{\mu\nu}(t,z) = h_+(t - z/c)\, e^+_{\mu\nu} + h_\times(t - z/c)\, e^\times_{\mu\nu}. \tag{1.5}$$

The polarization tensors $e^+_{\mu\nu}$ and $e^\times_{\mu\nu}$ are defined with respect to an orthonormal basis $\{\hat{u}, \hat{v}, \hat{k}\}$ normal to the propagation direction. For waves propagating along $\hat{k} = \hat{z}$, we define:

$$e^+_{ij} = \hat{u}_i\hat{u}_j - \hat{v}_i\hat{v}_j \xrightarrow[\hat{k}=\hat{z}]{} \begin{pmatrix} 1 & 0 & 0 \\ 0 & -1 & 0 \\ 0 & 0 & 0 \end{pmatrix}, \tag{1.6}$$

$$e^\times_{ij} = \hat{u}_i\hat{v}_j + \hat{v}_i\hat{u}_j \xrightarrow[\hat{k}=\hat{z}]{} \begin{pmatrix} 0 & 1 & 0 \\ 1 & 0 & 0 \\ 0 & 0 & 0 \end{pmatrix}. \tag{1.7}$$

In matrix form, for propagation along the z-axis, the complete wave perturbation can be expressed as:

$$h^{\mathrm{TT}}_{\mu\nu} = \begin{pmatrix} 0 & 0 & 0 & 0 \\ 0 & h_+ & h_\times & 0 \\ 0 & h_\times & -h_+ & 0 \\ 0 & 0 & 0 & 0 \end{pmatrix} f(t - z/c),$$

where $f(t - z/c)$ represents the waveform profile. The symmetry and traceless conditions ensure that only two independent polarization states survive. The + polarization

distorts a ring of test particles by elongating it along the x-axis while compressing it along the y-axis, whereas the $\times$ polarization produces the same effect rotated by $45°$, as illustrated in Figure 1.1.

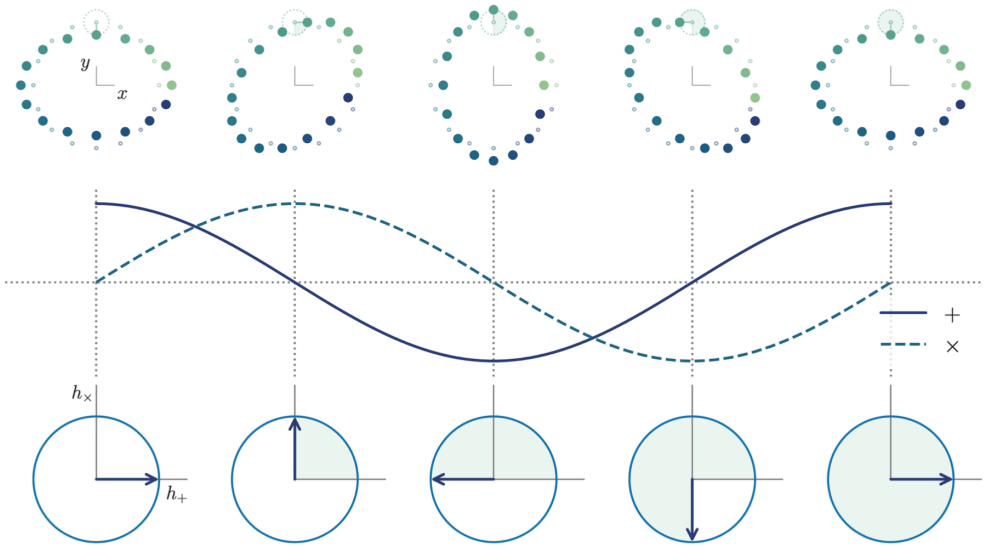

Figure 1.1: *GWs propagating along the z-axis produce distinct oscillatory patterns on test masses arranged in the x-y plane. The visualization tracks these deformations over time (left to right), with the polarization dynamics captured in the lower panel. Amplitude variations for the plus and cross polarization modes are quantified in the middle panel* [13].

1.1.2 Quadrupole Radiation and Energy Loss

Building on the linearized theory of Subsection Section 1.1.1, the generation of GWs is best described by a multipole expansion of the gravitational field.

In the weak-field, slow-motion regime where $v \ll c$, GWs are small perturbations $h_{\mu\nu}$ propagating on a flat Minkowski background. Energy-momentum conservation, $\partial_\nu T^{\mu\nu} = 0$, implies that only the TT part of these perturbations carries radiative energy. Under these assumptions, the far-field solution for the metric perturbation, expressed through retarded Green functions, takes the form

$$\bar{h}_{\mu\nu}(t,\vec{x}) \approx \frac{4G}{c^4 R}\int_V T_{\mu\nu}(t - R/c, \vec{x}')\, d^3x',$$

where R represents the distance from source to observer. The characteristic $1/R$ dependence reflects the expected falloff of a radiative field propagating in three spatial dimensions, distinguishing it from the $1/R^2$ behavior of static gravitational fields.

The connection to the source's mass distribution becomes explicit when the leading term in the multipole expansion is written in terms of the mass quadrupole moment:

$$I_{ij}(t) = \frac{1}{c^2}\int_V T^{00}(t,\vec{x})\, x^i x^j\, d^3x, \quad i,j = 1,2,3. \tag{1.8}$$

This tensor quantifies the deviation of the mass distribution from spherical symmetry. Applying the TT projection to the resulting field yields the quadrupole formula:

$$h_{ij}^{\mathrm{TT}}(t,R) = \frac{2G}{c^4 R}\ddot{I}_{ij}^{\mathrm{TT}}(t - R/c), \tag{1.9}$$

where I_{ij}^{TT} is the transverse-traceless projection of the trace-free mass quadrupole tensor and overdots denote time derivatives.
A full description of gravitational radiation requires not only the wave amplitude but also the energy, momentum, and angular momentum transported by the waves, which backreact on the source through global conservation laws. Although a strictly local gravitational energy density cannot be defined in GR, one can construct an effective stress–energy tensor in the weak-field, short-wavelength (geometric-optics) limit by averaging over several wavelengths:

$$\langle T_{\mu\nu}^{\mathrm{GW}} \rangle = \frac{c^4}{32\pi G}\langle \partial_\mu h_{ij}^{\mathrm{TT}}\, \partial_\nu h_{ij}^{\mathrm{TT}} \rangle,$$

Averaging the resulting energy flux over a sphere surrounding the source leads to the luminosity quadrupole formula (see [12] for a full derivation):

$$\frac{dE}{dt} = -\frac{G}{5c^5}\left\langle \dddot{I}_{ij}^{\mathrm{TT}} \dddot{I}_{ij}^{\mathrm{TT}} \right\rangle. \tag{1.10}$$

The negative sign confirms that the source loses energy as it radiates.
GWs are characteristically weak, which is evident from the prefactor in Equation 1.9. The strain amplitude is suppressed by $G/c^4 \simeq 8\times10^{-50}\,\mathrm{s^2\,g^{-1}\,cm^{-1}}$, necessitating source masses of stellar scale and relativistic velocities to produce a detectable signal.

1.1.3 Compact Binaries as Gravitational Wave Sources

Compact binaries, systems of black holes (BH), neutron stars (NS), or a combination of both, are among the most efficient sources of GWs. They naturally emit strong radiation because their quadrupole moment varies rapidly, and their orbital velocities can approach relativistic values before coalescence[1]. This makes them ideal systems to which the quadrupole formalism developed in Section 1.1.2 can be applied.

[1] To develop intuition for the magnitude of radiated power, consider a generic source characterized by mass M, size r_c, and internal velocity v_c. The quadrupole moment scales as $I \sim Mr_c^2$, leading to a third derivative that scales as $\dddot{I} \sim Mv_c^3/r_c$. Substituting into Equation 1.10 yields

$$\frac{dE}{dt} \sim \frac{G}{5c^5}\frac{M^2 v_c^6}{r_c^2}.$$

For self-gravitating systems where $v_c^2 \sim GM/r_c$, this simplifies to

$$\frac{dE}{dt} \sim \frac{G}{5c^5}\frac{M^5}{r_c^5}.$$

This scaling highlights the importance of compactness: as a system of fixed mass becomes denser (smaller r_c), its GW luminosity grows steeply as r_c^{-5}.

The inspiral phase of a compact binary system is driven by the energy balance between the system's orbital energy and its emission of GWs. For two compact objects of masses m_1 and m_2 in a quasi-circular orbit, the Newtonian orbital energy is given by

$$E_{\rm orb} = -\frac{G\mu M}{2l_0}, \tag{1.11}$$

where $M = m_1 + m_2$ is the total mass, $\mu = m_1 m_2/M$ is the reduced mass, and l_0 is the orbital separation. The GW luminosity in the quadrupole approximation for a binary system is

$$L_{\rm GW} = \frac{32}{5}\frac{G^4}{c^5}\frac{\mu^2 M^3}{l_0^5}.$$

Integrating the energy balance equation $dE_{\rm orb}/dt = -L_{\rm GW}$, yields an evolution equation for $l_0(t)$:

$$l_0(t) = l_{0,\rm in}\left(1 - \frac{t}{t_c}\right)^{1/4}, \quad t_c = \frac{5}{256}\frac{c^5}{G^3}\frac{l_{0,\rm in}^4}{\mu M^2},$$

where t_c is the coalescence time for an initial separation $l_{0,\rm in}$. This solution describes a monotonically shrinking orbit with an accelerating inspiral. The system consequently spends most of its lifetime at large separations, where the orbital evolution is slow. When the binary is embedded in some astrophysical environments, the dissipative interaction with the environment requires an additional term in the energy balance equation. More details will be given in Chapter 4.

The orbital frequency, given by Kepler's law $\Omega_K = \sqrt{GM/l_0^3}$, evolves as

$$\Omega_K(t) = \Omega_{K,\rm in}\left(1 - \frac{t}{t_c}\right)^{-3/8},$$

which corresponds to an orbital period that shortens as $P(t) \propto (t_c - t)^{3/8}$. This accelerating frequency sweep produces a GW signal whose frequency and amplitude both increase with time.

The strain amplitude observed at a distance R is given by

$$h_0(t) = \frac{4G^{5/3}}{c^4}\frac{\mu M^{2/3}(\pi f_{\rm GW})^{2/3}}{R},$$

where $f_{\rm GW} = \Omega_K/\pi$ is the GW frequency (twice the orbital frequency for a circular binary). The inspiral dynamics are primarily governed by the *chirp mass*,

$$\mathcal{M} = \mu^{3/5} M^{2/5},$$

which allows the strain amplitude to be expressed more compactly as

$$h_0(t) = \frac{4(G\mathcal{M})^{5/3}}{c^4}\frac{(\pi f_{\rm GW})^{2/3}}{R}.$$

The phase evolution of the signal is

$$\phi(t) = \phi_c - 2\left(\frac{c^3}{5G\mathcal{M}}\right)^{5/8}(t_c - t)^{5/8}.$$

A measurement of the frequency $f_{\rm GW}$ and its time derivative $\dot{f}_{\rm GW}$ from the chirp waveform thus provides a direct estimate of $\mathcal{M}$, the key mass parameter determining the inspiral dynamics.

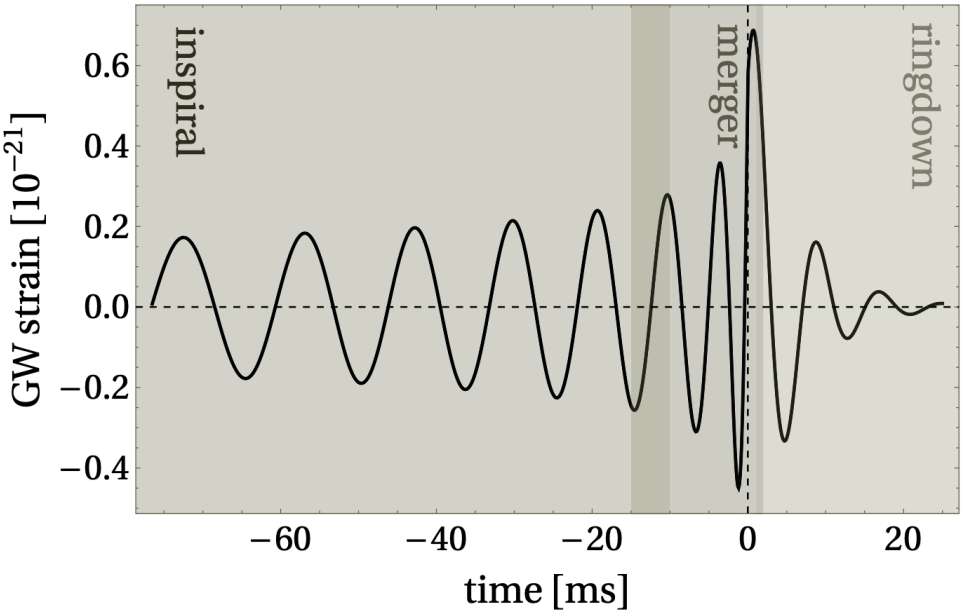

Figure 1.2: *Illustrative GW signal from a coalescing BH binary. The signal evolves through three characteristic phases: inspiral (left shaded region), where the orbital frequency and amplitude increase; merger (central shaded region), the highly dynamical coalescence; and ringdown (right shaded region), where the final remnant oscillates and relaxes to equilibrium. The boundaries between phases are approximate due to the non-linear dynamics in the final stages of coalescence* [12].

As the binary tightens and the orbital velocity v/c increases, higher-order post-Newtonian (PN) corrections to the quadrupole formalism become significant. These corrections imprint detailed physical information onto the waveform's phase, such as the mass ratio, individual component spins, and, in the case of NS, tidal deformabilities. A detailed discussion of the PN framework and its application in testing for beyond-GR scenarios, where specific PN terms capture deviations from the vacuum GR predictions, will be presented in Chapter 4. However, as the system approaches the innermost stable circular orbit (ISCO), the PN expansion breaks down, necessitating numerical relativity simulations to model the subsequent merger phase.

This merger begins when the separation reaches a few gravitational radii, marking a transition into a highly dynamical, strong-field regime. Numerical solutions of Einstein's equations reveal that this phase generates the highest-amplitude GWs. The final stage is the *ringdown*, where the remnant, a single, highly perturbed BH, settles into a stationary state by emitting damped oscillations at its characteristic quasi-normal mode

(QNM) frequencies. Since these frequencies and damping times depend uniquely on the mass and spin of the final BH, their measurement enables BH spectroscopy, providing a direct test of the no-hair theorem. The theoretical framework for this spectroscopy is developed in the next section, with its application to testing fundamental physics detailed in Chapter 5.

Accurately modeling this full sequence of dynamics is fundamental for detecting and interpreting GW signals, and will be described in depth in Chapter 3.

1.2 Theoretical Frameworks for Gravitational Wave Modeling

The accurate modeling of GWs from compact binary coalescence presents substantial theoretical challenges due to the absence of exact analytical solutions to the two-body problem in GR. Multiple complementary approaches have been developed, each valid in different physical regimes and together providing coverage across the entire parameter space of binary systems. These methodologies range from perturbative analytical expansions to full numerical solutions of Einstein's equations, with hybrid approaches bridging the gaps between them.

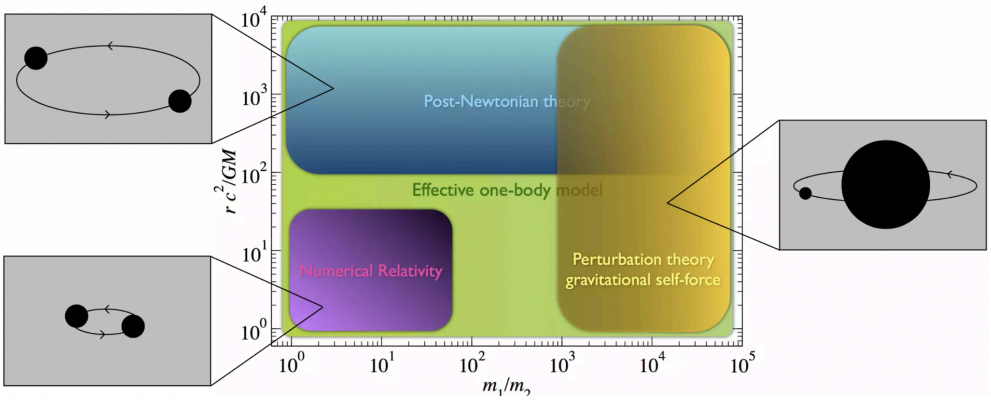

Figure 1.3: *Parameter space coverage of different gravitational waveform modeling approaches. The vertical axis represents orbital separation (related to orbital velocity), showing that post-Newtonian methods are valid for well-separated systems, while numerical relativity captures the highly relativistic merger regime. The horizontal axis shows mass ratio, with perturbation theory applicable for extreme mass ratios and effective-one-body formalism providing coverage across the full parameter space. Adapted from* [14].

As illustrated in Figure 1.3, each waveform modeling approach has its specific domain of validity. Numerical relativity simulations excel in the highly relativistic merger regime but are computationally expensive and typically limited to moderate mass ratios. Post-Newtonian methods provide accurate descriptions during the early inspiral phase when orbits are well-separated but break down as the binary approaches merger. Perturbation theory becomes applicable for extreme mass ratio systems, while the effective-one-body approach offers a unified framework that spans the entire parameter space through analytical insights calibrated to numerical results.

1.2.1 Post-Newtonian Formalism for Inspiralling Binaries

The post-Newtonian (PN) formalism extends the weak-field approximation introduced in Section 1.1.2 to include relativistic corrections beyond the leading-order quadrupole emission. It provides a systematic expansion of the equations of motion and the emitted gravitational radiation in powers of the small parameter [15]

$$\epsilon \sim \frac{v^2}{c^2} \sim \frac{GM}{rc^2} \ll 1, \tag{1.12}$$

where v is the characteristic orbital velocity, M the total mass, and r the orbital separation of the binary system.

In harmonic gauge, the field equations (see Equation 1.3) can be rewritten in the relaxed form

$$\Box h^{\mu\nu} = \frac{16\pi G}{c^4}\,\tau^{\mu\nu}, \tag{1.13}$$

where the effective stress–energy pseudo-tensor

$$\tau^{\mu\nu} = |g|T^{\mu\nu} + \frac{c^4}{16\pi G}\Lambda^{\mu\nu}$$

includes both the matter contribution $T^{\mu\nu}$ and the gravitational self-interaction terms $\Lambda^{\mu\nu}$. The PN expansion is then constructed by iteratively, , expanding both$\tau^{\mu\nu}$ and $h^{\mu\nu}$ in powers of ϵ.

The PN expansion is valid in the near zone, where the field varies slowly ($r \ll \lambda_{\mathrm{GW}}$), while the far-zone radiation field can be represented as a multipole expansion in $1/R$. The two regimes are connected through an asymptotic matching procedure in an overlap region, ensuring global consistency of the solution. This multipolar–post-Minkowskian (MPM) framework expresses the radiative field in terms of source multipole moments, which are computed from the PN-expanded energy–momentum distribution.

The relative acceleration of the two compact objects admits a PN expansion of the form

$$\frac{d^2\vec{r}}{dt^2} = \vec{a}_{\mathrm{N}} + \vec{a}_{\mathrm{1PN}} + \vec{a}_{\mathrm{2PN}} + \cdots + \vec{a}_{\mathrm{RR}}, \tag{1.14}$$

where the Newtonian term $\vec{a}_{\mathrm{N}}$ corresponds to Keplerian motion, and $\vec{a}_{\mathrm{RR}}$ denotes radiation–reaction corrections that first appear at 2.5PN order ($\sim \epsilon^{5/2}$). The conservative orbital energy likewise expands as

$$E_{\mathrm{orb}} = E_{\mathrm{N}} + E_{\mathrm{1PN}} + E_{\mathrm{2PN}} + \cdots,$$

and balances with the GW luminosity via

$$\frac{dE_{\mathrm{orb}}}{dt} = -\frac{dE}{dt}.$$

The inspiral phase of a compact binary system follows from the energy balance be-

tween the orbital energy and GW emission. For two compact objects of masses m_1 and m_2 in a quasi-circular orbit, the Newtonian orbital energy and quadrupole luminosity are given by . Equation 1.11 and Equation 1.10, respectively. Integrating the balance equation $dE_{\rm orb}/dt = -L_{\rm GW}$ yields the evolution of the orbital separation $l_0(t)$ and the corresponding coalescence time t_c.

The GW energy flux generalizes the quadrupole luminosity of Equation 1.10 as a PN series:

$$\frac{dE}{dt} = \mathcal{F}_{\rm N} + \mathcal{F}_{\rm 1PN} + \mathcal{F}_{\rm 1.5PN} + \mathcal{F}_{\rm 2PN} + \cdots , \tag{1.15}$$

where the half-integer orders originate from hereditary (non-local-in-time) effects such as tails and memory. Combining the flux and energy expansions through the balance equation yields the PN evolution of the orbital frequency and, consequently, of the GW phase.

For a quasi-circular binary, defining the dimensionless PN parameter

$$x = \left(\frac{GM\Omega_K}{c^3}\right)^{2/3} = \left(\frac{\pi GM f_{\rm GW}}{c^3}\right)^{2/3},$$

and the symmetric mass ratio $\eta = \mu/M$, the GW phase can be written as

$$\phi(f) = \phi_c - \frac{1}{\eta}\left(\pi GMf/c^3\right)^{-5/3}\left[1 + \alpha_2 x + \alpha_3 x^{3/2} + \alpha_4 x^2 + \cdots\right], \tag{1.16}$$

where the coefficients α_i are known PN corrections encoding effects from mass ratio, spins, and tails. In practice, waveform models for compact binaries used in data analysis typically include PN corrections up to 3.5PN order in phase ($\sim \epsilon^{7/2}$).

The PN expansion remains accurate as long as $v/c \lesssim 0.3$, corresponding to the inspiral regime preceding the innermost stable circular orbit (ISCO). Beyond this point, the expansion ceases to converge, and the system must be modeled using numerical relativity or effective-one-body approaches.

1.2.2 Stationary Phase Approximation

In GW data analysis (discussed further in Chapter 3), working with the Fourier-domain representation of the signal is often necessary. Directly computing the Fourier transform of the time-domain waveform is analytically challenging, and numerical evaluation is computationally prohibitive for many applications like parameter estimation. The stationary phase approximation (SPA) provides an efficient analytical method to approximate this Fourier transform.

For a waveform with a 0PN-order amplitude, the plus and cross polarizations are generically given by

$$h_{+,\times}(t) = A_{+,\times}(t)\cos\Phi_{+,\times}(t). \tag{1.17}$$

Their Fourier transforms are defined by the integral

$$\tilde{h}_{+,\times}(f) = \int_{-\infty}^{\infty} A_{+,\times}(t)\cos[\Phi_{+,\times}(t)]\, e^{2\pi i f t}\, dt. \tag{1.18}$$

Rewriting the cosine in terms of complex exponentials yields

$$\tilde{h}_{+,\times}(f) = \frac{1}{2}\int_{-\infty}^{\infty} A_{+,\times}(t)\left[e^{i(2\pi f t - \Phi_{+,\times}(t))} + e^{i(2\pi f t + \Phi_{+,\times}(t))}\right] dt. \tag{1.19}$$

The SPA is based on the observation that the integrand oscillates rapidly, leading to significant cancellation, except in the vicinity of a point t_* where the phase is stationary. This point is defined by the condition that the first derivative of the total phase vanishes. For the second exponential term, this condition is

$$2\pi f = \dot{\Phi}_{+,\times}(t_*) = \pi f_{\rm GW}(t_*). \tag{1.20}$$

The first exponential term has no stationary point and integrates to a negligible value. By expanding the phase to second order around t_* and treating the amplitude $A_{+,\times}(t)$ as slowly varying, the integral can be evaluated as a Gaussian, resulting in the SPA solution:

$$\tilde{h}_{+,\times}(f) \simeq \frac{A_{+,\times}(t_*)}{\sqrt{\ddot{\Phi}_{+,\times}(t_*)}}\, e^{i\Psi_{+,\times}(f)}, \tag{1.21}$$

where the Fourier-domain phase is given by

$$\Psi_{+,\times}(f) = 2\pi f t_* - \Phi_{+,\times}(t_*) - \frac{\pi}{4}. \tag{1.22}$$

The stationary time t_* can be expressed as a function of frequency f using Equation 1.20. The complete phase $\Psi(f)$, known up to 3.5PN order [16, 17, 18], has the general form:

$$\Psi(f) = 2\pi f t_c - \phi_c - \frac{\pi}{4} + \sum_{j=0}^{7}\left[\psi_j + \psi_j^{(l)}\ln f\right] f^{(j-5)/3}, \tag{1.23}$$

where t_c and ϕ_c denote the coalescence time and phase, and the coefficients are defined as

$$\psi_j = \frac{3}{128\eta}(\pi M)^{(j-5)/3}\alpha_j, \tag{1.24}$$

$$\psi_j^{(l)} = \frac{3}{128\eta}(\pi M)^{(j-5)/3}\alpha_j^{(l)}. \tag{1.25}$$

The SPA amplitude depends on $A(t_*)$ and the second derivative of the phase, $\ddot{\Phi}(t_*)$, which is related to the rate of change of the GW frequency:

$$\ddot{\Phi}(t_*) = \pi \dot{f}_{\rm GW}(t_*). \tag{1.26}$$

This frequency derivative can be expressed in terms of the system's energy balance:

$$\dot{f}_{\rm GW}(t) = \frac{df_{\rm GW}}{dt} = \frac{3x}{2\pi M}\frac{dE/dx}{E'(x)}\mathcal{F}(x), \tag{1.27}$$

where $\mathcal{F}(x)$ is the post-Newtonian energy flux (see Equation 1.10).

The resulting SPA waveform, with a 0PN amplitude, is known in the literature as the *TaylorF2* approximant [19, 20] and is extensively used in the analysis of GW data.

1.2.3 The Effective-One-Body Formalism

The Effective-One-Body (EOB) formalism is an analytical approach that combines perturbation theory with post-Newtonian expansion to model the complete evolution of binary systems, from inspiral through merger and ringdown. Developed to provide a unified description of binary dynamics, the EOB approach has been successfully validated against numerical relativity simulations for various scenarios, including the transition from inspiral to merger, estimation of radiated energy, and the full waveform construction [21].

The EOB framework rests on several key components: the conservative two-body dynamics encoded in a Hamiltonian, the radiation-reaction forces driving the inspiral, and the emitted gravitational waveforms. The fundamental idea is to map the real two-body problem onto an effective one-body problem, where a test particle moves in a deformed metric. This approach treats comparable-mass systems as deformations of the test-particle limit, building upon established results from perturbation theory.

In practice, the physical system with masses m_1, m_2 and spins S_1, S_2 is replaced by an effective description where a particle with mass $\mu = m_1 m_2/(m_1 + m_2)$ and effective spin $S_*(S_1, S_2)$ moves in a deformed Kerr-like geometry. This effective metric has mass $M = m_1 + m_2$, spin $S_{\rm Kerr}(S_1, S_2)$, and is parameterized by the symmetric mass ratio $\nu = \mu/M$ (where $\nu = 1/4$ for equal masses), which serves as the deformation parameter.

The mapping between real and effective dynamics can be intuitively understood through a quantum mechanical analogy: rather than considering classical Hamiltonians directly, one can examine the energy levels of quantum bound states corresponding to the Hamiltonian operators. This perspective facilitates the construction of the conservative dynamics within the EOB framework.

Following this mapping, the radiation reaction forces and gravitational waveforms are similarly translated into the effective one-body picture. The merger-ringdown waveform, for instance, incorporates insights from the close-limit approximation, where the transition from two-body to one-body description occurs near the peak of the BH potential barrier. Through these constructions, the EOB approach achieves its primary goal: providing complete analytical waveforms for coalescing binary systems that remain accurate throughout all evolutionary phases.

1.2.4 Numerical Relativity

The analytical methods discussed previously represent decades of work by leading relativists. Numerical relativity (NR) offers a complementary approach by directly solving the Einstein field equations through numerical evolution of the spacetime geometry.

Numerical relativity has matured into a robust field that has seen remarkable progress over the past decades [22, 23, 24]. A pivotal achievement was Pretorius' [25] first successful simulation of a BBH system through multiple orbital cycles. Subsequent developments have focused on improving the stability, efficiency, and accuracy of numerical methods.

The principal strength of NR simulations lies in their solution of the complete Einstein equations without resorting to perturbative expansions. This makes NR an invaluable tool for validating post-Newtonian predictions, particularly during the inspiral phase where different PN approximants begin to diverge. Excellent agreement has been demonstrated between NR and PN waveforms in regimes where both approaches are expected to be reliable. Beyond verification, NR enables exploration of previously inaccessible dynamical regimes, most notably the merger phase and immediate post-merger evolution. Furthermore, NR simulations of the ringdown phase show strong consistency with predictions from BH perturbation theory [26, 27, 28].

However, NR simulations come with significant computational demands. Evolving a dynamical (3+1)-dimensional spacetime requires sophisticated numerical techniques and substantial computational resources, with typical simulations requiring weeks on modern supercomputing systems. While this precludes direct use of NR for GW data analysis, the information from available NR waveforms has been incorporated into hybrid models that enhance and refine analytical PN and EOB approaches. As the parameter space of compact binaries becomes more densely sampled by NR simulations, these hybrid models approach the accuracy of full NR solutions while retaining the computational efficiency of analytical methods. This effort is particularly important for spinning BBH systems, where merger and ringdown signals fall within the sensitive band of advanced detectors like AdVirgo and aLIGO.

For NS binaries, NR simulations have provided crucial insights into matter effects, including tidal deformations, potential disruption of stellar structure, and electromagnetic signatures arising from interacting magnetic fields. Since this dissertation focuses primarily on binary NS (BNS) systems with unknown equations of state, NR-tuned hybrid waveform models will not be employed in the exploratory studies presented here.

1.3 Black Holes

BHs are a fundamental prediction of GR, describing regions of spacetime bounded by an event horizon, a causal boundary from within which no information can escape to distant observers [29]. Notwithstanding their extreme nature, BHs are characterized

by mathematical simplicity, rendering them principal sources within GW astronomy. Understanding the theoretical properties of BHs provides the foundation for interpreting observational data and probing fundamental physics within these astrophysical laboratories.

The theoretical development of BHs spans over a century, from Schwarzschild's 1916 calculation of the first exact solution to Einstein's field equations [30], through the realization by Finkelstein in 1958 of the true nature of the event horizon as a one-way membrane [31], to Kerr's 1963 breakthrough describing rotating BHs [32]. This theoretical development, in conjunction with the no-hair theorem, which posits that stationary BHs in vacuum are completely described by their mass and angular momentum, makes BHs uniquely predictable objects whose GW signatures can be calculated with precision and tested against observations.

1.3.1 The Black Hole Zoo

The simplest BH solution describes a static, spherically symmetric, electrically uncharged object. The Schwarzschild metric in standard Schwarzschild coordinates (t, r, θ, ϕ) takes the form

$$ds^2 = -\left(1 - \frac{r_s}{r}\right) c^2 dt^2 + \left(1 - \frac{r_s}{r}\right)^{-1} dr^2 + r^2 d\Omega^2, \tag{1.28}$$

where $d\Omega^2 = d\theta^2 + \sin^2\theta\, d\phi^2$ represents the metric on the unit 2-sphere, and the Schwarzschild radius[2] is defined as

$$r_s = \frac{2GM}{c^2} = 2.95 \left(\frac{M}{M_\odot}\right) \text{ km}. \tag{1.29}$$

The Schwarzschild metric exhibits two coordinate singularities: one at $r = r_s$, which is a coordinate singularity marking the event horizon, and another at $r = 0$, which is a true curvature singularity. The nature of these singularities differs fundamentally. The event horizon represents merely a coordinate artifact, a boundary beyond which events cannot influence the external universe, through which infalling matter passes smoothly without encountering any local pathology. The singularity at $r = 0$, conversely, represents a genuine breakdown of the spacetime geometry where curvature invariants diverge, signaling the limits of classical GR.

For GW astronomy, the Schwarzschild solution provides the starting point for understanding non-spinning BHs and serves as the basis for perturbation theory analyses that describe how BHs ring down after merger events. The characteristic timescale associated with a Schwarzschild BH is

$$\tau = \frac{r_s}{c} = \frac{2GM}{c^3} = 49.2 \left(\frac{M}{10M_\odot}\right) \mu\text{s}, \tag{1.30}$$

[2] This fundamental length scale sets the size of the BH and marks the location of the event horizon. For a $10M_\odot$ stellar-mass BH, the Schwarzschild radius is approximately 30 km, while for a supermassive BH of $10^6 M_\odot$, it reaches roughly 3×10^6 km, about 5 times the radius of the Sun.

which sets the natural frequency scale for the QNM oscillations that dominate the ringdown phase of binary coalescences.

Astronomical bodies naturally possess angular momentum from their formation and evolution, making rotation a generic feature of astrophysical BHs. The Kerr solution describes the spacetime geometry of a rotating, axisymmetric, stationary BH. In Boyer-Lindquist coordinates (t, r, θ, ϕ), which generalize Schwarzschild coordinates to the rotating case, the Kerr metric reads

$$\begin{aligned} ds^2 = &-\left(1 - \frac{r_s r}{\Sigma}\right) c^2 dt^2 - \frac{r_s r a \sin^2\theta}{\Sigma}(c\, dt\, d\phi + d\phi\, c\, dt) \\ &+ \frac{\Sigma}{\Delta} dr^2 + \Sigma\, d\theta^2 + \frac{\sin^2\theta}{\Sigma}\left[(r^2 + a^2)^2 - \Delta a^2 \sin^2\theta\right] d\phi^2, \end{aligned} \tag{1.31}$$

where the auxiliary functions are defined as

$$\Sigma = r^2 + a^2 \cos^2\theta, \tag{1.32}$$

$$\Delta = r^2 - r_s r + a^2 = r^2 - \frac{2GMr}{c^2} + a^2. \tag{1.33}$$

The parameter a has dimensions of length and is related to the BH's angular momentum J through

$$a = \frac{J}{Mc} = \frac{cJ}{GM}, \tag{1.34}$$

though it proves more convenient to work with the dimensionless spin parameter

$$a_* = \frac{a}{GM/c^2} = \frac{cJ}{GM^2}, \tag{1.35}$$

which satisfies $|a_*| \leq 1$ for physically realistic BHs. The bound $a_* = 1$ corresponds to an extremal Kerr BH rotating at the maximum possible rate consistent with cosmic censorship, while $a_* = 0$ recovers the Schwarzschild solution.

The event horizon of a Kerr BH is located at the outer root of $\Delta = 0$:

$$r_+ = \frac{GM}{c^2}\left(1 + \sqrt{1 - a_*^2}\right) = \frac{r_s}{2}\left(1 + \sqrt{1 - a_*^2}\right). \tag{1.36}$$

For a non-rotating BH ($a_* = 0$), this reduces to $r_+ = r_s$, while for a maximally rotating BH ($a_* = 1$), the horizon shrinks to $r_+ = GM/c^2 = r_s/2$. This dramatic reduction in horizon size for rapidly spinning BHs has important observational consequences, as it allows matter in accretion disks to orbit closer to the BH before plunging inward.

The Kerr solution exhibits several features absent in the Schwarzschild case. The off-diagonal $dt\, d\phi$ term in the metric represents frame dragging, the tendency of a rotating mass to drag spacetime around with it. This effect becomes increasingly important closer to the BH and within a region called the ergosphere, bounded by the event hori-

zon and the surface where $g_{tt} = 0$. Within the ergosphere, no observer can remain stationary with respect to distant stars; all must orbit in the same direction as the BH's rotation.

For GW observations, the Kerr solution is fundamental because astrophysical BHs are expected to be well-described by the Kerr metric with very high precision. The mass M and spin parameter a_* completely determine the spacetime geometry and thus all observable properties of the BH, including its GW emission during inspiral and ringdown. The innermost stable circular orbit (ISCO), which marks the inner edge of accretion disks and sets the final stages of inspiral, has a radius that depends strongly on the spin:

$$r_{\rm ISCO} = \frac{GM}{c^2}\left[3 + Z_2 \mp \sqrt{(3 - Z_1)(3 + Z_1 + 2Z_2)}\right], \tag{1.37}$$

where

$$Z_1 = 1 + (1 - a_*^2)^{1/3}[(1 + a_*)^{1/3} + (1 - a_*)^{1/3}], \tag{1.38}$$

$$Z_2 = \sqrt{3a_*^2 + Z_1^2}, \tag{1.39}$$

and the minus (plus) sign applies to prograde (retrograde) orbits. For a non-rotating BH, $r_{\rm ISCO} = 6GM/c^2$, while for a maximally rotating prograde orbit, it approaches $r_{\rm ISCO} = GM/c^2$, just outside the event horizon.

For completeness, we note the existence of charged BH solutions. The Reissner-Nordström metric [33, 34] describes a static, spherically symmetric BH with electric charge Q, while the Kerr-Newman solution [35] generalizes this to rotating charged BHs. These solutions are characterized by three parameters: mass M, spin angular momentum J, and electric charge Q [36, 37, 38].

However, for astrophysical macroscopic BHs, electric charge is completely negligible and can be safely ignored. Any significant initial charge would be rapidly neutralized through interactions with the highly ionized plasma pervading astrophysical environments. The equilibrium charge-to-mass ratio for a BH in a typical interstellar medium is extraordinarily small, of order $Q/M \sim 10^{-30}$ in geometric units. Consequently, astrophysical BHs are excellently approximated by the Kerr solution with only two parameters: mass and spin.

1.3.2 Stability and Quasi-Normal Modes

A fundamental property of BHs in GR, and in many modified theories of gravity, is their stability against perturbations. When a stationary BH solution is subjected to an external perturbation, the resulting dynamics cause the spacetime to relax back to a stationary BH configuration.

Over six decades of research have established the linear stability of Schwarzschild and Kerr BHs. The pioneering work of Regge and Wheeler [39] developed the formalism

for axial perturbations of the Schwarzschild spacetime, later extended to polar modes by Zerilli [40]. Teukolsky [26] generalized the perturbative framework to rotating Kerr BHs by deriving a separable master equation for massless fields of arbitrary spin. Subsequent analyses have demonstrated that all physical solutions of these equations are damped, providing strong evidence for the linear stability of Schwarzschild and Kerr BHs (with ongoing work addressing the extremal limit).

In the time domain, the evolution of a generic perturbation typically follows a characteristic pattern: an initial prompt response determined by the details of the disturbance is followed by a ringdown phase dominated by exponentially damped oscillations, the QNMs, and a late-time power-law tail arising from backscattering off spacetime curvature. This behavior confirms BHs as dissipative systems, absorbing energy at the horizon and radiating it to infinity as they relax to equilibrium.

The QNMs correspond to the characteristic vibrational modes of the BH. Unlike normal modes of conservative systems, they are damped because the system is open: energy can flow irreversibly into the horizon or radiate to infinity. Consequently, the eigenfrequencies are complex:

$$\omega = \omega_R + i\omega_I, \quad \omega_I < 0,$$

where ω_R sets the oscillation frequency and ω_I the decay rate. In the time domain, a perturbation behaves as

$$h(t) \sim e^{-|\omega_I|t} \cos(\omega_R t + \phi),$$

or a superposition thereof. The discrete spectrum is determined by boundary conditions requiring purely ingoing waves at the horizon and purely outgoing waves at infinity. These conditions ensure the system radiates and absorbs perturbations rather than sustaining them.

A remarkable property of QNMs is that their spectrum depends only on the intrinsic parameters of the BH, in GR, its mass M, spin a, and charge if present. Thus every BH of a given (M, a) a "sounds" the same. Different initial disturbances excite different linear combinations of modes, but the frequencies and damping times themselves are universal. This makes BHs analogous to resonant objects such as bells, whose tone is determined by their shape.

The computation of QNM frequencies relies on BH perturbation theory. The field equations are linearized around the background metric, and symmetries permit a separation of variables into spin-weighted spheroidal harmonics. This reduces the problem to radial master equations, such as those of Regge–Wheeler, Zerilli, or Teukolsky, which take a Schrödinger-like form:

$$\frac{d^2\Psi}{dr_*^2} + \left[\omega^2 - V(r)\right]\Psi = 0,$$

where r_* is the tortoise coordinate. Imposing the physical boundary conditions transforms this into a spectral problem for ω, solvable via continued-fraction methods, WKB

approximations, or numerical integration.
The QNM spectrum serves the same role in BH physics as atomic spectral lines do in atomic physics: it provides a discrete set of characteristic frequencies from which the system's parameters can be inferred. This forms the basis of *BH spectroscopy*, the program of measuring multiple QNMs in the ringdown to infer the BH's mass and spin and to test GR by verifying consistency between modes. A detailed treatment of observational strategies and data analysis methods will be presented in Chapter 3.

1.3.3 The Area Law and Black Hole Thermodynamics

The irreversible nature of BH evolution is codified in the *area theorem*: in any classical process, the total surface area of all event horizons is non-decreasing [41, 42, 43]. This theorem establishes a rigorous gravitational analogue of the second law of thermodynamics, with the horizon area serving as a measure of gravitational entropy and thereby encoding the irreversible character of BH dynamics within GR.
The mathematical structure of BH mechanics can be systematically organized into four laws [44], which formally parallel the laws of classical thermodynamics.
The *zeroth law* states that the surface gravity κ remains constant over the event horizon of any stationary BH in equilibrium. For a Kerr BH characterized by mass M and dimensionless spin parameter a_*, this quantity is given by

$$\kappa = \frac{c^4}{4GM} \frac{\sqrt{1-a_*^2}}{1+\sqrt{1-a_*^2}}, \tag{1.40}$$

which reduces to $\kappa = c^4/(4GM)$ in the Schwarzschild limit ($a_* = 0$) and vanishes in the extremal limit ($a_* \to 1$).
The *first law* establishes a differential relation between variations in the BH mass and changes in its geometric and angular properties:

$$dM = \frac{\kappa c^2}{8\pi G} dA + \Omega_H dJ + \Phi_H dQ, \tag{1.41}$$

where A denotes the horizon area, Ω_H the angular velocity of the horizon, J the angular momentum, Φ_H the electrostatic potential at the horizon, and Q the electric charge. This expression bears a formal resemblance to the first law of thermodynamics, $dE = TdS - pdV + \mu dN$, suggesting the physical identification of surface gravity with temperature and horizon area with entropy.
The *second law* constitutes the area theorem itself:

$$\delta A \geq 0, \tag{1.42}$$

which was rigorously proven by Hawking [42] under the assumption that matter satisfies the null energy condition. This inequality implies that dynamical processes involving BHs, including coalescence events, must result in a total horizon area that exceeds

or equals the sum of the initial areas. For a BBH merger producing a remnant with final mass M_f and spin $a_{*,f}$ from progenitors with areas A_1 and A_2, this constraint takes the explicit form

$$A_f = 16\pi \left(\frac{GM_f}{c^2}\right)^2 \left(1 + \sqrt{1 - a_{*,f}^2}\right) \geq A_1 + A_2. \tag{1.43}$$

This inequality constitutes a fundamental consistency requirement that can be subjected to direct observational test through GW parameter estimation. Current measurements are consistent with this prediction; detailed quantitative constraints will be presented in Chapter 5.

The *third law* prohibits the reduction of surface gravity to zero through any finite sequence of physical processes, thereby establishing an analogue of the unattainability of absolute zero temperature.

The formal analogy between BH mechanics and thermodynamics acquires physical substance when quantum field theory in curved spacetime is incorporated. Hawking's calculation [43] demonstrated that BHs emit thermal radiation with a characteristic temperature

$$T_H = \frac{\hbar\kappa}{2\pi k_B c}, \tag{1.44}$$

thereby establishing that the surface gravity is indeed proportional to a physical temperature. This result directly implies the existence of a BH entropy[3], given by the Bekenstein-Hawking formula [45]:

$$S_{\rm BH} = \frac{k_B c^3 A}{4G\hbar}. \tag{1.45}$$

The area theorem provides a fundamental explanation for the irreversibility inherent in gravitational collapse and BH dynamics. During BBH mergers, although a substantial fraction of the system's initial mass-energy is radiated away as GWs, the second law ensures that the total horizon area, and consequently the gravitational entropy, necessarily increases. This entropy production reflects the conversion of coherent orbital kinetic energy into the incoherent degrees of freedom associated with the horizon geometry.

Any observational evidence for violations of the area theorem, or for systematic deviations from the Bekenstein-Hawking entropy formula, would constitute evidence for physics beyond GR. Such deviations could arise from quantum gravitational corrections, additional conserved charges, or fundamental modifications to Einstein's equations. The precision measurement of masses and spins before and after merger, enabled by GW astronomy, thus provides a unique empirical probe of these foundational aspects of BH physics.

[3] This entropy is remarkably large: for a solar-mass BH, $S_{\rm BH} \sim 10^{77} k_B$, confirming that BHs represent the most entropic macroscopic objects of comparable mass in the observable Universe.

1.4 The Expanding Universe

GR revolutionized the classical notion of spacetime, replacing the idea of a fixed background with a dynamical geometry determined by the distribution of matter and energy. This principle is encapsulated in Einstein's field equations,

$$G_{\mu\nu} + \Lambda g_{\mu\nu} = \frac{8\pi G}{c^4} T_{\mu\nu}, \tag{1.46}$$

where Λ denotes the cosmological constant, corresponding to a uniform energy density that counteracts gravitational attraction on cosmological scales. When these equations are applied under the assumption of large-scale homogeneity and isotropy (the *cosmological principle*), they predict that the Universe cannot remain static but must either expand or contract. This theoretical result, first obtained by Friedmann [46] and Lemaître [47], was observationally confirmed by Hubble [48], establishing cosmic expansion as a cornerstone of modern cosmology.

1.4.1 The ΛCDM Model

The ΛCDM model provides the standard theoretical framework describing our expanding Universe. Its foundation is the Friedmann–Lemaître–Robertson–Walker (FLRW) metric, which incorporates spatial homogeneity and isotropy:

$$ds^2 = -c^2 dt^2 + a^2(t) \left[\frac{dr^2}{1 - kr^2} + r^2 d\Omega^2 \right], \tag{1.47}$$

where $a(t)$ is the scale factor, k the spatial curvature ($-1, 0, +1$ for open, flat, and closed geometries), and $d\Omega^2 = d\theta^2 + \sin^2\theta\, d\phi^2$. Comoving coordinates (r, θ, ϕ) remain fixed for observers following the Hubble flow, while their physical (proper) separation increases proportionally to $a(t)$.

The evolution of $a(t)$ follows from Einstein's equations applied to a perfect fluid with energy–momentum tensor $T^\mu_\nu = \mathrm{diag}(-\rho c^2, p, p, p)$. Energy–momentum conservation, $\nabla_\mu T^\mu_\nu = 0$, yields the fluid equation:

$$\dot{\rho} + 3H(t) \left(\rho + \frac{p}{c^2} \right) = 0, \tag{1.48}$$

where $H(t) = \dot{a}/a$ is the Hubble parameter and H_0 its present-day value. Assuming an equation of state $p = w\rho c^2$, the solution is

$$\rho_i \propto a^{-3(1+w_i)}. \tag{1.49}$$

Inserting the FLRW metric into Equation 1.46 yields the Friedmann equations:

$$H^2 = \frac{8\pi G}{3}\rho - \frac{kc^2}{a^2} + \frac{\Lambda c^2}{3}, \tag{1.50}$$

$$\frac{\ddot{a}}{a} = -\frac{4\pi G}{3}\left(\rho + \frac{3p}{c^2}\right) + \frac{\Lambda c^2}{3}. \tag{1.51}$$

Ordinary matter and radiation ($\rho + 3p/c^2 > 0$) decelerate the expansion, while a positive Λ drives acceleration.

From Equation 1.49, matter scales as $\rho_m \propto a^{-3}$, radiation as $\rho_r \propto a^{-4}$, and dark energy remains constant ($\rho_\Lambda = \text{const.}$). Defining the critical density for spatial flatness,

$$\rho_c \equiv \frac{3H^2}{8\pi G}, \tag{1.52}$$

and the density parameters

$$\Omega_m \equiv \frac{\rho}{\rho_c}, \quad \Omega_k \equiv -\frac{kc^2}{a^2H^2}, \quad \Omega_\Lambda \equiv \frac{\Lambda c^2}{3H^2}, \tag{1.53}$$

one obtains the constraint $\Omega_m + \Omega_k + \Omega_\Lambda = 1$.

To connect with observations, we define present-day density parameters $\Omega_{m,0}$, $\Omega_{k,0}$, and $\Omega_{\Lambda,0}$ using H_0 and the current scale factor a_0. The relationship between cosmological redshift and the scale factor is given by:

$$1 + z = \frac{a(t_0)}{a(t_e)}, \tag{1.54}$$

where $a(t_0)$ is the scale factor when light is observed and $a(t_e)$ when it was emitted. For observations made today, this simplifies to $a(t) = 1/(1+z)$.

For a matter-dominated universe, the density scales as $\rho/\rho_0 = 1/a(t)^3$. Substituting this and $a(t) = 1/(1+z)$ into the Friedmann equation yields the dimensionless Hubble parameter:

$$E(z) \equiv \frac{H(z)}{H_0} = \sqrt{\Omega_{m,0}(1+z)^3 + \Omega_{k,0}(1+z)^2 + \Omega_{\Lambda,0}}. \tag{1.55}$$

Observations indicate $\Omega_{m,0} \simeq 0.3$, $\Omega_{\Lambda,0} \simeq 0.7$, and $\Omega_{k,0} \approx 0$, consistent with a spatially flat, accelerating universe. These values define the ΛCDM model: a Universe dominated by dark energy (Λ) with the remaining fraction composed of matter. Despite its minimal set of six parameters, the ΛCDM framework provides a quantitatively accurate description of a wide range of independent observations, including the detailed anisotropy spectrum of the CMB, the characteristic scale of baryon acoustic oscillations, and the growth of large-scale structure.

1.4.2 The Hubble Tension

A key challenge in modern cosmology is the persistent discrepancy between early- and late-time determinations of the Hubble constant H_0, known as the *Hubble tension* [49, 50].
As illustrated in Fig. 1.4, measurements of H_0 can be broadly grouped into two classes. Early-Universe probes such as the *Planck* satellite yield $H_0 = 67.4 \pm 0.5\ \mathrm{km\,s^{-1}\,Mpc^{-1}}$ [51], while local, late-Universe measurements from the SH0ES collaboration give $H_0 = 73.2 \pm 1.3\ \mathrm{km\,s^{-1}\,Mpc^{-1}}$ [52]. The resulting $\sim 5\sigma$ tension may signal unaccounted-for systematics or new physics beyond ΛCDM.

1.4.3 Cosmological Distances and Gravitational-Wave Standard Sirens

Distance Measures in an Expanding Universe

In cosmology, several distance definitions are employed, each tailored to specific observables. For photons traveling along null geodesics in the FLRW metric, the comoving distance is:

$$\chi = \int_0^z \frac{c\,dz'}{H(z')} = \frac{c}{H_0}\int_0^z \frac{dz'}{E(z')}. \tag{1.56}$$

For a flat Universe ($k = 0$), the luminosity distance[4] is

$$d_L(z) = (1+z)\chi = \frac{c(1+z)}{H_0}\int_0^z \frac{dz'}{E(z')}, \tag{1.57}$$

which, in ΛCDM, becomes

$$d_L(z; H_0, \Omega_m) = \frac{c(1+z)}{H_0}\int_0^z \frac{dz'}{\sqrt{\Omega_m(1+z')^3 + (1-\Omega_m)}}. \tag{1.58}$$

This relation encodes the full expansion history of the Universe, making luminosity distance a cornerstone of cosmological inference.
Another fundamental quantity is the comoving volume, V_C. Under the assumptions of isotropy and homogeneity, the matter distribution is approximately uniform in comoving coordinates throughout cosmic evolution. Although galaxy clustering introduces small-scale deviations, these assumptions remain valid on scales larger than about 100 Mpc. The comoving volume element is given by

$$\frac{dV_C}{dz} = \frac{c}{H_0}\frac{1}{E(z)}\left(\frac{c}{H_0}\int_0^z \frac{dz'}{E(z')}\right)^2. \tag{1.59}$$

When normalized, this expression loses its explicit dependence on H_0 and can be used as a prior on galaxy redshift distributions. The empirical connection between redshift and cosmic expansion was first revealed through early spectroscopic observations of

[4] The luminosity distance d_L is defined such that the observed flux F from a source of intrinsic luminosity L follows $F = L/(4\pi d_L^2)$, accounting for both geometric dilution and photon energy redshift.

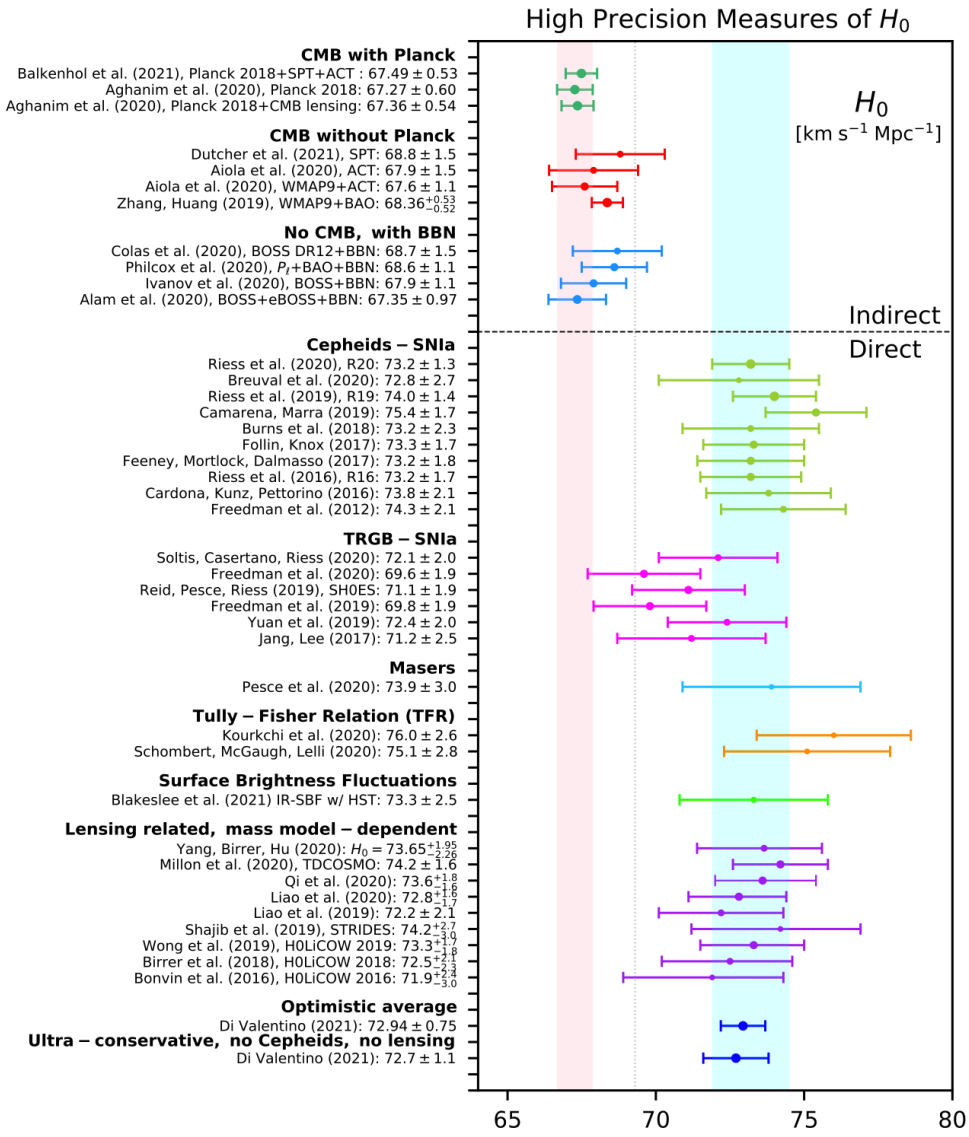

Figure 1.4: *Measurements of the Hubble constant H_0 showing the tension between early and late-Universe probes. The plot displays 68% confidence level constraints from various astronomical missions and groups. The cyan vertical band indicates the value from the SH0ES Team [52] ($H_0 = 73.2 \pm 1.3$ km s^{-1} Mpc^{-1}), representing late-Universe measurements, while the light pink band shows the Planck 2018 result [51] ($H_0 = 67.4 \pm 0.5$ km s^{-1} Mpc^{-1}) derived from early-Universe observations within the ΛCDM framework. This $\sim 5\sigma$ discrepancy constitutes the Hubble tension. Figure adapted from Ref. [53].*

galaxies, whose redshifts were found to increase systematically with distance. The observed redshift is defined as

$$z = \frac{\lambda_{\text{obs}} - \lambda_{\text{emit}}}{\lambda_{\text{emit}}}, \tag{1.60}$$

where λ_{emit} and λ_{obs} are the emitted and observed wavelengths, respectively. For recession velocities $v \ll c$, this relation reduces to

$$z \approx \frac{v}{c}, \tag{1.61}$$

leading, at small redshifts, to the linear Hubble law

$$cz \approx H_0 d_L. \tag{1.62}$$

This relation holds when peculiar velocities are negligible, such that the observed redshift is purely cosmological. In practice, z is measured from spectroscopic or photometric data (after correcting for peculiar motions), while d_L is determined from standard candles.

1.4.4 Gravitational Wave Propagation in FLRW Spacetime

To understand how GWs propagate through an expanding universe, we must generalize the flat spacetime wave equation to curved FLRW spacetime. The d'Alembertian operator $\Box$ in curved spacetime with metric $g_{\mu\nu}$ takes the form:

$$\Box = \frac{1}{\sqrt{-g}} \partial_\mu (\sqrt{-g} g^{\mu\nu} \partial_\nu) \tag{1.63}$$

where g is the determinant of the metric tensor.
The FLRW metric can be conveniently expressed in conformal time η, defined by $d\eta = dt/a(t)$:

$$ds^2 = a^2(\eta)[-c^2 d\eta^2 + dr^2 + r^2 d\Omega^2] \tag{1.64}$$

For GW perturbations h_{ij} propagating on this background, we seek solutions to the wave equation in the form $\phi(r, \eta) = (1/r) f(r, \eta)$. This leads to:

$$\partial_r^2 f - f'' - 2\frac{a'}{a} f' = 0 \tag{1.65}$$

where primes denote derivatives with respect to conformal time. By defining $g(r, \eta) = a(\eta) f(r, \eta)$, the equation simplifies to:

$$\partial_r^2 g - g'' - 2\frac{a''}{a} g = 0 \tag{1.66}$$

For GWs with frequencies satisfying $\omega^2 \gg 1/\eta^2$ (i.e., wavelengths much smaller than the Hubble scale), the last term becomes negligible, and the equation reduces to the

standard wave equation. Solutions take the form:

$$g(\eta, r) \propto e^{\pm i\omega(\eta - r/c)} \tag{1.67}$$

Thus, any function of the form $g(\eta - r/c)$ is a solution, provided its Fourier components satisfy the high-frequency condition. Normalizing with respect to present time t_0, we find:

$$\phi(t, r) = \frac{g(t - r/c)}{a(t_0)} \tag{1.68}$$

The crucial insight is that the GW amplitude scales as $1/[a(t_0)r]$, where the factor $1/a(t_0)$ accounts for the cosmological expansion. This modifies the distance dependence compared to flat spacetime, where the amplitude simply scales as $1/r$.

Gravitational Waves as Standard Sirens

The amplitude scaling derived above leads directly to the concept of GWs as *standard sirens*. Compact binary coalescences offer an independent means of measuring cosmological distances through GW observations. Unlike electromagnetic standard candles, GWs encode absolute distance information directly in their amplitude [54, 55].

For a binary inspiral in flat spacetime, the GW strain is

$$h_0(t) = \frac{4\pi^{2/3} G^{5/3}}{c^4 R} \mathcal{M}^{5/3} (\pi f_{\rm GW}(t))^{2/3}, \tag{1.69}$$

where $\mathcal{M}$ is the chirp mass, $f_{\rm GW}$ the frequency, and R the source distance. In an expanding universe, accounting for the amplitude scaling derived above, the observed strain becomes

$$h_0(t_{\rm obs}) = \frac{4\pi^{2/3} G^{5/3}}{c^4 d_L(z)} (\mathcal{M}^{\rm obs})^{5/3} (\pi f_{\rm GW}^{\rm obs})^{2/3}, \tag{1.70}$$

with $\mathcal{M}^{\rm obs} = \mathcal{M}(1+z)$ and $d_L(z)$ the luminosity distance.

If an electromagnetic counterpart provides the redshift z, the Hubble constant follows directly from the distance-redshift relation:

$$d_L(z) = \frac{c}{H_0} \left[z + \frac{1}{2}(1 - q_0) z^2 + O(z^3) \right]. \tag{1.71}$$

The first such measurement from the BNS merger GW170817 yielded $H_0 = 70^{+12}_{-8}\,\mathrm{km\,s^{-1}\,Mpc^{-1}}$ [56, 57]. Future detections will refine this constraint and may help resolve the Hubble tension discussed in Section 1.4.2.

Moreover, discrepancies between GW- and electromagnetic-based luminosity distances would indicate deviations from GR's propagation laws, a topic explored further in Chapter 6.

Source-Frame vs. Detector-Frame Masses

The cosmological propagation of GWs introduces another crucial subtlety: the distinction between source-frame and detector-frame masses. The redshift affects not just the wave amplitude and frequency, but also the apparent masses of the compact objects. The chirp mass, defined in the source frame as:

$$\mathcal{M}_c = \frac{(m_1^s m_2^s)^{3/5}}{(m_1^s + m_2^s)^{1/5}}, \tag{1.72}$$

appears redshifted in the detector frame. The redshifted chirp mass is:

$$\mathcal{M}_{cz} = (1+z)\mathcal{M}_c(m_1^s, m_2^s) = \mathcal{M}_c(m_1^d, m_2^d) \tag{1.73}$$

This relation shows that the chirp mass measured by GW detectors is not the true source-frame chirp mass, but rather a redshifted version.
The individual component masses are similarly redshifted. We define source-frame masses m_1^s, m_2^s as the true physical masses at the source, and detector-frame masses m_1^d, m_2^d as the apparent masses measured by the detector. These are related by:

$$m_1^d = (1+z)m_1^s, \quad m_2^d = (1+z)m_2^s \tag{1.74}$$

This means that without independent knowledge of the redshift z, GW observations alone cannot distinguish between a nearby low-mass system and a distant high-mass system if they have the same detector-frame masses. This mass-redshift degeneracy is fundamental to GW astronomy.
The detector-frame masses are what we directly measure from GW data because they determine the observed frequency evolution and amplitude. The waveform equations naturally contain these redshifted quantities because the observed frequencies are redshifted ($f_{\rm obs} = f_{\rm source}/(1+z)$), the mass scale that sets the frequency evolution is the redshifted mass, and the amplitude depends on the combination $\mathcal{M}_{cz}/d_L$.
To recover the true physical masses at the source (m_1^s, m_2^s), we need an independent measurement of redshift. Several approaches exist: electromagnetic counterpart identification (as demonstrated with GW170817), statistical association with galaxy catalogs (the *catalog method*), and cosmological inference using population mass distributions (the *spectral siren method*). Both the catalog and spectral siren methods rely on assumptions about the source-frame mass distribution and are detailed in Section 6.2.

1.5 Why Test GR with Gravitational Waves?

Albert Einstein's GR remains one of the most successful theories in modern physics, having withstood all experimental tests across scales ranging from Solar System dynamics to cosmology. Nevertheless, its completeness is challenged by persistent observational. The requirement for dark matter to explain galactic dynamics and the

need for dark energy to account for the Universe's accelerated expansion suggest that our understanding of gravity may be incomplete. Either 95% of the Universe's content is unknown, or GR itself requires modification on certain scales. GW astronomy provides a unique and powerful avenue to address this fundamental dichotomy by probing gravity in its most extreme regime.

The historical validation of GR's radiative properties began with the Hulse-Taylor binary pulsar, whose orbital decay matched the prediction of energy loss to GWs. However, such systems operate in the weak-field, quasi-stationary regime. GW observations, particularly from compact binary coalescences, transcend these limits. They provide a direct window into the strong-field, highly dynamical regime where the gravitational potential approaches $\Phi/c^2 \sim 0.1$ and velocities reach a significant fraction of the speed of light. It is in this unexplored territory, illustrated in Fig. 1.5, that deviations from GR are most likely to manifest.

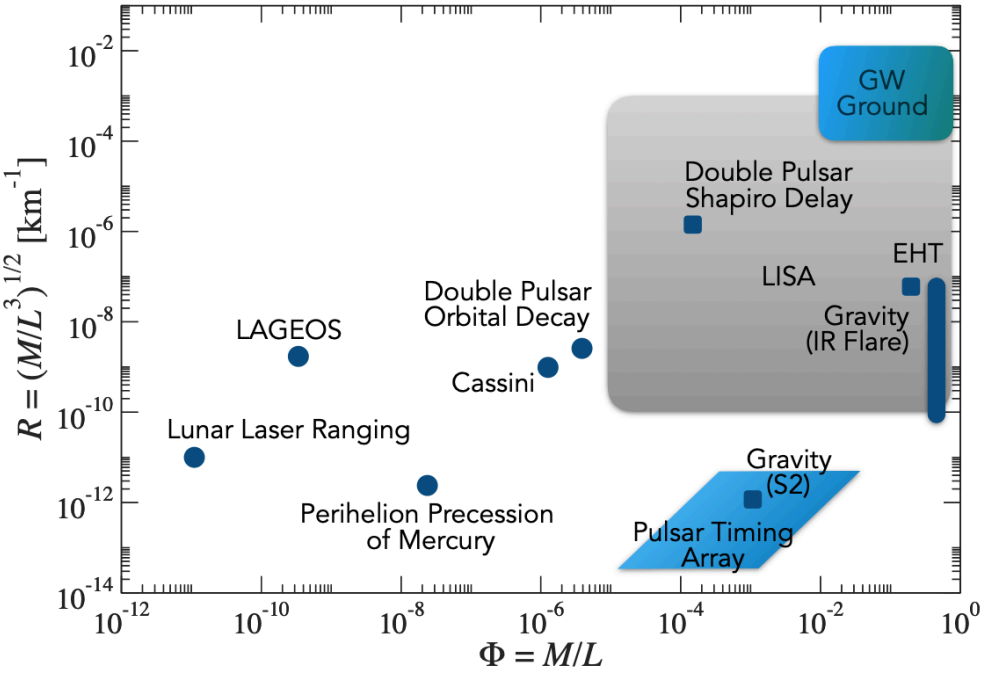

Figure 1.5: *Reach of different gravitational experiments in the space of characteristic spacetime curvature ($\mathcal{R} \sim M/L^3$) and gravitational potential ($\Phi \sim M/L$). For binary systems, the virial theorem relates M/L to v^2/c^2, mapping the orbital velocity to the potential strength. Ground-based GW detectors (e.g., LIGO, Virgo, ET) probe the high-curvature, high-potential regime of merging compact objects, a domain inaccessible to Solar System, binary pulsar, or cosmological tests. Figure taken from [58]*

The utility of GW for fundamental physics is threefold. First, GWs are exceptionally clean messengers: owing to their extremely weak coupling to matter, they propagate virtually unimpeded across cosmological distances and thus retain a faithful imprint of the underlying spacetime dynamics. Second, they directly probe the tensorial degrees of freedom of gravity, which are precisely the sector most commonly altered in extensions of GR. Third, observational milestones such as GW170817 have already delivered stringent, theory-agnostic constraints. The coincident detection of gravitational and

electromagnetic signals from this event established that GWs propagate at the speed of light to within one part in 10^{15}, thereby excluding a wide class of modified gravity models that predict anomalous dispersion or frequency-dependent propagation.

Looking forward, the next generation of detectors will transform this field. High-fidelity waveforms from millions of sources will enable precision tests of the Kerr metric during BH ringdown, searches for additional polarization states, and measurements of any dispersion or attenuation in GW propagation over cosmological distances. Furthermore, as sensitivity increases, our idealized waveforms constructed under the vacuum assumption will begin to break down; the necessity of having models that account for realistic astrophysical environments will become crucial for performing unbiased parameter estimation and the subsequent tests of GR. On the cosmological frontier, the *standard siren* approach, introduced in Section Section 1.4.2, provides a powerful, calibration-free method to measure cosmic expansion. Any discrepancy between the luminosity distance inferred from GWs ($d_L^{\rm GW}$) and that from electromagnetic observations ($d_L^{\rm EM}$) would be a direct signature of modified propagation, offering a novel pathway to resolve the Hubble tension discussed in Section Section 1.4.2.

GW astronomy is not merely a new observational tool; it is a probe of fundamental physics. It allows us to stress-test GR in the strong-field regime, to explore the nature of compact objects, and to measure the geometry of the Universe on large scales. The following chapters of this thesis are dedicated to developing and applying these tests. Chapter 4 will detail how deviations from GR are encoded in the waveform models used for detection and parameter estimation. Chapter 5 will focus on using BH ringdown to perform "BH spectroscopy" and test the no-hair theorem. Finally, Chapter 6 will explore how the cosmological propagation of GWs can be used to constrain theories of modified gravity and dark energy.

2
Principles of GW Detection

2.1 Introduction

GW detectors are among the most precise scientific instruments ever built. They are designed to measure a strain $h \sim 10^{-21}$ induced by passing GWs on a baseline of several kilometers. The basic detection principle relies on measuring differential variations in optical path length between two perpendicular arms using laser interferometry. When a GW passes through the detector, it perturbs the spacetime metric and induces a relative phase shift between the two light beams propagating in the orthogonal directions. This phase shift is then converted into a measurable change in the interference pattern at the photodetector.

The first direct detection of GWs by the LIGO and Virgo collaborations in 2015 marked a milestone in experimental physics, confirming one of the last predictions of Einstein's GR and inaugurating the era of GW astronomy. Modern detectors, such as Advanced LIGO, Advanced Virgo, and KAGRA, are kilometer-scale Michelson interferometers equipped with Fabry–Perot arm cavities, power and signal recycling mirrors, and sophisticated vibration-isolation systems to suppress seismic and thermal noise. Future observatories such as the Einstein Telescope and Cosmic Explorer aim to extend this sensitivity by one or more orders of magnitude through cryogenic operation, underground construction, and advanced quantum noise reduction techniques.

This chapter presents the physical principles that govern interferometric GW detectors. We begin with the general response of light to spacetime perturbations and then discuss the successive developments that have led from the basic Michelson interferometer to the dual-recycled Fabry–Perot configuration used in current observatories. Finally, the principal sources of noise that limit detector sensitivity are summarized.

2.2 Principles of Detection

The purpose of a GW detector is to measure the tiny perturbation in distance ΔL between free-falling test masses induced by the passage of a GW. Since these changes are

extremely small, of order $10^{-18}\,\mathrm{m}$ for kilometer-scale interferometers, direct mechanical measurement is infeasible. Laser interferometry provides a phase-sensitive means of detecting these perturbations by comparing the optical path lengths along two orthogonal arms.

2.2.1 Propagation of Light in a Perturbed Spacetime

The propagation of light in vacuum follows null geodesics in spacetime, meaning the spacetime interval between any two points along its path is zero. For a light ray with separation vector dx^μ between two events, this condition is expressed as:

$$g_{\mu\nu}dx^\mu dx^\nu = 0, \tag{2.1}$$

where $g_{\mu\nu}$ is the metric tensor. In the case of a GW propagating along the z-axis, this equation becomes:

$$0 = c^2dt^2 - dx^2 - dy^2 - dz^2 + 2h_\times dxdy + h_+(dx^2 - dy^2), \tag{2.2}$$

with h_+ and $h_\times$ representing the plus and cross polarization states of the GW.
This formulation reveals that GWs do not alter the direction of light propagation but rather affect the optical path length, as evidenced by the absence of force-like terms in the geodesic equation. For light traveling along the x-axis, the expression simplifies to:

$$0 = c^2dt^2 - dx^2 + h_+dx^2. \tag{2.3}$$

Assuming small amplitude perturbations ($h_+ \ll 1$), this can be approximated as:

$$dx = \pm cdt\left(1 + \frac{1}{2}h_+(t)\right). \tag{2.4}$$

Consider a round-trip light travel experiment where a photon is emitted at time t_0, reflected at distance L, and detected at time t_2. The outward journey gives:

$$L = c(t_1 - t_0) + \frac{1}{2}c\int_{t_0}^{t_1} h_+(u)du, \tag{2.5}$$

while the return journey satisfies:

$$-L = c(t_1 - t_2) - \frac{1}{2}c\int_{t_1}^{t_2} h_+(u)du. \tag{2.6}$$

Combining these expressions and defining $t_2 = t$ as the detection time and $t_0 = t_r$ as the retarded time, we obtain:

$$t_r = t - \frac{2L}{c} + \frac{1}{2}\int_{t_r}^{t} h(u)du. \tag{2.7}$$

To first order in h, this simplifies to:

$$t_r = t - \frac{2L}{c} + \frac{1}{2}\int_{t-2L/c}^{t} h(u)du. \tag{2.8}$$

For a monochromatic GW with frequency $f = \omega/(2\pi)$ and strain amplitude $h(t) = h_0 \cos(\omega t)$, the retarded time relation becomes:

$$t_r = t - \frac{2L}{c} + \frac{h_0 L}{c}\,\mathrm{sinc}(\omega L/c)\cos(\omega(t - L/c)). \tag{2.9}$$

A similar expression applies for light propagation along the y-axis, though with opposite sign in the final term. This demonstrates how GW detection fundamentally relies on measuring the optical time delay between light emission and reception after reflection. This principle forms the basis for modern ground-based interferometric detectors.

2.2.2 Detector Response and Antenna Patterns

The measured GW signal depends not only on the source properties but also on the relative orientation between the source and the detector. For ground-based interferometric detectors like LIGO and Virgo, the antenna patterns quantify how the detector's sensitivity varies with the sky position and polarization of the incoming wave.

Consider an L-shaped interferometer with arms aligned along the $\hat{x}$ and $\hat{y}$ axes. The detector response to a GW with polarization components h_+ and $h_\times$ is given by:

$$h(t) = F_+(\theta, \phi, \psi)h_+(t) + F_\times(\theta, \phi, \psi)h_\times(t), \tag{2.10}$$

where F_+ and $F_\times$ are the antenna pattern functions that depend on the source's sky location (θ, ϕ) and polarization angle ψ. A scheme of the angles is shown in Figure 2.1.

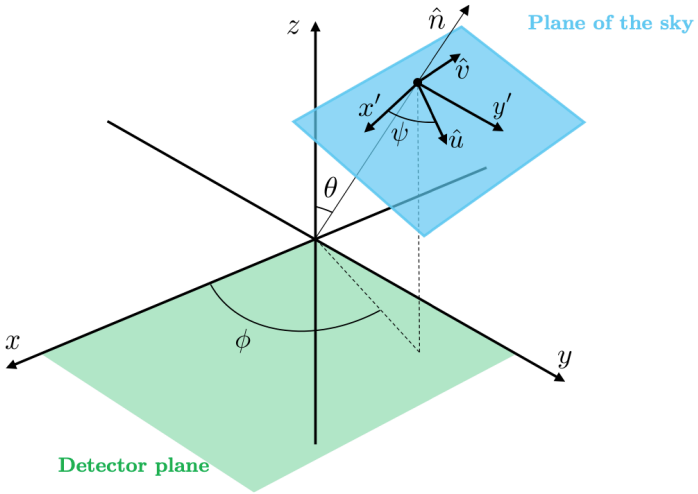

Figure 2.1: *Coordinate systems defining the relative orientation between the GW source and the detector. The angles (θ, ϕ) specify the sky location of the source relative to the detector's arms, while ψ represents the polarization angle that rotates the wave's principal axes. This geometric relationship determines the antenna response functions that modulate the measured signal amplitude.*

The antenna patterns for an L-shaped interferometer are:

$$F_+(\theta,\phi,\psi) = \frac{1}{2}(1+\cos^2\theta)\cos 2\phi\cos 2\psi - \cos\theta\sin 2\phi\sin 2\psi, \tag{2.11}$$

$$F_\times(\theta,\phi,\psi) = \frac{1}{2}(1+\cos^2\theta)\cos 2\phi\sin 2\psi + \cos\theta\sin 2\phi\cos 2\psi. \tag{2.12}$$

These functions satisfy $0 \leq |F_A| \leq 1$ and $F_+^2 + F_\times^2 \leq 1$. The detector is most sensitive when the source is located perpendicular to the detector plane ($\theta = 0, \pi$), where the response reaches its maximum. Conversely, there are blind spots along directions parallel to the detector arms where the antenna response vanishes.

For a compact binary coalescence with inclination angle ι, the total response can be written as:

$$h(t) = F(\theta,\phi,\psi,\iota)A(t)\cos[\Phi(t) - \varphi_P(\theta,\phi,\psi,\iota)], \tag{2.13}$$

where the combined antenna pattern is:

$$F(\theta,\phi,\psi,\iota) = \sqrt{F_+^2(\theta,\phi,\psi)\frac{(1+\cos^2\iota)^2}{4} + F_\times^2(\theta,\phi,\psi)\cos^2\iota}. \tag{2.14}$$

and the polarization phase φ_P accounts for the relative weighting of the two polarization components and is given by:

$$\varphi_P(\theta,\phi,\psi,\iota) = \arctan\left[\frac{F_+(\theta,\phi,\psi)(1+\cos^2\iota)}{4F_\times(\theta,\phi,\psi)\cos\iota}\right]. \tag{2.15}$$

When the source location is unknown, the root-mean-square detector response averaged over all angles is $\sqrt{\langle F^2\rangle} = 2/5$, indicating that the typical sensitivity is 40% of the maximum possible value.

In the frequency domain, particularly within the stationary phase approximation, the detector response modifies the waveform as:

$$\tilde{h}(f) = F(\theta,\phi,\psi,\iota)\tilde{A}(f)e^{i\Psi(f) - i\varphi_P(\theta,\phi,\psi,\iota)}. \tag{2.16}$$

This formulation is essential for parameter estimation, as the antenna patterns introduce degeneracies between the source's intrinsic parameters (masses, spins) and its extrinsic parameters (sky location, orientation).

2.2.3 Michelson Interferometer

The simplest interferometric configuration capable of detecting such time delays is the Michelson interferometer. A schematic layout is shown in Figure 2.2.

A laser source emits monochromatic light at frequency ω_L, with wavenumber $k_L = \omega_L/c$ and wavelength $\lambda_L = 2\pi/k_L$. The electric field of the laser beam is described by:

$$E(t,\vec{x}) = E_0 e^{-i\omega_L t + i\vec{k}_L\cdot\vec{x}}. \tag{2.17}$$

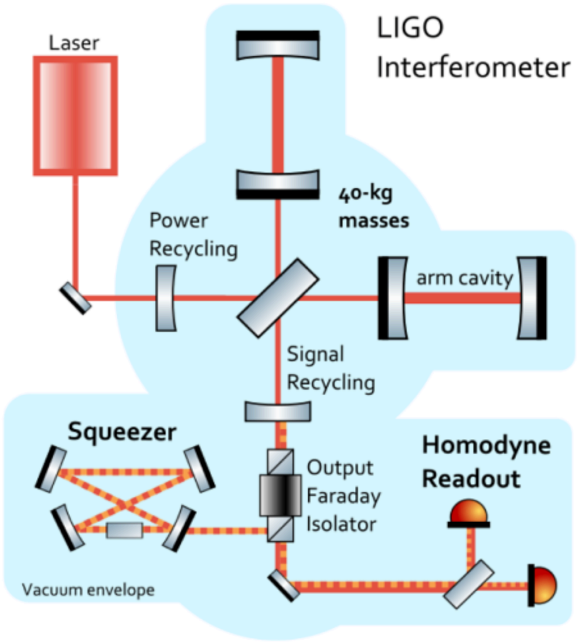

Figure 2.2: *Schematic diagram of a Michelson interferometer. A laser beam is split into two perpendicular arms, reflected by mirrors, and recombined at the beam splitter before detection.*

The interferometer splits the laser beam into two perpendicular arms of lengths L_x and L_y. After reflection from end mirrors, the beams recombine at the beam splitter at time t, having originally been separated at times $t_0^{(x)} = t - 2L_x/c$ and $t_0^{(y)} = t - 2L_y/c$. The returning fields are:

$$E_1 = -\frac{1}{2}E_0 e^{-i\omega_L t + 2ik_L L_x}, \tag{2.18}$$

$$E_2 = \frac{1}{2}E_0 e^{-i\omega_L t + 2ik_L L_y}. \tag{2.19}$$

The superposition at the output port yields:

$$E_{\text{out}} = E_1 + E_2 = -iE_0 e^{-i\omega_L t + ik_L(L_x+L_y)} \sin(k_L(L_y - L_x)), \tag{2.20}$$

$$P_{\text{out}} = |E_{\text{out}}|^2 = E_0^2 \sin^2(k_L(L_y - L_x)). \tag{2.21}$$

This demonstrates the interferometer's sensitivity to differential arm length changes. When accounting for GW effects, the returning fields acquire additional phase modulations:

$$E^{(x)}(t) = -\frac{1}{2}E_0 e^{i\omega_L(t-2L_x/c)+i\Delta\phi_x(t)}, \tag{2.22}$$

$$E^{(y)}(t) = \frac{1}{2}E_0 e^{i\omega_L(t-2L_y/c)+i\Delta\phi_y(t)}, \tag{2.23}$$

where the GW-induced phase shifts are:

$$\Delta\phi_x(t) = h_0 \frac{\omega_L L_x}{c} \operatorname{sinc}(\omega_G L_x/c) \cos(\omega_G(t - L_x/c)), \tag{2.24}$$

$$\Delta\phi_y(t) = -h_0 \frac{\omega_L L_y}{c} \operatorname{sinc}(\omega_G L_y/c) \cos(\omega_G(t - L_y/c)). \tag{2.25}$$

For nearly equal arm lengths $L_x \approx L_y \approx L$, where $L \equiv (L_x + L_y)/2$, the net phase difference becomes:

$$\Delta\phi_{\text{total}}(t) = \Delta\phi_x(t) - \Delta\phi_y(t) \approx 2h_0 \frac{\omega_L L}{c} \operatorname{sinc}(\omega_G L/c) \cos(\omega_G(t - L/c)). \tag{2.26}$$

The total output field and power in the presence of GWs are then:

$$E_{\text{tot}}(t) = E^{(x)}(t) + E^{(y)}(t) = -iE_0 e^{-i\omega_L(t-2L/c)} \sin(\phi_0 + \Delta\phi_x(t)), \tag{2.27}$$

$$P(t) = |E_{\text{tot}}|^2 = P_0 \left[1 - \cos(2\phi_0 + 2\Delta\phi_x(t))\right], \tag{2.28}$$

where $P_0 = |E_0|^2$ is the input power and ϕ_0 represents the operating point phase bias optimized for maximum sensitivity.

The power detected at the output port, given by Equation 2.28, is proportional to the laser power P_0. To maximize the power variation induced by a GW, one should maximize the phase shift $\Delta\phi_x$. This occurs when $\omega_G L/c = \pi/2$, yielding an optimal arm length:

$$L_{\text{opt}} = \frac{\pi c}{2\omega_G}. \tag{2.29}$$

Given that $\omega_G = 2\pi f_{GW}$, this can be rewritten as:

$$L_{\text{opt}} = \frac{c}{4 f_{GW}} \sim 750\,\text{km} \left(\frac{100\,\text{Hz}}{f_{GW}}\right). \tag{2.30}$$

This length scale presents significant technological challenges, motivating modifications to the basic Michelson design to achieve comparable sensitivity with shorter arms. The solution involves incorporating Fabry-Perot cavities in each arm, which resonantly enhance the effective optical path length through multiple reflections.

2.2.4 Fabry-Perot cavity

A Fabry-Perot cavity represents the simplest form of optical resonator, consisting of two partially reflective mirrors separated by a well-defined distance L, as illustrated in **??**perot_schematicfig:fabry_perot_schematic

. The operation of such a cavity relies on the interference of multiple reflected waves between the two mirrors, creating standing wave patterns when specific resonance conditions are met. Consider a Fabry–Perot cavity of physical length L with mirror amplitude reflectivities r_1 and r_2 and transmissivities t_1 and t_2, as shown schematically in **??**perot_schematicfig:fabry_perot_schematic

. For an incident field E_0, the steady-state transmitted and circulating fields are given by:

$$E_{\text{trans}} = \frac{t_1 t_2 e^{ikL}}{1 - r_1 r_2 e^{2ikL}} E_0, \tag{2.31}$$

$$E_{\text{circ}} = \frac{t_1}{1 - r_1 r_2 e^{2ikL}} E_0. \tag{2.32}$$

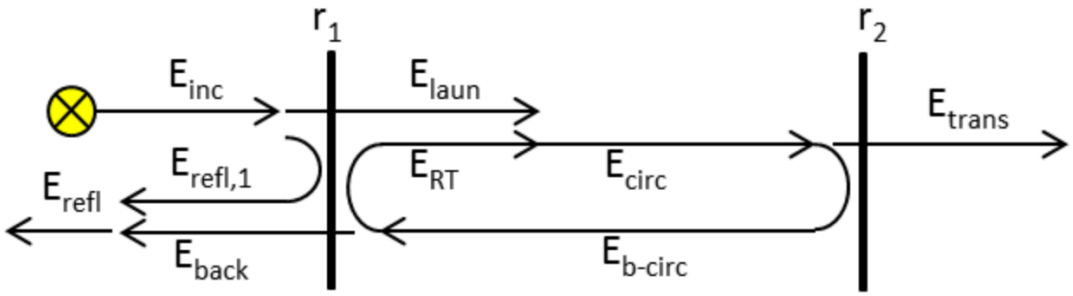

Figure 2.3: *Electric fields in a Fabry–Pérot resonator* [59]. *The electric-field mirror reflectivities are* r_1 *and* r_2. *Indicated are the characteristic electric fields produced by an electric field* E_{inc} *incident upon mirror 1:* $E_{\text{refl},1}$ *initially reflected at mirror 1,* E_{laun} *launched through mirror 1,* E_{circ} *and* $E_{\text{b-circ}}$ *circulating inside the resonator in forward and backward propagation direction, respectively,* E_{RT} *propagating inside the resonator after one round trip,* E_{trans} *transmitted through mirror 2,* E_{back} *transmitted through mirror 1, and the total field* E_{refl} *propagating backward. Interference occurs at the left- and right-hand sides of mirror 1 between* $E_{\text{refl},1}$ *and* E_{back}, *resulting in* E_{refl}, *and between* E_{laun} *and* E_{RT}, *resulting in* E_{circ}, *respectively.*

The power stored inside the cavity follows from the circulating field intensity:

$$P_{\text{circ}} = |E_{\text{circ}}|^2 = P_0 \frac{t_1^2}{1 + r_1^2 r_2^2 - 2 r_1 r_2 \cos(2kL)}. \tag{2.33}$$

The resonance condition corresponds to constructive interference after each round trip, occurring when:

$$2kL = 2\pi m, \quad m \in \mathbb{Z}. \tag{2.34}$$

As shown in Equation 2.33, the circulating power exhibits resonant enhancement when the denominator becomes small. This occurs precisely at the resonance condition given by Equation 2.34, where the cosine term equals unity. The characteristic behavior of the cavity response is illustrated in Figure 2.4, which shows the magnitude of the complex enhancement factor $|1/(1 - r_1 r_2 e^{2ikL})|$ as a function of the phase accumulation $2kL$.

The periodic peaks in Figure 2.4 correspond to successive longitudinal modes of the cavity, separated in frequency by the free spectral range (FSR):

$$\Delta\nu = \frac{c}{2L}. \tag{2.35}$$

The cavity finesse, which represents the average number of round trips a photon makes

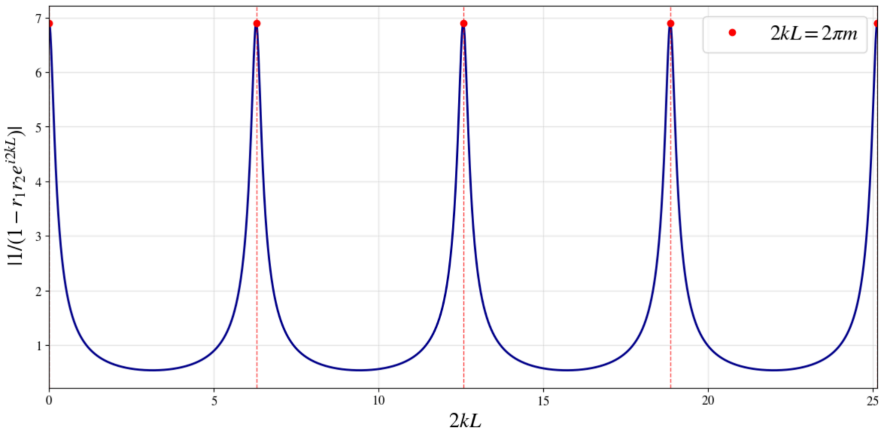

Figure 2.4: *Resonant behavior of a Fabry-Perot cavity showing the magnitude of the enhancement factor* $|1/(1 - r_1 r_2 e^{2ikL})|$ *as a function of phase accumulation* $2kL$*. The red dashed lines and markers indicate the resonance conditions where* $2kL = 2\pi m$ *for integer* m*, corresponding to constructive interference after each round trip. The sharp peaks demonstrate the frequency selectivity of the optical cavity.*

before escaping, is given by:

$$\mathcal{F} = \frac{\pi\sqrt{r_1 r_2}}{1 - r_1 r_2}. \tag{2.36}$$

At resonance, the circulating field reaches its maximum amplitude while the reflected power is minimized, making this the optimal operating point for GW detection. The spectral characteristics of the cavity are quantified by the FSR and finesse, with higher reflectivities leading to narrower linewidths and greater peak enhancement.

The linewidth, or full width at half maximum of the resonance peaks, relates to the finesse through:

$$\delta\nu = \frac{\Delta\nu}{\mathcal{F}}. \tag{2.37}$$

For high-reflectivity mirrors typical in GW detectors, the storage time of photons within the cavity becomes:

$$\tau = \frac{1}{\pi\delta\nu} = \mathcal{F} \cdot \frac{2L}{c\pi}, \tag{2.38}$$

which can be experimentally measured by observing the exponential decay of transmitted power when the input laser is suddenly blocked.

The crucial enhancement for GW detection comes from the phase shift induced by a GW of amplitude $h(t) = h_0 \cos(\omega_G t)$ on the cavity length $\Delta L(t) = (L h_0/2)\cos(\omega_G t)$. This produces an effective phase modulation of the intracavity field:

$$\Delta\phi_x \simeq \frac{4\mathcal{F}}{\pi} k_L \Delta L_x = \frac{2\mathcal{F}}{\pi} k_L L h_0 \cos(\omega_G t), \tag{2.39}$$

demonstrating that the Fabry–Perot resonance enhances the GW-induced phase shift by a factor $2\mathcal{F}/\pi$ relative to a simple Michelson interferometer.

For typical parameters in advanced detectors, with $\mathcal{F} \approx 450$ and $L = 4\,\mathrm{km}$ as in LIGO, the effective optical path length reaches approximately $1000\,\mathrm{km}$. This resonant enhancement makes the detection of GWs feasible with terrestrial-scale instruments, trans-

forming kilometer-scale arms into effectively hundred-kilometer-scale interferometers capable of measuring strains below $10^{-23}\,\mathrm{Hz}^{-1/2}$.

2.3 Advanced Gravitational Wave Detection with Dual-Recycled Interferometers

2.3.1 Signal Extraction Principles in Fabry-Pérot Interferometers

As shown in the previous section, the detection of GWs relies on measuring minute phase shifts, $\Delta\phi_{\mathrm{GW}}(t)$, induced in laser light circulating within interferometer arms. However, direct phase measurement presents significant challenges since photodetectors respond only to optical power, making it impossible to distinguish between GW-induced signals and laser amplitude noise.
This limitation is addressed through null instrument operation, where the interferometer is maintained at a dark fringe condition (red dot in **??**outputfig:IFO_output) such that output power vanishes in the absence of GW signals. While this configuration eliminates the DC background, it introduces another challenge: at the exact dark fringe, the power-phase derivative $\partial P/\partial\phi$ becomes zero. Consequently, for GW-induced phase shifts $\Delta\phi_{\mathrm{GW}}(t) \propto h$ (see Equation 2.24), the resulting power variation scales as $\Delta P \sim h$. Given typical GW strains of $h \sim 10^{-21}$, this would require detecting power variations of order 10^{-42}, which is experimentally infeasible.

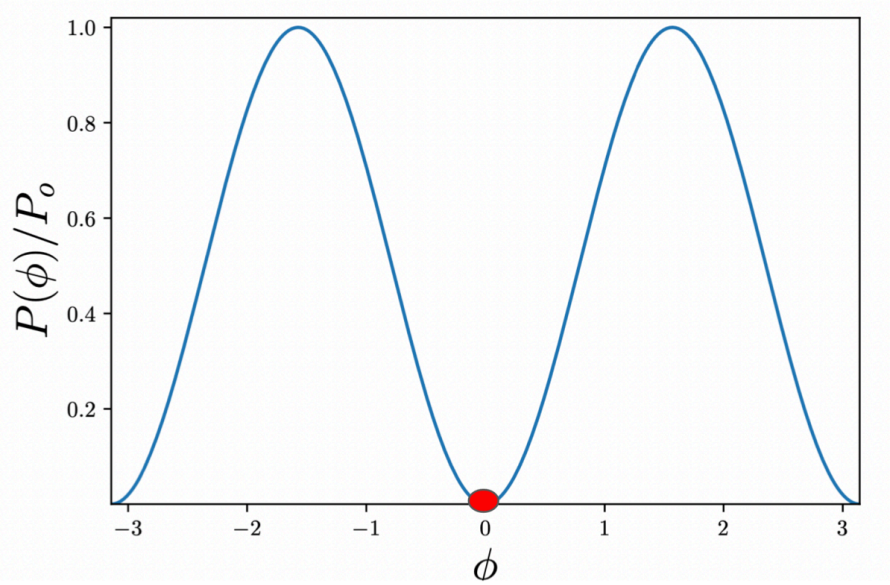

Figure 2.5: *Interferometer output characteristics showing normalized power versus phase shift. The dark fringe operating point (red) ensures minimal output power in the absence of GWs, optimizing SNR for weak detections* [60].

The standard solution employs heterodyne readout through phase modulation. Input laser light is modulated at frequency ω_{mod} using electro-optic modulators, dielectric crystals whose refractive index varies with applied electric fields $\vec{E}_{\mathrm{applied}}$ =

$\vec{E}_0 \cos(\omega_{\text{mod}} t)$ [61]. The modulated electric field becomes:

$$E_{\text{in}}(t) = E_0 e^{-i[\omega_L t + \Gamma \sin(\omega_{\text{mod}} t)]} \tag{2.40}$$

where ω_L is the laser frequency and $\Gamma \ll 1$ the modulation depth. For small Γ, this expands to:

$$E_{\text{in}}(t) = E_0 \left[J_0(\Gamma) e^{-i\omega_L t} + J_1(\Gamma) e^{-i(\omega_L + \omega_{\text{mod}})t} - J_1(\Gamma) e^{-i(\omega_L - \omega_{\text{mod}})t} + O(e^{-i\omega_L \pm 2\omega_{\text{mod}} t}) \right] \tag{2.41}$$

generating carrier (ω_L) and sideband $(\omega_L \pm \omega_{\text{mod}})$ components. These spectral components interact differently with Fabry-Pérot cavities, with reflected fields given by:

$$B(t) = E_0 \left[J_0(\Gamma) R_c e^{-i\omega_L t} + i\frac{\Gamma}{2} J_1(\Gamma) R_+ e^{-i(\omega_L + \omega_{\text{mod}})t} + i\frac{\Gamma}{2} J_1(\Gamma) R_- e^{-i(\omega_L - \omega_{\text{mod}})t} \right] \tag{2.42}$$

where R_c, R_+, and R_- represent cavity reflectances for carrier and sidebands respectively. When the interferometer is tuned such that the carrier satisfies the dark fringe condition $(a - b = n\lambda_L)$, GW passage perturbs the arm lengths, disrupting the perfect nulling. The resulting photodetector signal contains a component linear in h oscillating at ω_{mod}, which is extracted via demodulation.

2.3.2 Enhanced Sensitivity Through Optical Recycling and Squeezed Light

Modern GW detectors incorporate several optical enhancements to achieve the sensitivity required for astrophysical observations. Figure 2.6 illustrates a comprehensive dual-recycled interferometer configuration featuring multiple subsystems:

- **Power Recycling Mirror (PRM)**: Positioned before the beam splitter, this mirror system reflects light returning toward the laser back into the interferometer arms, significantly increasing circulating power by reusing photons that would otherwise be lost.
- **Signal Recycling Mirror (SRM)**: Located at the output port, this mirror assembly enables tuning of the interferometer's frequency response, allowing optimization of sensitivity across specific frequency bands of astrophysical interest.
- **Input Mode Cleaner (IMC)**: Following laser injection, the IMC filters higher-order spatial modes, reduces beam jitter, and suppresses frequency fluctuations before light enters the main interferometer, ensuring optimal beam quality.
- **Output Mode Cleaner (OMC)**: Positioned before detection, the OMC filters higher-order modes from the signal while reflecting control sidebands. A Faraday isolator prevents backscattered light from re-entering the interferometer.

Squeezed Light and Filter Cavity: Quantum noise imposes a fundamental sensitivity limit in GW detectors, manifesting as shot noise at high frequencies and radiation

pressure noise at low frequencies (see Section 2.4.1). The standard quantum limit represents the optimal trade-off between these competing quantum effects. The fundamental principle behind squeezed light enhanced interferometry involves injecting squeezed states of light into the detector's dark port to improve sensitivity beyond the quantum noise limit. Although no bright laser light enters through this port, the quantum fluctuations of the vacuum field do enter the system and become superimposed with the electromagnetic output field containing the GW signal. By replacing these vacuum fluctuations with continuous injection of squeezed vacuum states, the measurement uncertainty can be strategically manipulated [62, 63].

The quantum noise of light can be understood through two complementary properties: amplitude fluctuations and phase fluctuations. According to quantum mechanics, these two types of noise are fundamentally linked—reducing one necessarily increases the other. The lowest possible noise level, where both amplitude and phase fluctuations are equally small, corresponds to ordinary vacuum noise. Squeezed states break this symmetry by making one type of fluctuation exceptionally quiet while accepting more noise in the other.

The most common method for generating these squeezed states involves using nonlinear optical crystals that can convert laser light into quantum-correlated photon pairs through a process called parametric down-conversion. When placed inside an optical cavity, this system can continuously generate the squeezed light needed for GW detection. This method has become standard in current-generation detectors.

However, a fundamental challenge exists: reducing high-frequency shot noise makes low-frequency radiation pressure noise worse, and vice versa. The solution is frequency-dependent squeezing, which uses an additional optical component called a filter cavity. This cavity acts like a frequency-dependent rotator that changes the squeezing properties across different frequencies. At high frequencies (above about 100 Hz), it reduces shot noise, while at low frequencies (below 100 Hz), it automatically switches to reducing radiation pressure noise instead.

The filter cavity works by imposing a frequency-dependent delay on the squeezed light, with the amount of rotation determined by the cavity's specific design parameters. This solution enables detectors to surpass the standard quantum limit across a broad frequency band used for GW observations, significantly improving their ability to detect faint cosmic signals.

The combination of heterodyne readout techniques with advanced optical subsystems, power and signal recycling, mode cleaning, and quantum squeezing, enables the sensitivity required for GW astronomy. This integrated approach forms the foundation of current-generation detectors like LIGO and Virgo, allowing them to detect spacetime strains as small as 10^{-23} across a broad frequency range.

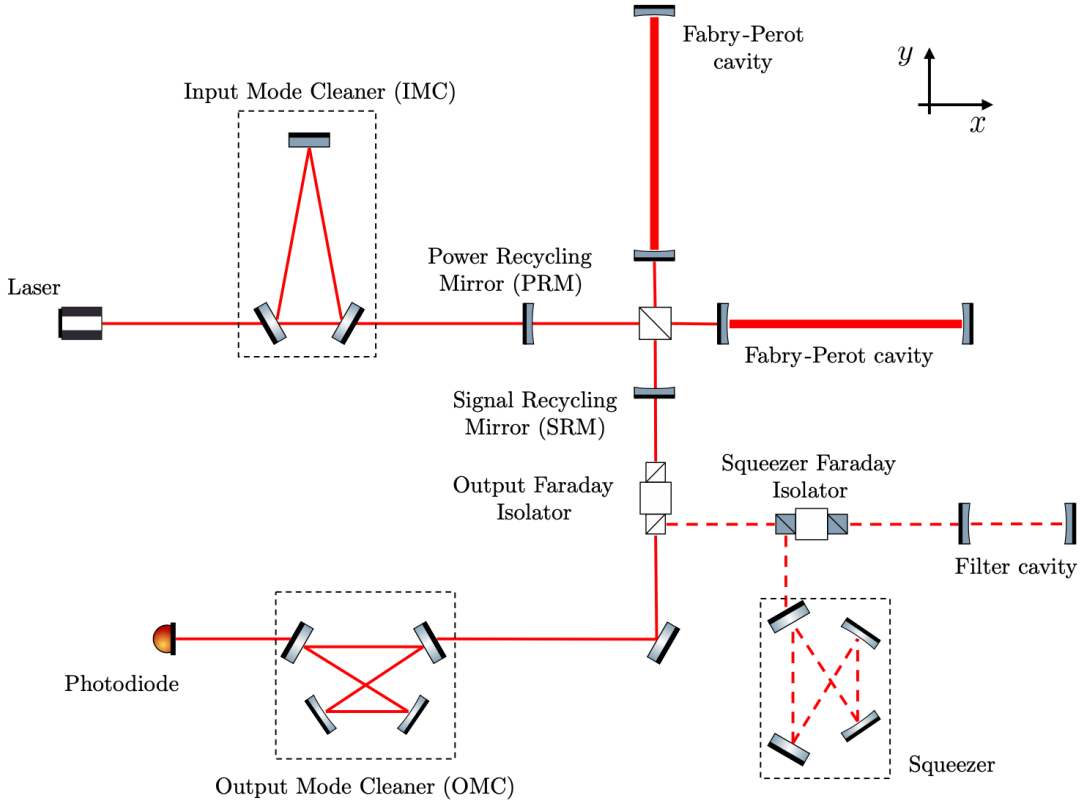

Figure 2.6: *Comprehensive schematic of a dual-recycled Michelson interferometer with Fabry-Perot arm cavities, incorporating input/output mode cleaners and squeezed light technology for enhanced GW detection.*

2.4 Sources of Noise in GW Detectors

Ground-based interferometric detectors are subject to multiple noise sources that fundamentally limit their scientific capabilities. Each noise component typically dominates within specific frequency bands, necessitating targeted design optimizations and operational strategies to effectively mitigate their impact on detector sensitivity.

The detector output can be modeled as:

$$s(t) = h(t) + n(t), \tag{2.43}$$

where $h(t)$ represents any GW signal present and $n(t)$ encompasses all noise contributions. While detector noise may exhibit non-stationary and non-Gaussian characteristics over long timescales, it can typically be treated as stationary during short observation intervals. Under this assumption, we define the expectation operator $\langle\cdot\rangle$ as averaging over time periods where signals remain approximately constant. The noise satisfies $\langle n(t)\rangle = 0$, and stationarity implies that the correlation function $\langle n(t)n(t')\rangle$ depends only on the time difference $t - t'$. Fourier transformation yields:

$$\langle \tilde{n}(f)\tilde{n}^*(f')\rangle = \iint dt\, dt' \, \langle n(t)n(t')\rangle e^{-i2\pi ft} e^{i2\pi f't'} \equiv \frac{1}{2}\delta(f - f')S_n(f), \tag{2.44}$$

where $S_n(f)$ represents the one-sided noise power spectral density. This quantity serves as the standard measure of interferometer sensitivity, directly determining signal detectability against the noise background. The following subsections analyze the principal noise sources affecting detector performance.

2.4.1 Shot Noise

Shot noise constitutes a fundamental limitation arising from the quantum nature of photons. For a laser beam with average photon arrival rate corresponding to N_γ photons detected during time T, the measured optical power is:

$$P = \frac{1}{T} N_\gamma \hbar \omega_L. \tag{2.45}$$

Photon detection represents a discrete counting process where individual photon arrivals constitute independent events. This process follows Poisson statistics, with probability distribution:

$$p(N; \bar{N}) = \frac{1}{N!} \bar{N}^N e^{-\bar{N}}, \tag{2.46}$$

where N denotes the detected photon count and $\bar{N}$ its expectation value. For large $\bar{N}$, this distribution approaches Gaussian statistics with standard deviation $\sqrt{\bar{N}}$, yielding photon number fluctuations:

$$\Delta N_\gamma = \sqrt{N_\gamma}. \tag{2.47}$$

These fluctuations manifest as optical power noise:

$$(\Delta P)_{\text{shot}} = \frac{1}{T}\Delta N_\gamma \hbar\omega_L = \sqrt{\frac{\hbar\omega_L P}{T}}. \tag{2.48}$$

Conversely, the GW signal induces power variations:

$$(\Delta P)_{\text{GW}} = P_{\text{circ}}|\sin(2\phi_0)|\frac{\phi_{\text{FP}}}{2}. \tag{2.49}$$

Equation 2.39 provided a simplified expression for the phase shift. A more complete treatment accounts for the sensitivity degradation that occurs when the GW frequency is comparable to the photon storage time within the cavity:

$$|\phi_{\text{FP}}| \approx h_0 \frac{4\mathcal{F}k_L L}{\pi}\frac{1}{\sqrt{1+(f/f_p)^2}}, \tag{2.50}$$

with the pole frequency approximated by [61]:

$$f_p = \frac{c}{4\mathcal{F}L}. \tag{2.51}$$

The SNR (SNR), quantifying signal distinguishability from noise, becomes:

$$\rho = \frac{(\Delta P)_{\text{GW}}}{(\Delta P)_{\text{shot}}} = \sqrt{\frac{P_{\text{circ}}T}{2\hbar\omega_L}}\frac{8\mathcal{F}Lh_0}{\lambda}\frac{1}{\sqrt{1+(f/f_p)^2}}. \tag{2.52}$$

For a periodic signal with amplitude h_0 observed for duration T, the SNR relates to the noise spectral density as [61]:

$$\rho = h_0\sqrt{\frac{T}{S_n(f)}}. \tag{2.53}$$

Higher circulating power generally reduces shot noise, thereby improving sensitivity. Notably, this noise originates from fundamental quantum principles and cannot be overcome without employing quantum techniques such as light squeezing, discussed in Section 2.3.2.

2.4.2 Radiation Pressure Noise

Radiation pressure noise represents another quantum mechanical limitation in GW detectors. This phenomenon arises from the momentum transfer when photons reflect from mirror surfaces, creating fluctuating forces due to statistical variations in photon arrival. A laser beam with circulating power P_{circ} exerts an average force $F = 2P_{\text{circ}}/c$ on mirrors, with fluctuations given by:

$$\Delta F = \frac{2\sqrt{\hbar\omega_L P_{\text{circ}}}}{c\sqrt{T}}. \tag{2.54}$$

The corresponding spectral density of this fluctuating force becomes:

$$S_F^{1/2} = \frac{2\sqrt{\hbar\omega_L P_{\text{circ}}}}{c}. \tag{2.55}$$

Applying Newton's second law $F = m\ddot{x}$ (assuming no external forces or damping), the Fourier-space relationship $F(f) = -m(2\pi f)^2 x(f)$ yields the displacement spectral density:

$$S_x^{1/2} = \frac{2\sqrt{\hbar\omega_L P_{\text{circ}}}}{m(2\pi f)^2 c}. \tag{2.56}$$

Photons incident on the beam splitter distribute randomly between the two arms with anti-correlated statistics. Under operating conditions, radiation pressure contributions from both arms add incoherently, introducing a factor of 2, while correlated fluctuations cancel.

Converting to equivalent strain noise using the transfer factor L for Michelson interferometers gives:

$$S_n^{1/2}(f)_{\text{rad}} = \frac{4\sqrt{2\hbar\omega_L P_{\text{circ}}}}{mL(2\pi f)^2 c^2}. \tag{2.57}$$

Incorporating Fabry-Pérot cavity effects, where mirror vibrations at frequency f detune the cavity and reduce circulating power by $[1 + (f/f_p)^2]$, modifies the expression to:

$$S_n^{1/2}(f)_{\text{rad}} = \frac{8\sqrt{2}\mathcal{F}}{mL(2\pi f)^2}\sqrt{\frac{\hbar P_{\text{circ}}}{c\lambda\mathcal{F}}}\frac{1}{1 + (f/f_p)^2}. \tag{2.58}$$

Like shot noise, radiation pressure noise stems from fundamental quantum properties of light and represents an inescapable limitation without quantum enhancement techniques such as squeezed light with filter cavities.

2.4.3 Standard Quantum Limit

The combined quantum noises establish a fundamental sensitivity boundary independent of technological advancement. This quantum noise manifests Heisenberg's uncertainty principle in action: photon position measurements inevitably impart recoil momentum to the mirrors. The total quantum noise spectral density combines both contributions:

$$S_n^{1/2}(f)_{\text{qua}} = \sqrt{S_n^{1/2}(f)_{\text{shot}}^2 + S_n^{1/2}(f)_{\text{rad}}^2} = \frac{1}{L\pi f_0}\sqrt{\frac{\hbar}{m}}\left(1 + \frac{f_p^2}{f^2}\right)^{1/4}\left(\frac{f_0^4}{f^4} + \frac{f_p^2}{f^2} + 1\right)^{1/2}, \tag{2.59}$$

where:

$$f_0 = \frac{4\mathcal{F}}{\pi}\sqrt{\frac{P_{\text{circ}}}{2\mathcal{F}\lambda c m}}. \tag{2.60}$$

Minimizing quantum noise at specific frequencies yields the standard quantum limit

(SQL):

$$S_n^{1/2}(f)_{\mathrm{SQL}} = \frac{1}{2\pi f L}\sqrt{\frac{8\hbar}{m}}. \tag{2.61}$$

This represents the optimal spectral density achievable at each frequency when circulating power is optimized. The envelope of these minima defines the ultimate quantum noise limit:

$$S_n^{1/2}(f)_{\mathrm{opt}} = \frac{1}{2}S_{\mathrm{SQL}}(f)\left[\sqrt{K(f)} + \frac{1}{\sqrt{K(f)}}\right], \tag{2.62}$$

with:

$$K(f) = \frac{4\pi\omega_L P_{\mathrm{circ}}}{\mathcal{F} m L^2 \omega^2(\omega_p^2 + \omega^2)}. \tag{2.63}$$

2.4.4 Displacement Noise

Displacement noise encompasses all non-GW, non-radiation pressure effects that alter test mass positions. Since strain is defined as $h = \Delta L/L$, any length variation appears as an equivalent GW signal.

Seismic Noise

Ground motion, particularly below 10 Hz, constitutes a significant noise source from natural phenomena (ocean waves, earthquakes, wind) and human activities (traffic, machinery). Seismic displacement typically follows a power-law spectrum:

$$x(f) = A\left(\frac{1\ \mathrm{Hz}}{f}\right)^{\gamma}\ \mathrm{m\ Hz^{-1/2}}, \tag{2.64}$$

with $\gamma \approx 2$ above 1 Hz. The amplitude A depends on local seismic quietness. Since typical levels preclude GW detection, sophisticated suspension systems are essential. A simple pendulum with resonant frequency f_0 attenuates strain noise by f_0^2/f^2 for $f \gg f_0$, while N-stage pendulums provide $(f_0^2/f^2)^N$ suppression. Typical systems place resonances around 10 Hz to enable detection above this threshold.

Newtonian Noise

Gravity-gradient noise arises from fluctuating Newtonian gravitational forces due to mass density variations in the surrounding environment. Microseismic activity particularly affects mass density distributions, altering the gravitational field interacting with test masses. The gravitational potential fluctuation from density variations is:

$$\delta\phi(t, \vec{x}_0) = -G\int dV\ \frac{\delta\rho(t, \vec{x})}{|\vec{x}_0 - \vec{x}|}. \tag{2.65}$$

Primary density fluctuation sources include [64]:

$$\delta\rho_{\text{seis}}(t,\vec{x}) = -\nabla\cdot(\rho_{\text{soil}}(\vec{x})\vec{\xi}(t,\vec{x})), \tag{2.66}$$

$$\delta\rho_{\text{press}}(t,\vec{x}) = \frac{\bar{\rho}_{\text{atm}}}{\gamma p_{\text{atm}}}\delta p_{\text{atm}}(t,\vec{x}), \tag{2.67}$$

$$\delta\rho_{\text{temp}}(t,\vec{x}) = -\frac{\bar{\rho}_{\text{atm}}}{\bar{T}_{\text{atm}}}\delta T_{\text{atm}}(t,\vec{x}), \tag{2.68}$$

where ρ_{soil} is soil density, $\vec{\xi}(t,\vec{x})$ represents seismic displacement, p_{atm} and T_{atm} denote air pressure and temperature, and $\gamma \approx 1.4$ is the adiabatic index. Barred quantities indicate averages. These combined contributions can limit low-frequency sensitivity below 10 Hz.

Newtonian noise presents a near-fundamental limitation resistant to conventional attenuation. Mitigation strategies include underground detector construction in quieter environments or real-time noise monitoring and subtraction.

2.4.5 Thermal Noise

At mid-to-low frequencies, thermal motion of mirror atoms and suspension components creates unpredictable displacements. Brownian molecular fluctuations generate mechanical dissipation modeled via the fluctuation-dissipation theorem:

$$S_x(\omega) = \frac{4k_BT\Re[Y(\omega)]}{\omega^2}, \tag{2.69}$$

where $Y(\omega)$ is mechanical admittance, k_B Boltzmann's constant, and T temperature.

For a damped harmonic oscillator $m\ddot{x} + \beta\dot{x} + kx = F$, the admittance becomes:

$$Y(\omega) = \frac{-im\omega^3 + \beta\omega^2 + ik\omega}{(k - m\omega^2)^2 + \beta^2\omega^2}, \tag{2.70}$$

yielding displacement spectral density:

$$S_x(\omega) = \frac{4k_BT\beta}{(k - m\omega^2)^2 + \beta^2\omega^2}. \tag{2.71}$$

Viscous damping sources include eddy currents from mirror magnets and residual gas damping. Structural losses within materials introduce complex elasticity $k(1 + i\phi)$, where ϕ is the loss angle:

$$S_x(\omega) = \frac{1}{\omega^2}\frac{4k_BTk\phi}{(k - m\omega^2)^2 + k^2\phi^2}. \tag{2.72}$$

For suspended mirrors forming pendulums, the elastic constant combines gravitational

and wire contributions:

$$k = k_g \left(1 + i\frac{k_e}{k_g}\phi_w\right) \equiv k_g(1 + i\phi_p), \tag{2.73}$$

where ϕ_p is the pendulum loss angle ($\sim 10^{-6}$ for Virgo suspensions). Above pendulum resonance, thermal noise approximates:

$$S_x(\omega) = \frac{4k_B T\phi_p}{\omega_0^2 m\omega^4}\omega, \tag{2.74}$$

with ω_0 the pendulum resonance frequency.

Thermo-optical Noise

Laser illumination causes mirror substrate heating and compression, with heat transfer to cooler regions reducing restoring forces. Thermoelastic noise approximates [65]:

$$S_x(\omega) = \frac{8k_B T\alpha^2(1+\sigma)^2\kappa T}{\omega^2\pi^{3/2}C\rho r_0^3}, \tag{2.75}$$

where α is thermal expansion coefficient, σ Poisson's ratio, κ thermal conductivity, C specific heat per unit volume, ρ material density, and r_0 laser beam radius.
Thermorefractive noise from laser-induced refractive index changes is [66]:

$$S_x(\omega) = \frac{4k_B T}{\omega^2}\frac{4\kappa T l}{\pi(\rho C)^2 r_0^4}\left(\frac{dn}{dT}\right)^2, \tag{2.76}$$

where l is optics length and dn/dT the thermo-refractive coefficient.

Coating Thermal Noise

Despite minimal mass fraction, coating thermal noise often dominates due to higher dissipation concentrated at the reflection surface. The approximation [65]:

$$S_x(f) = \frac{4k_B T}{\pi^3 f}\frac{1-\sigma^2}{E r_0}\phi\left[1 + O\left(\frac{r_0}{R}\right)\right], \tag{2.77}$$

where E is Young's modulus, ϕ the dissipation loss angle, and $I = 1.873$ for Gaussian beams. As a dominant noise around hundreds of Hz, mitigation strategies include cryogenic operation, reduced coating mechanical losses, and increased beam spot size for power dilution.

2.4.6 Residual Gas Noise

Ultra-high vacuum (UHV) operation minimizes gas-related noise from molecular collisions with mirrors and laser phase shifts from density variations along the beam path. Residual gas also enhances scattered light and optical absorption.

Despite UHV conditions ($\sim 10^{-9}$ mbar), remaining molecules contribute noise:

$$S_{\text{gas}}(f) = \frac{(4\pi\alpha)^2}{v_0} \int_0^L \frac{\rho(z)}{w(z)} e^{-2\pi f w(z)/v_0} dz, \tag{2.78}$$

where α is optical polarizability, v_0 average molecular speed, ρ number density, and $w(z)$ beam radius. Common species include H_2, H_2O, N_2, CO, and CO_2. Hydrocarbon-free environments prevent condensable organic deposition on optics.

2.4.7 Scattered Light Noise

Scattered light noise affects low-to-mid frequencies and requires careful mitigation. Photons deviating from intended paths due to surface imperfections or residual gas can reflect from unintended surfaces and recombine with the main beam, mimicking GW signals.

Current detectors implement robust scattering suppression in main Fabry-Pérot cavities, though strong microseismic activity or less-shielded optical systems can still experience sensitivity limitations. Detailed treatment follows in subsequent chapters.

2.4.8 Overall Sensitivity Curve

The combined effect of all noise sources determines the overall sensitivity profile of GW detectors. Figure 2.7 illustrates the projected sensitivity for Advanced LIGO based on theoretical noise models and design parameters, showing individual noise contributions and their combined effect on the detection threshold.

The actual performance during observing runs demonstrates the evolution of detector capabilities. Figure 2.8 compares the measured strain sensitivity between the O3b and O4a observing periods for both LIGO Hanford (LHO) and LIGO Livingston (LLO) observatories, highlighting the substantial improvements achieved through technical upgrades.

The significant sensitivity improvement observed in O4a stems from several key enhancements. Quantum noise reduction was achieved through the implementation of frequency-dependent squeezing, while scattered light mitigation involved the removal of septum windows that previously transmitted ground vibrations. Additional improvements included damping of baffle resonances and replacement of alignment dither systems with camera-based servos at LHO, which eliminated spectral features around 20 Hz. The persistent difference in sensitivity between the two observatories, particularly noticeable around 100 Hz at LLO, reflects site-specific conditions and component variations.

While design sensitivity curves represent theoretical projections, actual detector performance during observation periods incorporates various technical noise sources that emerge during operation. These include:

- **Laser frequency noise**: Residual phase noise from laser frequency instabilities

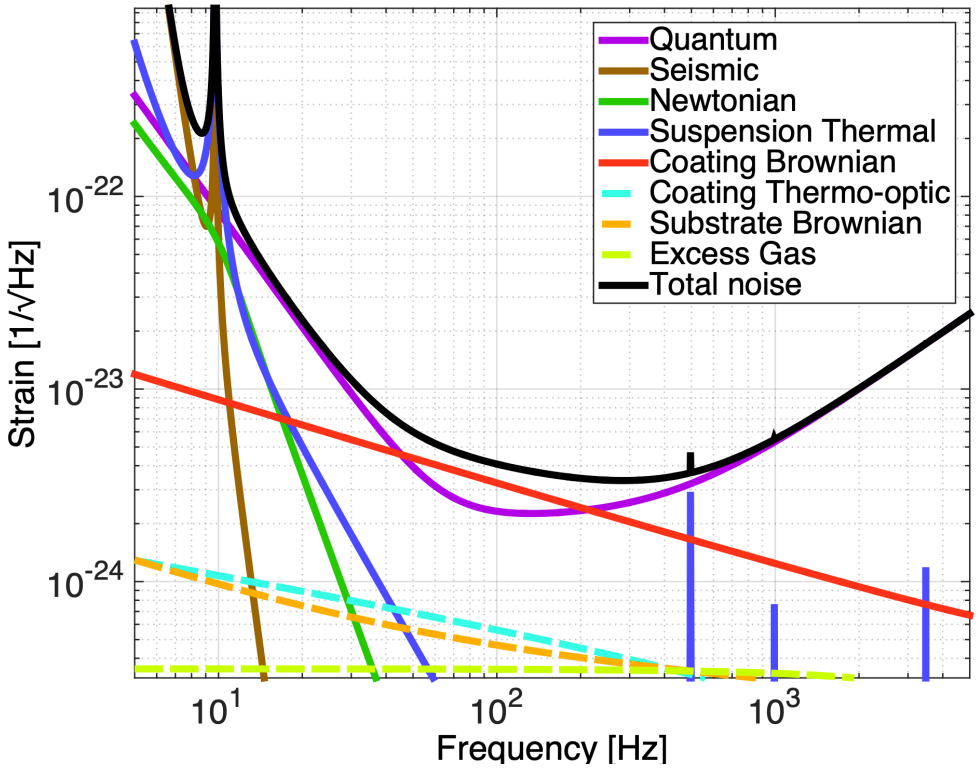

Figure 2.7: *Theoretical sensitivity curve for Advanced LIGO displaying individual noise contributions and the total design sensitivity, based on fundamental physical limits and instrument parameters* [67].

that leaks to detection ports through optical asymmetries despite active stabilization systems.

- **Laser intensity noise**: Power fluctuations at dark ports that remain significant at spectral extremes despite control system mitigation.
- **Alignment sensing noise**: Limitations in mirror alignment detection systems that constrain positioning accuracy and dominate low-frequency noise budgets.
- **Beam pointing noise**: Fluctuations in beam alignment affecting optical mode matching, manifesting as spectral peaks from mechanical resonances.

The continuous refinement of detector sensitivity through systematic noise identification and mitigation has been crucial for expanding the astrophysical reach of GW astronomy. The progression from O3b to O4a sensitivity demonstrates how technical innovations and operational optimizations translate directly into improved scientific capabilities, enabling the detection of fainter GW signals from more distant cosmic sources.

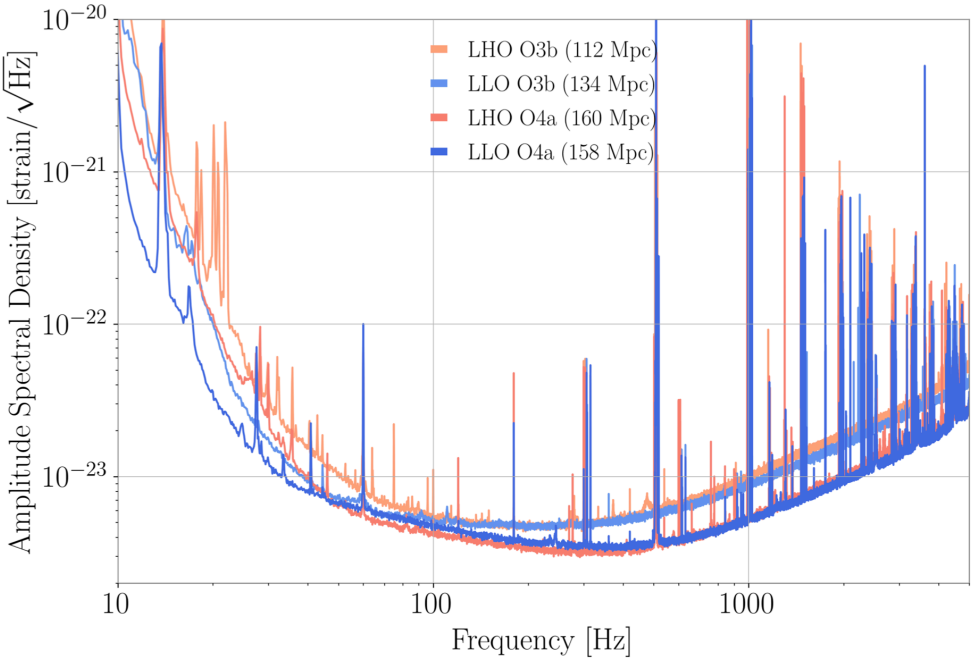

Figure 2.8: *Evolution of detector sensitivity between O3b and O4a observing runs for LIGO Hanford and LIGO Livingston. The enhanced broadband performance in O4a results from multiple technical improvements including quantum squeezing implementation, scattered light mitigation, and advanced control systems.*

3
Analysis of GW Data

3.1 Searches and the Identification of GW Transients in the Data

The detection and characterization of GW represent one of the most challenging signal processing problems in modern physics. As shown in previous sections, typical astrophysical signals produce strain amplitudes of order 10^{-21} to 10^{-23} in ground-based detectors, buried deep within instrumental noise that can be orders of magnitude larger. This chapter describes the sophisticated statistical and computational methods developed to extract these faint cosmic signals and infer the properties of their astrophysical sources.

The analysis of GW data proceeds through two complementary stages: *detection*, which identifies potential signals in the noisy detector output, and *parameter estimation*, which extracts physical information from confirmed detections. Detection pipelines employ matched filtering techniques that leverage our precise theoretical knowledge of expected waveform morphologies, while parameter estimation uses Bayesian inference to quantify uncertainties in source properties and test fundamental physics.

The development of these analysis methods has evolved in parallel with detector technology. Early searches focused on identifying individual events through computationally efficient techniques, while modern analyses must handle the high event rates of advanced detectors and provide rapid alerts for multimessenger follow-up. This chapter covers the theoretical foundations of both detection and parameter estimation, the practical implementation of these methods in current observatories, and the milestones achieved through successive observing runs.

3.1.1 Matched Filtering

The detection problem for GWs from compact binary coalescences involves discriminating astrophysical signals against a dominant background of instrumental noise in laser interferometers. Typical strain amplitudes of order 10^{-21} to 10^{-23} are buried deep

within instrumental noise that can be orders of magnitude larger. However, the deterministic nature of GWforms predicted by GR enables their detection despite this signal-to-noise deficit. Although merger times are stochastic, the functional form of the waveform is known with high precision. Since the GW emission from compact binary coalescences is fully specified by a limited parameter set, including component masses, spins, and orbital orientation, the resulting strain templates can be computed with high precision. This enables the implementation of optimal filtering techniques, where the data are cross-correlated with theoretical waveforms to identify signals matching the expected morphology.

Matched filtering has long been known to be the optimal linear technique for detecting a known signal embedded in stationary, Gaussian noise [68, 69].

The detection methodology proceeds by comparing the detector output $s(t)$ to a theoretical template through a noise-weighted inner product, defined for frequency-domain quantities as:

$$(a \mid b) \equiv 4\,\mathrm{Re} \int_0^\infty \frac{\tilde{a}(f)\,\tilde{b}^*(f)}{S_n(f)}\,df, \tag{3.1}$$

where $S_n(f)$ represents the detector's one-sided noise PSD. The matched-filter signal-to-noise ratio (SNR) for a template h is given by:

$$\rho_{mf}(s \mid h) = \frac{(s \mid h)}{\sqrt{(h \mid h)}}. \tag{3.2}$$

where s denotes the detector output strain data as defined in Eq. **??**. When the data contain the true signal $h(t;\vec{\lambda}_{\mathrm{true}})$, filtering with a perfectly matching template $h_{\mathrm{template}}(t;\vec{\lambda})$ yields an expected SNR of:

$$\langle\rho\rangle = \frac{(h \mid h_{\mathrm{template}})}{\sqrt{(h_{\mathrm{template}} \mid h_{\mathrm{template}})}}, \tag{3.3}$$

which achieves its theoretical maximum exclusively when the template identically matches the signal:

$$\rho_{\mathrm{optimal}} = \sqrt{(h \mid h)} = 2\sqrt{\int_0^\infty \frac{|\tilde{h}(f)|^2}{S_n(f)}\,df}. \tag{3.4}$$

This expression shows that the detectability in each frequency band depends not only on the intrinsic waveform amplitude $|\tilde{h}(f)|$ but also on the noise PSD $S_n(f)$.

The practical implementation of matched filtering is demonstrated in Figure 3.1, which shows the SNR time series obtained by applying Eq. (3.2) to GW150914 data from the LIGO Hanford detector. The analysis used a BBH template with component masses of $36M_\odot$, revealing a clear SNR peak of $\rho \approx 19$ at the merger time. This exceeds the background fluctuations by a significant margin, illustrating how matched filtering can extract weak GW signals from noisy detector data. The temporal structure of the SNR evolution follows the expected signal morphology, with increasing values during

inspiral, a sharp peak at merger, and rapid decay during ringdown.

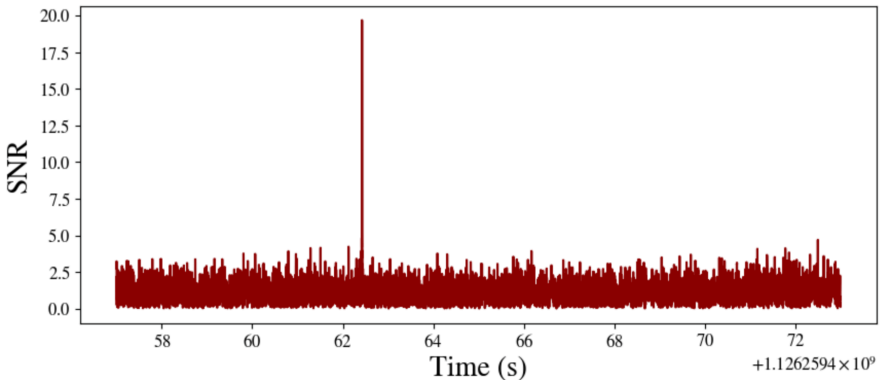

Figure 3.1: *SNR time series from matched filtering analysis of GW150914 data.*

3.1.2 Template Banks and Parameter Space Coverage

In practical search scenarios, the true source parameters $\vec{\lambda}_{\text{true}}$ are a priori unknown. Consequently, rather than employing a single template, the data are systematically filtered against a comprehensive template bank $\{h(\vec{\lambda}_i)\}$ that provides discrete coverage of the continuous parameter space manifold. Although the waveform manifold exhibits continuity in component masses and spins, computational constraints mandate restriction to discrete sampling points. These templates must be strategically placed such that any astrophysical signal within the targeted parameter space generates a sufficient SNR when correlated with its nearest template neighbor.

The match quantifies the optimal achievable overlap between a signal and a template, obtained by maximizing their normalized inner product over extrinsic parameters (time and phase offsets):

$$\mathcal{M}(\vec{\lambda}, \Delta\vec{\lambda}) \equiv \max_{\Delta\lambda_{\text{extr}}} (\hat{h}(\vec{\lambda}) \mid \hat{h}(\vec{\lambda} + \Delta\vec{\lambda})), \tag{3.5}$$

This maximization is restricted to extrinsic parameters because waveforms related by time and phase shifts represent identical physical templates. The match ranges from 0 (orthogonal waveforms) to 1 (identical waveforms after optimal alignment).

For templates that are close in parameter space, the match can be approximated by a Taylor expansion:

$$\mathcal{M}(\vec{\lambda}, \Delta\vec{\lambda}) \simeq 1 - g_{ij}\Delta\lambda^i\Delta\lambda^j, \tag{3.6}$$

where the template-space metric is defined as

$$g_{ij} \equiv -\frac{1}{2}\frac{\partial^2 \mathcal{M}}{\partial\Delta\lambda^i\partial\Delta\lambda^j}\bigg|_{\Delta\lambda=0}. \tag{3.7}$$

This metric endows the waveform manifold with a geometric structure, allowing distances between neighboring templates to be expressed as

$$ds^2 = 1 - \mathcal{M} = g_{ij}\Delta\lambda^i\Delta\lambda^j. \tag{3.8}$$

This geometric interpretation forms the basis of template bank construction methods, which aim to place templates such that no point in parameter space lies farther than a chosen distance, or mismatch, from the nearest template.
The mismatch is defined as

$$\mathcal{MM}(\vec{\lambda}, \Delta\vec{\lambda}) = 1 - \mathcal{M}(\vec{\lambda}, \Delta\vec{\lambda}), \tag{3.9}$$

and directly measures the fractional loss in SNR due to imperfect matching between the true signal and the template. Template placement algorithms are typically designed to ensure $\mathcal{MM} \lesssim 3\%$ everywhere in the search space, guaranteeing minimal loss in detection efficiency and preserving the effectiveness of signal vetoes.
The fitting factor serves as the standard metric for quantifying template bank quality, representing the proximity of true signals to the template manifold in terms of the fraction of SNR recovered when filtering data with an approximate family of templates. For a given signal h_*, the fitting factor is formally defined as:

$$\mathcal{FF}(h_*) = \max_{\vec{\lambda} \in \text{bank}} \mathcal{M}(\tilde{h}_*, \tilde{h}(\vec{\lambda})). \tag{3.10}$$

The fractional reduction in recovered SNR is quantified by $1-\mathcal{FF}(h_*)$. When $\mathcal{FF}(h_*) < 1$, this indicates that the signal lies outside the optimally covered parameter space region, with the fitting factor representing the maximum achievable cross-correlation with available templates.

3.1.3 Multi-Detector Network Analysis

While template bank construction addresses the coverage of the intrinsic parameter space, real searches must also account for the distributed nature of the detector network. The full power of GW searches emerges in the network configuration of detectors. By coherently combining data from multiple observatories, the network SNR is constructed as

$$\rho^2_{\text{network}} = \sum_{i=1}^{N_{\text{det}}} \rho_i^2, \tag{3.11}$$

where ρ_i is the SNR in detector i. Coherent network analysis enables valuable consistency checks via residual analysis and χ^2-tests, while the construction of null streams that cancel genuine signals but preserve instrumental artifacts offers powerful discrimination against detector glitches. Furthermore, source localization is achieved through time-of-arrival differences between detectors, where the time delay between detectors i and j constrains the source direction through:

$$\Delta t_{ij} = \frac{\vec{d}_{ij} \cdot \hat{n}}{c}, \tag{3.12}$$

where $\vec{d}_{ij}$ is the baseline vector between detectors and $\hat{n}$ is the unit vector pointing toward the source, enabling rapid sky localization crucial for multimessenger follow-up observations.

3.1.4 Significance

However, a high network SNR is not in itself sufficient to claim astrophysical origin, as instrumental noise transients can masquerade as coherent signals. Assessing the significance of candidate events requires robust background estimation to account for the non-Gaussian and non-stationary nature of detector noise. The most widely used method is time-slide analysis, in which artificial relative time shifts are applied between detectors. This destroys genuine astrophysical correlations while preserving the statistical properties of the noise, allowing one to estimate the rate of accidental coincidences. The false alarm rate (FAR) is then defined as

$$\mathrm{FAR} = \frac{N_{\mathrm{background}}}{T_{\mathrm{background}}},$$

where $N_{\mathrm{background}}$ is the number of background triggers exceeding a given significance threshold in an effective background time $T_{\mathrm{background}}$. The inverse false alarm rate (IFAR),

$$\mathrm{IFAR} = \frac{1}{\mathrm{FAR}},$$

represents the expected time between false alarms of comparable significance and provides a direct measure of the confidence in a candidate event. In current searches, detection thresholds are typically set to require $\mathrm{IFAR} \gtrsim 1\,\mathrm{yr}$.

Finally, the development of low-latency analysis has been critical for multimessenger astronomy. Online pipelines now deliver GW candidate alerts within minutes, enabling rapid follow-up by telescopes across the electromagnetic spectrum. These low-latency analyses balance the need for speed with robustness, performing preliminary parameter estimation within hours and producing refined results with full Bayesian inference over the following days or weeks. Achieving this capability has required innovations in streaming data processing at kilohertz rates, efficient searches over template banks with up to 10^6 waveforms, and the automation of data quality monitoring. Together, these efforts make it possible not only to detect GWs in real time, but also to trigger the global network of observatories that together form the multimessenger infrastructure of modern astrophysics.

3.2 Parameter Estimation

3.2.1 Bayesian Framework

The determination of astrophysical source properties from GW observation, including component masses, spins, and orbital parameters, constitutes an inverse problem wherein one infers causal parameters from the data. This class of inference problem is optimally addressed through Bayesian statistical methodology, which provides a rigorous mathematical foundation for parameter estimation.
Bayesian analysis provides a systematic way to combine prior expectations with the information contained in the data while rigorously quantifying uncertainties throughout the analysis. In contrast to frequentist approaches that define probability through hypothetical repeated sampling, the Bayesian interpretation treats probability as a quantitative measure of rational belief conditioned on available information. This epistemological foundation renders Bayesian methods particularly appropriate for GW astronomy, where astrophysical events are intrinsically non-reproducible, and where the inference must accommodate sophisticated waveform models and realistic detector noise characteristics.
The mathematical basis for this approach is established by Bayes' theorem, which prescribes the mechanism for updating prior knowledge into posterior understanding through conditional probability. Denoting the source parameters by $\boldsymbol{\theta}$ and the observed detector data by $\mathbf{d}$, the theorem specifies the posterior probability distribution as:

$$p(\boldsymbol{\theta}|\mathbf{d},\mathcal{H}) = \frac{p(\mathbf{d}|\boldsymbol{\theta},\mathcal{H})\,p(\boldsymbol{\theta}|\mathcal{H})}{p(\mathbf{d}|\mathcal{H})}, \tag{3.13}$$

Each constituent term in Bayes' theorem admits a distinct epistemological and mathematical interpretation:

- The **posterior probability distribution** $p(\boldsymbol{\theta}|\mathbf{d},\mathcal{H})$ encapsulates our refined understanding of the source parameters following assimilation of the experimental data, representing the complete solution to the inverse problem by encoding all available information about $\boldsymbol{\theta}$ after observational constraints have been applied.
- The **likelihood function** $p(\mathbf{d}|\boldsymbol{\theta},\mathcal{H})$ quantifies the probability of obtaining the specific observational dataset $\mathbf{d}$ under the assumption of particular parameter values $\boldsymbol{\theta}$, thereby measuring how well the theoretical model explains the observed data for any given parameter configuration.
- The **prior probability distribution** $p(\boldsymbol{\theta}|\mathcal{H})$ embodies our pre-existing knowledge or physical assumptions regarding plausible parameter values before incorporation of the current data, incorporating constraints from astrophysical population studies, theoretical considerations, or previous experimental results.
- The **Bayesian evidence** $p(\mathbf{d}|\mathcal{H})$ serves as an essential normalization constant ensuring proper probabilistic calibration of the posterior distribution, while simultaneously providing a quantitative measure of the model's overall explanatory

power through marginalization over the entire parameter space.

The evidence term, obtained through marginalization over the entire parameter space, guarantees that the posterior probability distribution maintains unit integral:

$$p(\mathbf{d}|\mathcal{H}) = \int p(\mathbf{d}|\boldsymbol{\theta}, \mathcal{H})\, p(\boldsymbol{\theta}|\mathcal{H})\, d\boldsymbol{\theta}. \tag{3.14}$$

Beyond its role as a normalization factor, this quantity assumes critical importance in the context of model selection, as it facilitates rigorous comparison between competing theoretical hypotheses through the computation of Bayes factors, thereby providing a principled mechanism for evaluating the relative explanatory power of alternative models.
In practical implementations of parameter estimation, the primary objective centers upon characterization of the posterior probability distribution. Given that the evidence remains invariant for a fixed model and dataset, the posterior distribution exhibits proportionality to the product of the likelihood function and the prior distribution:

$$p(\boldsymbol{\theta}|\mathbf{d}, \mathcal{H}) \propto p(\mathbf{d}|\boldsymbol{\theta}, \mathcal{H})\, p(\boldsymbol{\theta}|\mathcal{H}). \tag{3.15}$$

This fundamental proportionality relationship establishes the theoretical foundation for sampling algorithms, such as Markov Chain Monte Carlo methods and nested sampling techniques, that systematically explore the complex topology of the posterior distribution to extract parameter constraints and credible intervals.

3.2.2 Application to Tests of General Relativity

The Bayesian framework finds one of its most powerful applications in the rigorous testing of fundamental physical theories. Within the context of GW astronomy, this allows us to ask a precise question: are the observed data more consistent with signals described by Einstein's GR, or do they provide evidence for a beyond-GR model?
This is naturally formulated as a problem of **Bayesian model selection** between two competing hypotheses:

- The **GR hypothesis** (H_{GR}) postulates that the data contain a signal perfectly described by a waveform model derived from General Relativity.
- The **modified GR hypothesis** (H_{modGR}) postulates that the signal is described by a parameterized extension of the GR waveform, allowing for possible deviations.

The model comparison hinges on the computation of the **Bayes factor**, which is the ratio of the evidences for the two models:

$$B^{\mathrm{GR}}_{\mathrm{modGR}} = \frac{p(\mathbf{d}|H_{\mathrm{modGR}})}{p(\mathbf{d}|H_{\mathrm{GR}})}. \tag{3.16}$$

A Bayes factor $B^{\mathrm{GR}}_{\mathrm{modGR}} > 1$ indicates support for the modified GR hypothesis given the data.

To construct a generic H_{modGR} hypothesis, the parameter space of the GR model is extended by introducing **test parameters** $\{\delta\chi_i\}$. These parameters quantitatively measure deviations in the gravitational waveform, for instance, by allowing the coefficients of the post-Newtonian phase expansion to vary independently of the binary's intrinsic parameters like its mass and spin.

A sophisticated approach involves formulating H_{modGR} not as a single model with a fixed number of extra parameters, but as a composite of several sub-hypotheses, H_I. Each sub-hypothesis H_I corresponds to a different subset I of the test parameters being active (non-zero). This strategy automatically embodies **Occam's razor**: it prevents the model from being penalized for unnecessary degrees of freedom, ensuring that evidence for a deviation is only claimed if the data genuinely require it.

The methodology detailed in Chapter 4 is a concrete implementation of this Bayesian model selection framework, designed to perform a generic and robust test of GR using GW signals from compact binary coalescences.

3.3 Sampling Algorithms

Exploring the posterior distribution is a computationally demanding task, as the parameter space is typically high-dimensional, with fifteen or more parameters required to describe a generic binary merger. Modern analyses employ a variety of advanced sampling algorithms to efficiently explore these complex posteriors. The Metropolis-Hastings algorithm constitutes the foundational methodology for Markov Chain Monte Carlo sampling approaches. The algorithm initiates from an arbitrary starting point θ_0 within the parameter space. At each iteration n, a candidate parameter vector θ^* is generated from a proposal distribution $q(\theta^*|\theta_n)$, which governs the transition mechanism between states. The acceptance probability for this proposed move is computed as:

$$\alpha = \min\left(1, \frac{p(\theta^*|\vec{d})q(\theta_n|\theta^*)}{p(\theta_n|\vec{d})q(\theta^*|\theta_n)}\right) \tag{3.17}$$

If the proposal is accepted according to this probabilistic criterion, the chain advances to the new state with $\theta_{n+1} = \theta^*$; otherwise, the chain remains at its current position with $\theta_{n+1} = \theta_n$. Crucially, the evidence normalization constant present in the posterior distribution cancels in the acceptance ratio, thereby requiring only the evaluation of the likelihood-prior product rather than the fully normalized posterior density.

3.3.1 Nested Sampling

Nested sampling is a computational technique that simultaneously performs parameter estimation and calculates the Bayesian evidence. Unlike traditional Markov Chain Monte Carlo methods that sample the posterior directly, nested sampling transforms the multidimensional evidence integral into a one-dimensional problem.

Algorithm Principle

The fundamental idea involves reformulating the evidence integral by introducing a new variable. Define the prior mass $X(\lambda)$ as the fraction of prior volume where the likelihood exceeds threshold λ:

$$X(\lambda) = \int_{\{L(\boldsymbol{\theta})>\lambda\}} p(\boldsymbol{\theta}|\mathcal{H})\, d\boldsymbol{\theta}, \tag{3.18}$$

where $L(\boldsymbol{\theta}) \equiv p(\mathbf{d}|\boldsymbol{\theta}, \mathcal{H})$ denotes the likelihood. This quantity decreases monotonically from $X = 1$ (when λ is minimal) to $X = 0$ (when λ exceeds all likelihood values).
The evidence can then be expressed as a one-dimensional integral:

$$\mathcal{Z} = p(\mathbf{d}|\mathcal{H}) = \int_0^1 L(X)\, dX, \tag{3.19}$$

where $L(X)$ represents the inverse function giving the likelihood level corresponding to prior mass X.
The nested sampling algorithm executes through a carefully structured iterative procedure that systematically explores the parameter space while simultaneously computing the Bayesian evidence:

1. **Initialization**: The algorithm commences by drawing an ensemble of N sample points, termed "live points," from the prior probability distribution $p(\boldsymbol{\theta}|\mathcal{H})$. This initial population provides a representative sampling of the entire prior volume and establishes the starting configuration for the subsequent iterative exploration.
2. **Iteration**: At each algorithmic step indexed by i, the following sequence of operations is performed:
    - Identification of the live point $\boldsymbol{\theta}_i$ possessing the lowest likelihood value $L_i \equiv p(\mathbf{d}|\boldsymbol{\theta}_i, \mathcal{H})$ within the current ensemble, thereby determining the lowest likelihood threshold for the subsequent sampling step.
    - Archival recording of this point $\boldsymbol{\theta}_i$ along with its associated likelihood value L_i, preserving this information for subsequent evidence computation and posterior distribution reconstruction.
    - Replacement of the discarded point with a new sample drawn from the prior distribution, subject to the stringent constraint that its likelihood must exceed the established threshold L_i, ensuring progressive exploration of higher likelihood regions.
    - Incorporation of the discarded point into the accumulating evidence estimate, with each such point contributing a weighted term to the final evidence calculation.
3. **Prior mass evolution**: Each iteration induces a systematic contraction of the accessible prior volume. For an ensemble of N live points, the expected reduction

in prior mass at step i follows the statistical relationship:

$$X_i = e^{-i/N} X_{i-1}, \tag{3.20}$$

commencing from the initial condition $X_0 = 1$, which yields the asymptotic expression $X_i \approx e^{-i/N}$ for the diminishing prior volume.

4. **Evidence calculation**: The Bayesian evidence $\mathcal{Z}$ is numerically approximated through the weighted summation:

$$\mathcal{Z} \approx \sum_{i=1}^{M} L_i \, w_i, \tag{3.21}$$

where the weighting factors $w_i = X_{i-1} - X_{i+1}$ represent the differential prior mass intervals associated with each discarded point, and M denotes the total number of iterations performed throughout the algorithm's execution.

5. **Termination**: The algorithm proceeds iteratively until the residual prior volume contributes negligibly to the cumulative evidence estimate, typically determined when the product of the maximum likelihood among remaining live points and the surviving prior mass falls below a predetermined fractional tolerance threshold.

Posterior Samples

Beyond computing evidence, nested sampling naturally generates posterior samples. Each discarded point $\boldsymbol{\theta}_i$ receives posterior weight proportional to $L_i w_i$. After normalization, these weights provide a representation of the posterior distribution suitable for parameter estimation.
The method offers several advantages: efficient handling of multimodal posteriors, simultaneous parameter estimates and evidence calculation, and focused computational effort on high-likelihood regions while maintaining thorough exploration.

3.3.2 Likelihood Function

The likelihood quantifies how well a model with parameters θ explains the data d. Given the data model of Eq. **??**, where the detector output consists of a signal plus noise, constructing the likelihood requires understanding both expected signals and the stochastic nature of detector noise.

Noise Characterization

The noise process is typically modeled as Gaussian and stationary, meaning it is fully described by its mean (assumed zero) and its covariance. For discrete time samples t_i and t_j, the covariance matrix is defined as

$$C_{ij} = \langle n(t_i) n(t_j) \rangle, \tag{3.22}$$

where $\langle\cdot\rangle$ denotes an average over noise realizations. The covariance matrix encodes the expected correlations between noise at different times: each element C_{ij} gives the expected product of noise values at times t_i and t_j. Stationarity implies that C_{ij} depends only on the time difference $|t_i - t_j|$, not the absolute times.
In the frequency domain, stationarity implies that different frequency components of the noise are uncorrelated. The noise is then characterized by its one-sided PSD $S_n(f)$, which describes how the noise power is distributed across frequencies. The PSD is related to the covariance matrix via Fourier transformation.

Likelihood Construction

Assuming Gaussian stationary noise, the residual $r(t) = d(t) - h(t;\boldsymbol{\theta})$ between data and model follows a multivariate Gaussian distribution. The likelihood becomes:

$$p(\mathbf{d}|\boldsymbol{\theta},\mathcal{H}) = \frac{1}{(2\pi)^{N/2}[\det \mathbf{C}]^{1/2}} \exp\left[-\frac{1}{2}\sum_{i,j} r_i\, C^{-1}_{ij}\, r_j\right], \tag{3.23}$$

where N is the number of data samples, $\mathbf{C}$ is the noise covariance matrix, and C^{-1}_{ij} denotes its inverse.
The exponential argument represents a weighted least-squares measure of model fit. The covariance matrix inverse weights different time samples according to expected noise levels, samples with lower noise contribute more strongly to parameter constraints.
Taking the logarithm gives the time-domain log-likelihood:

$$\ln p(\mathbf{d}|\boldsymbol{\theta},\mathcal{H}) = -\frac{1}{2}\sum_{i,j} r_i C^{-1}_{ij} r_j - \frac{1}{2}\ln\det \mathbf{C} - \frac{N}{2}\ln(2\pi). \tag{3.24}$$

Frequency Domain Formulation

Practical implementations typically work in the frequency domain due to computational efficiency. Transforming to frequency components $\tilde{d}(f)$, $\tilde{h}(f;\boldsymbol{\theta})$, and $\tilde{n}(f)$ via Fourier transform, the likelihood simplifies when noise is stationary.
The noise covariance matrix becomes diagonal in the frequency domain, different frequency bins are uncorrelated. The likelihood takes the form:

$$p(\mathbf{d}|\boldsymbol{\theta},\mathcal{H}) \propto \exp\left[-\frac{1}{2}\sum_k \frac{|\tilde{d}(f_k) - \tilde{h}(f_k;\boldsymbol{\theta})|^2}{S_n(f_k)}\Delta f\right], \tag{3.25}$$

where the sum runs over frequency bins f_k, and Δf is the frequency resolution.
Using the previously defined noise-weighted inner product (Eq. 3.1), the log-likelihood can be written compactly as

$$\ln p(\mathbf{d}|\boldsymbol{\theta},\mathcal{H}) = \text{const} - \frac{1}{2}\langle d - h | d - h\rangle. \tag{3.26}$$

This formulation makes explicit how detector sensitivity (through $S_n(f)$) weights different frequency components when constraining parameters. Frequencies with better sensitivity (lower S_n) contribute more information.
The constant term contains normalization factors independent of θ and can be ignored during parameter estimation. This formulation highlights that the contribution of each frequency component to the likelihood is naturally weighted by the detector sensitivity: frequencies with lower $S_n(f)$ contribute more strongly.

3.4 Prior Distributions

The specification of prior probability distributions constitutes a fundamental component of Bayesian parameter estimation. Priors encode our pre-existing knowledge of source properties and observational constraints, while ideally remaining as uninformative as possible in regimes where such knowledge is limited. Careful selection of priors ensures that the resulting posterior distributions faithfully reflect both the data and well-motivated physical assumptions, avoiding undue bias while maintaining sensitivity to the information content of the observations.

3.4.1 Intrinsic Parameters Priors

Mass Priors

The choice of mass priors reflects the underlying physical understanding of the binary components and the aspects of the signal to which detectors are most sensitive. Commonly, priors are chosen to be uniform either in the individual component masses (m_1, m_2) or in derived combinations such as the chirp mass $\mathcal{M}_c$ and the mass ratio $q = m_2/m_1$ (with $m_1 \geq m_2$ by convention). For studies that aim to characterize astrophysical populations, priors may be chosen either in the detector frame or in the source frame, depending on whether cosmological redshift effects are to be incorporated.

Spin Priors

The specification of spin priors depends both on astrophysical considerations and on the desire for minimally informative assumptions where knowledge is uncertain. The dimensionless spin magnitude of each component, $\chi_i = cS_i/(Gm_i^2)$, is bounded between zero and unity by the Kerr limit. In practice, several standard choices are employed. Spins may be treated isotropically, with uniform magnitude and random orientation on the sphere, or they may be restricted to align or anti-align with the orbital angular momentum. Astrophysically motivated constraints may also be imposed; for example, BHs formed through stellar collapse are expected to satisfy $\chi \lesssim 0.9$.
Two effective spin combinations are particularly relevant for GW analyses. The effective inspiral spin,

$$\chi_{\text{eff}} = \frac{m_1\chi_1 \cos\theta_1 + m_2\chi_2 \cos\theta_2}{m_1 + m_2}, \tag{3.27}$$

where θ_i is the angle between each spin and the orbital angular momentum, captures the leading-order influence of spin on the inspiral rate. The effective precession spin χ_p encodes contributions from spin components in the orbital plane and is the primary driver of precession-induced modulations in the waveform.

3.4.2 Extrinsic Parameter Priors

Extrinsic parameters describe not the intrinsic properties of the binary system, but rather how it is positioned and oriented relative to the observer and the detector network. Fully specifying these parameters requires accounting for the relation between three reference frames:

- The **source frame**, where the binary's orbital angular momentum defines the z-axis.
- The **Earth frame**, where the source location is expressed in right ascension and declination.
- The **wave frame**, aligned with the direction of GW propagation and defining the polarization basis.

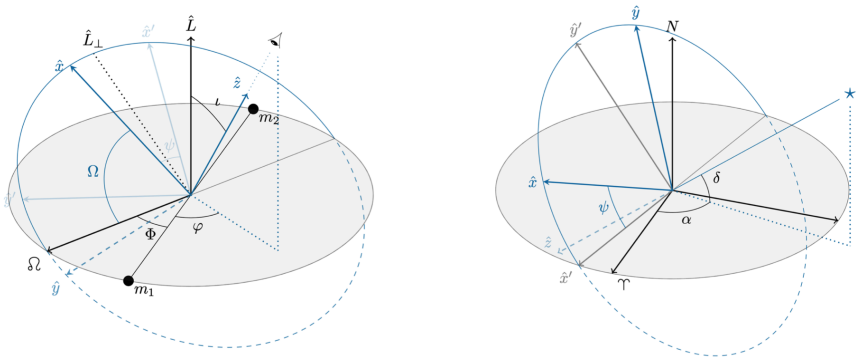

Figure 3.2: *Coordinate systems for GW parameterization. Left: Binary system in the source frame showing inclination ι and azimuthal angle φ. Right: Celestial coordinates in the Earth frame with right ascension α and declination δ. The wave frame (not shown) connects these systems through the polarization angle ψ, following standard GW data analysis conventions.*

The geometric relation between the source and Earth frame is illustrated in Fig. 3.2. The angles (ι, ϕ) describe the position of the observer in the source frame, while (α, δ) locate the source in the Earth frame. The final rotation between the source and wave frames defines the polarization angle ψ, following the conventions adopted by the LVK Collaboration.

Sky Location

The sky position of the source in the Earth frame is given by right ascension α and declination δ. A non-informative prior corresponds to assuming sources are uniformly

distributed over the celestial sphere, which leads to

$$p(\alpha) \propto \text{const}, \quad p(\delta) \propto \cos\delta. \tag{3.28}$$

Luminosity Distance

The luminosity distance D_L is typically assigned a prior that is uniform in comoving volume, consistent with a homogeneous distribution of sources on cosmological scales. For a flat universe, this implies

$$p(D_L) \propto D_L^2, \tag{3.29}$$

up to a maximum distance determined by detector sensitivity or astrophysical considerations.

Binary Orientation

In the source frame, the observer's direction is parameterized by the inclination angle ι, defined as the angle between the orbital angular momentum and the line of sight, and the azimuthal angle ϕ. Symmetry dictates that the observer's direction relative to the source should be isotropically distributed, yielding

$$p(\cos\iota) \propto \text{const}, \quad p(\phi) \propto \text{const}. \tag{3.30}$$

Only ι typically enters the waveform amplitude explicitly, while ϕ may be partially degenerate with phase parameters depending on detector response.

Polarization and Coalescence Parameters

The rotation between the source and wave frames defines the polarization angle ψ, which is conventionally assigned a uniform prior

$$\psi \sim \mathcal{U}(0, \pi). \tag{3.31}$$

The coalescence phase ϕ_c and coalescence time t_c similarly receive uniform priors over their allowed ranges, ensuring no preferred arrival phase or time is assumed a priori.

3.4.3 Calibration Uncertainties

The reconstructed strain data used in parameter estimation is obtained by applying a modeled detector response function $R_{\text{model}}(f, t)$ to the raw detector output. However, the true response function $R(f, t)$ is not known with perfect precision, and discrepancies between the modeled and true response introduce systematic calibration errors that propagate into astrophysical parameter estimates.

These calibration uncertainties are conventionally parameterized by a complex correction factor:

$$\eta(f,t) = \frac{R(f,t)}{R_{\mathrm{model}}(f,t)} = \left[1 + \delta A(f,t)\right] e^{i\delta\phi(f,t)}, \tag{3.32}$$

where $\delta A(f,t)$ and $\delta\phi(f,t)$ describe frequency- and time-dependent amplitude and phase errors, respectively. During contemporary observing runs, typical uncertainties are of order $\delta A \sim 10\%$ in amplitude and $\delta\phi \sim 10^\circ$ in phase, though the precise values vary across the detector's sensitive frequency band.

The relationship between the observed strain and the true GW signal is consequently modified as:

$$h_{\mathrm{true}}(f,t) = \eta(f,t)\, h_{\mathrm{obs}}(f,t), \tag{3.33}$$

making $\eta(f,t)$ an additional nuisance parameter that must be accounted for in the likelihood evaluation.

Calibration uncertainties predominantly affect parameters that depend on the overall amplitude or phase evolution of the GW signal. Luminosity distance and binary inclination are particularly sensitive to amplitude errors δA, while phase-dependent quantities such as coalescence phase and sky localization can be biased by phase errors $\delta\phi$. Intrinsic parameters like chirp mass are generally more robust to calibration uncertainties but may still be affected through parameter correlations in the posterior distribution.

In practical inference frameworks, calibration errors are incorporated by assigning informed priors on $\eta(f,t)$ derived from laboratory measurements, instrumental characterization, or injected calibration lines. Depending on the computational approach, these priors may be marginalized analytically, yielding an effectively broadened likelihood, or sampled explicitly alongside astrophysical parameters, enabling complete propagation of calibration systematics into the final posterior distributions.

3.5 Waveform Models for GW Data Analysis

The accurate detection and parameter estimation of GW signals from compact binary coalescences relies critically on the availability of high-fidelity waveform models. These models must accurately capture the complex physics of binary dynamics across the entire inspiral-merger-ringdown sequence while remaining computationally efficient enough for practical data analysis applications. Following the first direct detection of GWs in 2015 [70], the development of waveform models has evolved into a sophisticated field balancing physical accuracy against computational constraints.

As advanced GW detectors continue to improve in sensitivity and the catalog of observed events grows [71], systematic biases from waveform modeling uncertainties are becoming increasingly important relative to statistical errors. Current analyses typically employ multiple waveform families to assess systematic uncertainties, with consistency between different models serving as an important validation of parameter

estimation results. However, as demonstrated in recent studies [72], combined analyses of multiple events can reveal subtle preferences for particular waveform families that may indicate underlying systematic biases.

This section describes the three principal waveform families used in contemporary GW data analysis: surrogate models built from numerical relativity simulations, effective-one-body waveforms derived from analytical gravity, and phenomenological models constructed through hybrid approaches.

The choice of waveform model in GW data analysis involves careful consideration of the signal properties, computational constraints, and required accuracy. For high-mass systems where the merger and ringdown contribute significantly to the detected signal, models with accurate merger descriptions (such as EOB or surrogate models) may be preferred. For longer signals where computational efficiency is paramount, phenomenological models often provide the most practical solution.

3.5.1 Surrogate Waveform Models

Surrogate waveform models represent a data-driven approach to waveform generation, constructed through interpolation over precomputed numerical relativity simulations. These models offer exceptional accuracy within their domain of validity, as they inherit the fidelity of full numerical solutions to Einstein's equations without introducing analytical approximations beyond the numerical discretization inherent in the original simulations.

The construction of surrogate models typically involves several key steps: (1) selection of a dense sampling of the binary parameter space (masses, spins, etc.), (2) generation of high-accuracy numerical relativity waveforms at each parameter space point, (3) identification of reduced-order basis representations to handle the high-dimensional data, and (4) development of accurate interpolation schemes across the parameter space.

The `NRSur7dq4` model [73] represents the state-of-the-art in surrogate modeling for precessing BBH systems. This time-domain model extends earlier surrogate constructions to higher mass ratios, covering systems with $q \leq 6$ and total masses $M \gtrsim 66M_{\odot}$, with precise validity boundaries depending on the mass ratio. The model includes all subdominant harmonic modes up to $l \leq 4$ in the co-precessing frame, providing comprehensive mode content for accurate waveform representation.

The principal advantage of surrogate models lies in their high accuracy, as they directly encode numerical relativity results. However, this comes at the cost of limited parameter space coverage due to the computational expense of generating sufficient numerical relativity simulations. Additionally, surrogate models can be computationally intensive to evaluate compared to purely analytical approaches, though they remain significantly faster than generating new numerical relativity waveforms from scratch.

3.5.2 Effective-One-Body Waveforms

Effective-one-body (EOB) waveforms provide an analytical approach to waveform modeling that bridges the gap between post-Newtonian theory and numerical relativity. As discussed in Section 1.2.3, the EOB framework maps the two-body problem onto an effective one-body problem, where a test particle moves in a deformed BH metric.
The `SEOBNRv4PHM` model [74] represents a state-of-the-art implementation of the EOB approach for precessing systems with higher-order modes. Built from the aligned-spin `SEOBNRv4HM` model [75], this time-domain waveform includes subdominant harmonics $(l, |m|) = (2, 1), (3, 3), (4, 4), (5, 5)$ in the co-precessing frame and is valid for mass ratios $1 \leq q \leq 50$.
The EOB approach offers several advantages: it provides a physically motivated description of the binary dynamics throughout the coalescence process, maintains consistency with analytical results in various limits (post-Newtonian, test-particle, etc.), and can be extended to new physical scenarios through systematic improvements to the underlying Hamiltonian and radiation reaction models. However, EOB waveforms are typically computationally expensive to generate compared to phenomenological models, making them challenging for large-scale parameter estimation studies.
For the `SEOBNRv4PHM` model specifically, the precessing sector is not directly calibrated to numerical relativity simulations, relying instead on the twisting-up procedure applied to the aligned-spin baseline. This represents a potential limitation in regions of parameter space where precession effects are strong and not fully captured by this approximate mapping.

3.5.3 Phenomenological Waveforms

Phenomenological waveform models take a hybrid approach, combining analytical insights from post-Newtonian theory and BH perturbation theory with numerical relativity calibrations. These models are constructed using piecewise closed-form expressions for different phases of the coalescence (inspiral, intermediate, and ringdown), making them computationally efficient while maintaining good accuracy.
The `IMRPhenomXPHM` model [76] represents a frequency-domain phenomenological approximant that includes both precession and higher-order modes. Built from the non-precessing `IMRPhenomXHM` model [77] through a twisting-up procedure [78, 79], this model includes subdominant modes $(l, |m|) = (2, 1), (3, 3), (3, 2), (4, 4)$ in the co-precessing frame. The model is formally valid for spin magnitudes up to 0.99 and mass ratios $q \leq 1000$, though its recommended usage is limited to $q \leq 20$ due to calibration against numerical relativity simulations.
A complementary time-domain approach is implemented in the `IMRPhenomTPHM` model [80], built from the non-precessing `IMRPhenomTHM` model [81] using a distinct twisting-up procedure optimized for time-domain construction. This model includes harmonics $(l, |m|) = (2, 1), (3, 3), (4, 4), (5, 5)$ and is valid for secondary masses $m_2 \geq 0.5 M_\odot$ and spin magnitudes $|\chi_{1,2}| \leq 0.99$ for $q \leq 200$, with recommended usage up to $q \leq 20$.

The primary advantage of phenomenological models is their computational efficiency, particularly for frequency-domain models like `IMRPhenomXPHM` that enable rapid evaluation of noise-weighted inner products during matched filtering. However, this efficiency comes at the cost of some physical intuition, as the piecewise construction may not maintain the same level of physical consistency as EOB approaches throughout the entire coalescence process.

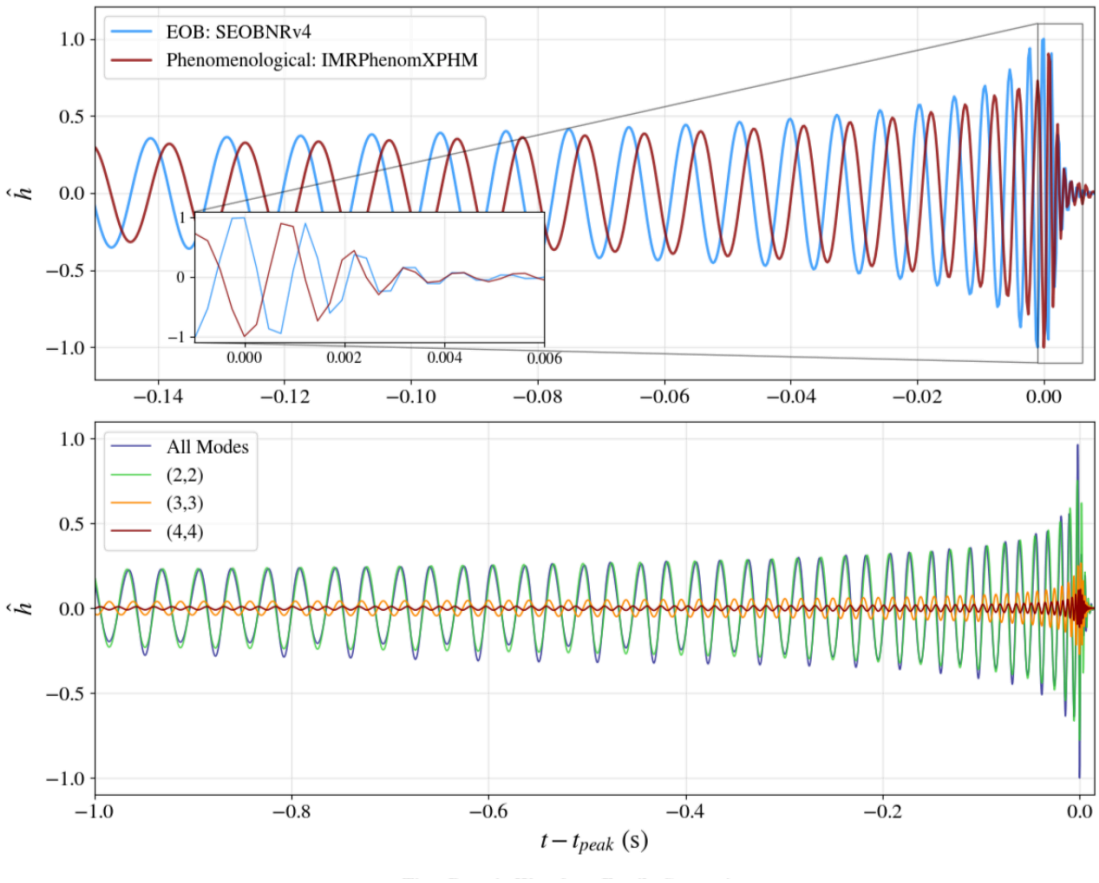

Figure 3.3: *Comparison of GWform models.* ***Top:*** *Time-domain waveforms from EOB (SEOBNRv4, blue) and phenomenological (IMRPhenomXPHM, dark blue) approaches for an equal-mass binary with spin $\chi = 0.9$. The inset shows a detailed view of the late inspiral and merger region, highlighting the subtle differences between the two models as they approach coalescence.* ***Bottom:*** *Higher-order mode decomposition of the phenomenological waveform IMRPhenomXPHM for a mass ratio $q \approx 5.7$ system, showing individual mode contributions normalized to the peak amplitude of the full waveform. The $(2, 2)$ mode dominates the signal, while higher harmonics $(3, 3)$ and $(4, 4)$ contribute significantly during the merger and ringdown phases.*

3.6 Milestones in GW Catalogs Through O4

The past decade has seen GW astronomy mature into an established observational field. Systematic improvements in detector sensitivity across observing runs have enabled detailed studies of compact binary populations, their astrophysical origins, and strong-field gravitational physics.

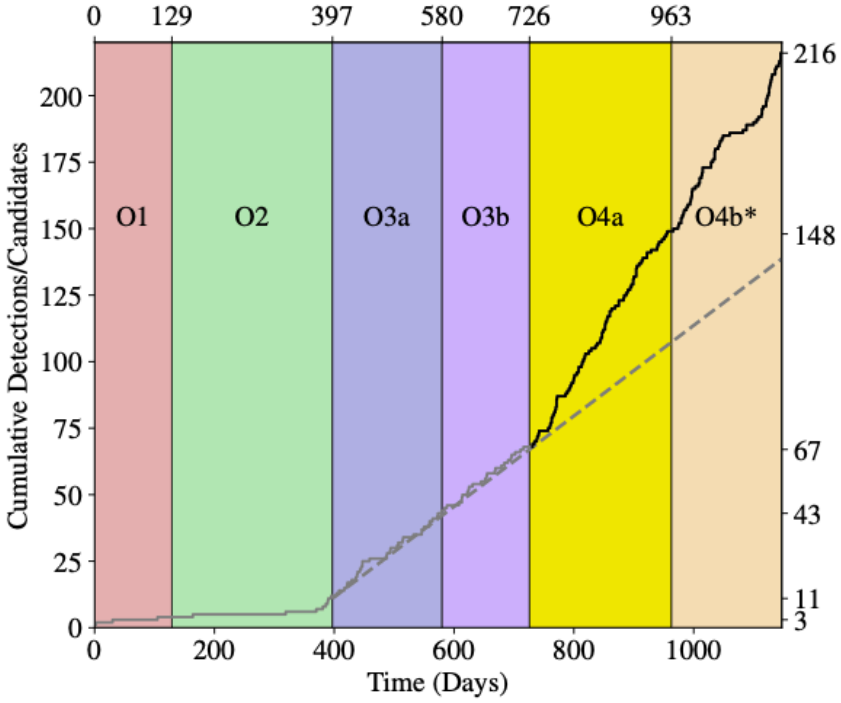

Figure 3.4: *Cumulative GW detections across observing runs from O1 through O4. The exponential growth in detection rates reflects steady improvements in detector sensitivity and the maturation of data analysis pipelines. The transition from isolated discoveries in O1 to near-daily detections in O4 marks GW astronomy's emergence as a routine observational tool for astrophysics* [82].

3.6.1 GWTC-1: The Dawn of GW Astronomy

The first observing run (O1, September 2015–January 2016) marked humanity's entry into the era of GW astronomy. On September 14, 2015, just days after Advanced LIGO began its first science run, the detectors captured GW150914—a BBH merger with component masses of $36M_\odot$ and $29M_\odot$ at a luminosity distance of approximately 410 Mpc. This landmark detection provided the first direct evidence for GW, confirmed the existence of stellar-mass BBHs, and demonstrated that BHs with masses exceeding $25M_\odot$ exist in nature. The signal was so clear that it could be seen by eye in the filtered detector data, with a combined signal-to-noise ratio exceeding 24.

O1 yielded two additional detections: GW151226, a lighter system with masses $\sim 14M_\odot$ and $\sim 8M_\odot$ that completed at least 55 orbital cycles in the LIGO band, and the marginal candidate LVT151012. These early detections immediately revealed that BBH mergers occur at rates sufficient to enable population studies and that stellar-mass BHs span a wider mass range than previously observed through X-ray binaries.

The second observing run (O2, November 2016–August 2017) expanded the catalog with eight additional BBH mergers, but its most transformative contribution came on August 17, 2017, with GW170817, the first detected BNS merger. With component masses of approximately $1.46M_\odot$ and $1.27M_\odot$, this event occurred at a mere 40 Mpc, making it the closest and most thoroughly studied GW source to date. The multi-messenger observation campaign that followed stands as a watershed moment in as-

tronomy: a short gamma-ray burst detected by Fermi and INTEGRAL 1.7 seconds after merger, followed by the discovery of an optical/infrared kilonova in NGC 4993, and subsequent observations across the entire electromagnetic spectrum from radio to X-rays over weeks and months.

GW170817 delivered an extraordinary scientific harvest. The GW signal, combined with the kilonova observations, provided direct evidence for the r-process nucleosynthesis of heavy elements in NS mergers, resolving a decades-old mystery about the cosmic origin of gold, platinum, and other heavy elements. The time delay between the GW arrival and the gamma-ray burst placed stringent constraints on violations of Lorentz invariance and the photon mass. Perhaps most remarkably, the combination of GW distance measurement and electromagnetic redshift determination enabled a completely independent measurement of the Hubble constant: $H_0 = 70^{+12}_{-8}$ km s^{-1} Mpc^{-1}, offering a new approach to resolving the tension between early- and late-universe measurements.

The Virgo detector joined the network in August 2017, enabling true three-detector observations for the first time. GW170814, observed by all three instruments, demonstrated the power of the global network for source localization, reducing the sky area uncertainty by more than an order of magnitude compared to two-detector observations. GWTC-1, released in 2019, reported 11 confident detections from O1 and O2: 10 BBH mergers and 1 BNS merger, establishing GW astronomy as a permanent fixture in the astronomical toolkit.

3.6.2 GWTC-2 & GWTC-3: Population Emergence

The third observing run represented a quantum leap in both detector performance and scientific output. Divided into O3a (April–October 2019) and O3b (November 2019–March 2020, curtailed by the COVID-19 pandemic), this run benefited from substantial sensitivity improvements. The BNS range increased from approximately 80 Mpc in O2 to 120-140 Mpc in O3, corresponding to a factor of ∼2-3 increase in the observable volume of the universe. This enhanced sensitivity, combined with nearly a full year of observing time, enabled the detection of dozens of mergers and the emergence of genuine population statistics.

GWTC-2, covering O3a, added 39 new detections, while GWTC-3 brought the cumulative total to 90 GW events. This growing sample revealed the rich diversity of the compact binary population and challenged theoretical predictions in several important ways. The BH mass distribution showed unexpected features, including a possible gap or suppression around ∼45-50 $M_\odot$ and a dearth of systems in the predicted "pair-instability mass gap" above ∼65 $M_\odot$. The distribution of mass ratios indicated that Nature produces binaries across the full spectrum from nearly equal masses to highly asymmetric pairs.

Several individual detections from O3 deserve special mention for their unique contributions:

- **GW190412**: The first conclusively asymmetric BBH merger, with masses of approximately $30M_\odot$ and $8M_\odot$ (mass ratio $q \sim 0.27$). The strong asymmetry enabled the first unambiguous observation of higher-order multipole moments beyond the dominant quadrupole in a GW signal, providing independent confirmation of the binary nature of the source and enabling tests of general relativity inaccessible in more symmetric systems.
- **GW190425**: A BNS merger with an unusually high total mass of approximately $3.4\ M_\odot$, significantly heavier than the Galactic population of BNSs. The system's formation channel remains uncertain, with proposed scenarios including dynamical formation in dense stellar environments or substantial mass transfer between progenitor stars. This event expanded the known diversity of NS systems and has implications for equation of state constraints.
- **GW190521**: A massive BBH merger bringing together components of approximately $85M_\odot$ and $66M_\odot$ to form a ~$150M_\odot$ remnant, the first clear detection of an intermediate-mass BH. Both progenitors likely lie in or near the theoretically predicted pair-instability mass gap, where stellar evolution models predict no BHs should form directly from stellar collapse. The event has spurred numerous theoretical investigations into hierarchical merger scenarios, Population III star formation, and alternative formation channels. The signal also exhibited tentative evidence for orbital precession and a possible AGN electromagnetic counterpart, though both remain debated.
- **GW190814**: An extremely asymmetric merger pairing a ~$23M_\odot$ BH with a compact object of mass ~$2.6M_\odot$. The lighter component occupies the "mass gap" between the heaviest known NSs (~2.1-2.2$M_\odot$) and the lightest previously confirmed BHs (~$5M_\odot$), making it either an unusually massive NS that challenges equation of state models or an unexpectedly light BH that demands explanation from stellar evolution theory.
- **GW200105** and **GW200115**: The first confident detections of NS–BH (NSBH) binary mergers, detected within 10 days of each other in early January 2020. These events completed the trio of possible compact binary types (BBH, BNS, NSBH) observable through GW and provided the first observational constraints on the NSBH merger rate. The component masses and lack of electromagnetic counterparts suggest both NSs were likely tidally disrupted inside their companion BHs' event horizons, preventing the formation of massive accretion disks that might power detectable electromagnetic emission.

By the conclusion of O3, GW astronomy had clearly transitioned from novelty to maturity, with the sample size enabling meaningful statistical inference about formation channels, mass distributions, and spin alignments across the compact object population.

3.6.3 GWTC-4: The Era of Routine Discovery

The fourth observing run marks a paradigm shift in GW astronomy, the transition from remarkable individual discoveries to systematic population surveys. O4a (May 24, 2023–January 16, 2024) alone contributed 128 new GW candidates with astrophysical probability exceeding 0.5, bringing the cumulative total to 126 confident detections. This corresponds to a detection rate of approximately one event every two days of observing time, representing a roughly 58% contribution to all GW observations through 2024. At this rate, the sample doubles on timescales of months rather than years, enabling increasingly precise population statistics and rare-event studies.

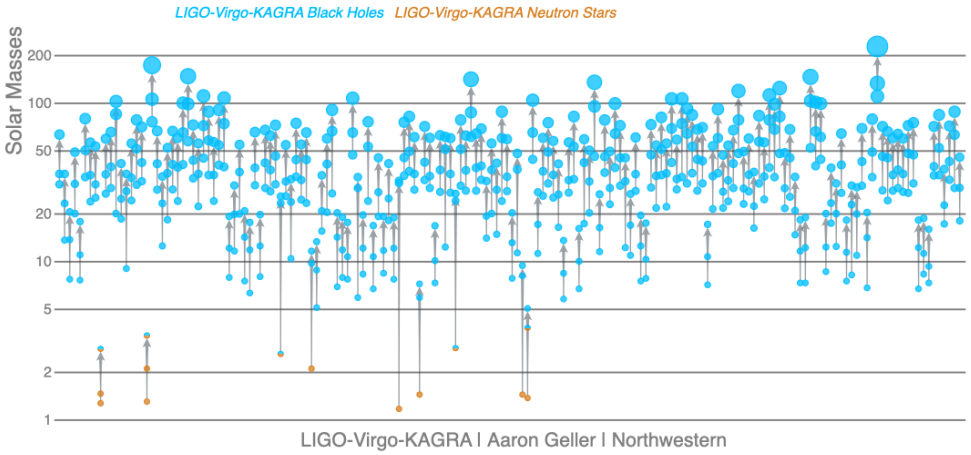

Figure 3.5: *Mass spectrum of compact binaries detected in GWTC-4. Individual detections are shown as points, with colors distinguishing BHs (blue) from NSs (orange). Arrows trace the progenitor-to-remnant mass evolution through merger. The population now spans from ~1.2$M_\odot$ NSs to BHs exceeding 100$M_\odot$, revealing rich structure including apparent gaps, pile-ups, and extending into the theoretically forbidden pair-instability regime.*

Beyond the sheer volume of detections, O4 has produced several events of exceptional scientific significance:

- **GW230529**: Detected on May 29, 2023, this merger involved two compact objects with masses firmly in the lower mass gap, the mysterious desert between the most massive NSs and the least massive BHs. With component masses constrained to 1.2–2.0 $M_\odot$ and 2.4–4.0 $M_\odot$, GW230529 represents either a pair of unusually massive NSs, light BHs, or potentially a mixed system. Despite being detected only by LIGO Livingston with modest signal-to-noise ratio (~11), its occupancy of this theoretically puzzling mass range makes it invaluable for constraining the maximum mass of NSs and the minimum mass of BHs formed through stellar collapse. The event directly probes the nuclear equation of state at supranuclear densities and the explosion mechanisms of core-collapse supernovae.
- **GW230814**: GW230814 was detected on August 14, 2023 with a signal-to-noise ratio of 42.4, making it the loudest GW signal in the GWTC-4.0 catalog. The signal

was recorded by the LIGO Livingston observatory and corresponds to a binary black hole merger with component masses $m_1 = 33.7^{+2.9}_{-2.2} M_\odot$ and $m_2 = 28.2^{+2.2}_{-3.1} M_\odot$, with small effective inspiral spin $\chi_{\rm eff} = -0.01^{+0.06}_{-0.07}$. The high signal-to-noise ratio enabled the first confident detection of an $\ell = |m| = 4$ mode in the inspiral signal. This detection supports tests of consistency between theoretical predictions and the observed waveform. Most tests show agreement with general relativity, though some deviations appear in the ringdown portion of the signal. Simulations indicate that similar deviations can arise from detector noise effects in general relativity signals. This observation demonstrates that single-detector signals, even with high signal-to-noise ratios, provide limited constraints on fundamental physics without multiple observatory data.

- **GW231123**: GW231123 was detected on November 23, 2023 by both LIGO observatories with a network signal-to-noise ratio of 22.5. The signal corresponds to a binary black hole merger with component masses $137^{+22}_{-17} M_\odot$ and $103^{+20}_{-52} M_\odot$ at redshift $0.39^{+0.27}_{-0.24}$ and luminosity distance 0.7-4.1 Gpc. Both black holes have high spins: $0.9^{+0.10}_{-0.19}$ and $0.80^{+0.20}_{-0.51}$ respectively. The primary black hole mass lies within or above the pair-instability mass gap (60-130 $M_\odot$), while the secondary spans this gap. An independent ringdown analysis supports the formation of a massive remnant around 200 $M_\odot$. Parameter estimates show systematic uncertainties between different signal models. This observation indicates black hole formation through channels beyond standard stellar collapse, and that intermediate-mass black holes can form via GW driven mergers.
- **GW250114**: The current record-holder for signal strength, detected on January 14, 2025, with an estimated network signal-to-noise ratio of approximately 80, three to four times louder than any previous detection and rivaling GW150914 in its clarity and scientific impact. The exceptional data quality of GW250114 enabled the first precise observational confirmation of the exponentially damped oscillations in the ringdown phase, where the remnant BH settles to its final state through characteristic QNMs. These ringdown oscillations are among the cleanest predictions of general relativity in the strong-field regime, depending only on the remnant's mass and spin, and GW250114's pristine signal allows multiple ringdown overtones to be resolved for the first time. This landmark detection pushes tests of BH spectroscopy and no-hair theorem violations to unprecedented precision, while its occurrence during O4 underscores how far detector sensitivity and analysis techniques have advanced.

The statistical power of GWTC-4 transforms questions that could previously only be addressed through individual events into population-level studies. We can now robustly measure the BH mass function across cosmic time, constrain the fraction of systems formed through isolated binary evolution versus dynamical capture in dense stellar environments, infer the typical natal kicks imparted during BH formation from the observed spin orientations, and trace the metallicity evolution of massive star formation

through the mass distribution of merging BHs. The steady accumulation of detections at approximately one event every two days means that rare subpopulations, extremely asymmetric binaries, highly spinning systems, precessing orbits, now contain sufficient members for dedicated study.

As O4 continues into its second phase (O4c), extending through November 2025, the catalog will continue to grow. The combination of increasing sample size, improving detector sensitivity, and refined analysis techniques positions the field to address fundamental questions about stellar evolution, compact object formation, the expansion history of the universe, and the validity of general relativity across scales and regimes inaccessible to any other observational probe. The transformation from discovery to routine observation represents not an ending but a new beginning for GW science.

4

Environmental Effects in LIGO-Virgo Compact Binary Mergers

Compact binary mergers are conventionally modeled as isolated systems in a vacuum, an effective and widely adopted approximation that forms the basis for current waveform models [71, 83, 84, 85]. While this simplification has been crucial for rapid parameter estimation, it inherently neglects the astrophysical environments where these binaries form and evolve. A growing body of evidence suggests that a significant fraction of compact binaries may originate in dense or gas-rich environments, including globular clusters (GCs) [86, 87, 88, 89, 90], nuclear star clusters (NSCs) [91, 92, 93], young massive clusters, and active galactic nucleus (AGN) accretion disks [94, 95, 96, 97, 98, 99, 100, 101, 102, 103, 104]. In such environments, binary dynamics can be altered, inducing orbital eccentricity, modifying mass ratios and spin orientations, and, in some cases, generating detectable electromagnetic counterparts [100, 105, 101].

The principal mechanisms for these environmental effects are accretion [106, 107, 108] and dynamical friction (DF) [109, 110, 111, 112, 113, 114]. Accretion can steadily increase component masses and influence spins, while DF, the gravitational drag force arising from a binary's motion through ambient matter, can alter the orbital decay rate [115, 105, 101, 102]. Both processes can induce subtle yet potentially measurable deviations in the GW phase and amplitude. Such deviations not only impact parameter estimation but could also bias high-precision tests of GR if unaccounted for [115, 105, 103, 104].

This chapter presents a systematic, Bayesian search for these environmental signatures in LIGO-Virgo data, incorporating all events from GWTC-1 and selected low-mass events from GWTC-2. We develop a model-agnostic framework to constrain the density of matter surrounding compact binaries, providing the first observational limits derived from a unified analysis of the detected population.

4.1 Astrophysical Environments

Compact binaries form and evolve in diverse astrophysical settings, each capable of imprinting characteristic signatures on their dynamics, masses, spins, and emitted GWs. The primary environments considered are dense stellar systems, gas-rich regions, and dark-matter halos. In these contexts, gravitational interactions, accretion, and dissipative forces can accelerate binary assembly, modify orbital parameters, and introduce subtle deviations in waveform morphology. A detailed understanding of these environments is therefore essential for both interpreting the observed BBH population and identifying environmental signatures in the data.

Dense stellar systems, such as GCs, NSCs, and young massive clusters, are characterized by frequent dynamical encounters. Here, BBHs can form dynamically via binary-single exchanges, three-body interactions, or gravitational capture [87, 93]. These processes often yield systems with measurable eccentricity in the LIGO-Virgo band and isotropic spin orientations. Furthermore, the presence of intermediate-mass BHs (IMBHs) can facilitate hierarchical mergers through Kozai-Lidov oscillations [93].

Gas-rich environments, most notably AGN disks, offer a distinct formation channel. Stellar-mass BHs or NSs embedded in these disks can form binaries through gas-driven migration and dissipative capture, which rapidly hardens the orbit [100, 101, 102]. Accretion in these environments can spin up the binary components, and DF may produce measurable waveform dephasing, leading to so-called "dirty waveforms" [103]. Similar mechanisms may operate in dense star-forming regions, where protostellar multiples evolve within gaseous molecular clouds [116].

Beyond baryonic matter, dark matter (DM) can also influence BBH evolution. The adiabatic growth of a BH within a dark matter halo can create a dense spike in the density profile [117, 118]. More diffuse substructures, such as minihalos, exert a weaker influence unless the binary remains embedded for a prolonged period [119]. Although current GW detections rarely permit localization within a specific environment, statistical trends in masses, spins, or eccentricities, such as those suggested for GW190521, can provide indirect evidence of environmental effects [100, 101]. Incorporating these environmental effects (EEs) is thus critical for accurate parameter estimation, robust tests of GR, and the correct astrophysical interpretation of the observed BBH mergers.

4.2 Environmental Effects

In astrophysical channels such as those involving dense stellar systems or gas-rich environments, the binary's evolution can take place within a medium capable of exerting additional long-range forces on the system. These interactions modify the inspiral through sustained exchanges of energy and angular momentum between the binary and its surroundings. Their impact is most pronounced during the early inspiral phase, when the orbital separation is large and the cumulative effect of environmental forces can produce measurable deviations from predictions based on vacuum wave-

form models. Two physical mechanisms dominate the environmental impact on binary evolution: DF and mass accretion. DF arises when the gravitational potential of each compact object perturbs the surrounding medium, generating an overdense wake behind it. The gravitational pull from this wake exerts a drag force that extracts orbital energy and angular momentum independently of GW radiation reaction. The corresponding energy loss rate can be expressed as

$$\dot{E}_{\rm DF} \approx \frac{4\pi\rho M^2 I(v,\eta)}{v}\frac{1-3\eta}{\eta}, \tag{4.1}$$

where ρ is the local medium density, $M = m_1 + m_2$ is the total mass, $\eta = m_1 m_2/M^2$ the symmetric mass ratio, $v = (\pi M_z f)^{1/3}$ the characteristic orbital velocity, $M_z = (1+z)M$ the redshifted total mass, f the GW frequency, and $I(v,\eta)$ an environment-dependent function determined by the properties of the medium. Mass accretion onto the binary components alters their masses during the inspiral, modifying the gravitational binding energy and consequently the orbital decay rate. Two regimes are typically considered. In *Bondi–Hoyle–Lyttleton accretion* (BHLA), relevant for collisional media, the compact object moves supersonically through a uniform medium and gravitationally focuses upstream material. The resulting mass growth rate is

$$\dot{M}_{\rm BHLA} \approx \frac{4\pi\rho M^2\lambda}{v^3}\frac{1-5\eta(1-\eta)}{\eta^3}, \tag{4.2}$$

where $\lambda \sim O(1)$ is a phenomenological factor. In contrast, *collisionless accretion* (CA) describes environments with large mean free paths, leading to

$$\dot{M}_{\rm CA} \approx \frac{16\pi\rho M^2}{v}\frac{1-3\eta}{\eta}. \tag{4.3}$$

The magnitude of these effects depends on the local density, composition, and velocity structure of the surrounding medium, as well as on the binary parameters.

4.2.1 Waveform Modeling with Environmental Effects

Within the PN framework, environmental modifications to the GW signal manifest primarily as corrections to the inspiral phase. Since both DF and accretion are more effective at large orbital separations, their contributions enter at negative PN orders, dominating the early inspiral. CA contributes at the -4.5PN order, whereas BHLA and DF contribute at the -5.5PN order. For a quasi-circular inspiral in a diluted environment, where environmental effects are subdominant to the leading vacuum radiation reaction, the frequency-domain GW phase can be written as

$$\phi^{\rm env}(f) = \phi^{\rm vac}(f) + \frac{3}{128\eta}\,\delta\Phi_k\, v^{k-5}, \tag{4.4}$$

where $\phi^{\rm vac}$ is the standard vacuum phase, $\delta\Phi_k$ is the environmental dephasing parameter, $v = (\pi M_z f)^{1/3}$, and k specifies the PN order of the correction ($k = -9$ for CA and $k = -11$ for DF and BHLA). The dephasing parameter can be related to physical properties of the environment through

$$\delta\Phi_k = -\beta_k \tilde{\rho} M^2, \tag{4.5}$$

with $\tilde{\rho} = \rho$ for CA, $\tilde{\rho} = \lambda\rho$ for BHLA, and $\tilde{\rho} = I\rho$ for DF. The dimensionless coefficients β_k, which encapsulate the dependence on the binary's mass ratio and the PN structure of the effect, are given by

$$\beta^{\rm CA}_{-9} = \frac{125\pi(1-3\eta)}{357\eta^2}, \tag{4.6}$$

$$\beta^{\rm BHLA}_{-11} = \frac{125\pi[1-5\eta(1-\eta)]}{1824\eta^4}, \tag{4.7}$$

$$\beta^{\rm DF}_{-11} = \frac{25\pi(1-3\eta)}{304\eta^3}. \tag{4.8}$$

The environmental phase shift modifies the frequency evolution of the signal, and thus the number of GW cycles observed in a given frequency band. As illustrated in Fig. 4.1, these phase accumulations manifest as progressive dephasing between environmental and vacuum waveforms throughout the inspiral. If neglected in template construction, these effects can introduce significant waveform mismatches, potentially biasing parameter estimation and reducing detection efficiency. Accurate modeling of $\delta\Phi_k$ and its dependence on astrophysical conditions is therefore essential for probing binary environments with GW observations.

4.2.2 The Mismatch Metric for Environmental Effects

Having defined the general mismatch metric, $\mathcal{MM}$, in Eq. 3.9, we now apply it to quantify the detectability of environmental modifications to GWforms. Specifically, we compute the mismatch between an environmentally modified waveform, $h_{\rm env}$, and its vacuum counterpart, $h_{\rm vac}$.

In the context of weak environmental influences, where effects like dynamical friction and accretion are subdominant to GW emission, the waveform accumulates a small, cumulative dephasing. This dephasing can be modeled as a PN, like correction to the Fourier-domain phase, proportional to the small parameter $\rho M^2 \ll 1$. The mismatch directly measures the observable consequence of this accumulated phase difference.

The characteristic behavior of the mismatch is illustrated in Fig. 4.2. The functional dependence of $\mathcal{MM}$ on the medium density ρ and the dephasing parameter $\delta\Phi_k$ reveals key observational insights. For a given detector sensitivity curve, the mismatch typically shows symmetric peaks around zero dephasing. However, the corresponding waveform durations are asymmetric: a negative dephasing parameter shortens the in-band signal, while a positive one lengthens it. Analyses using the aLIGO de-

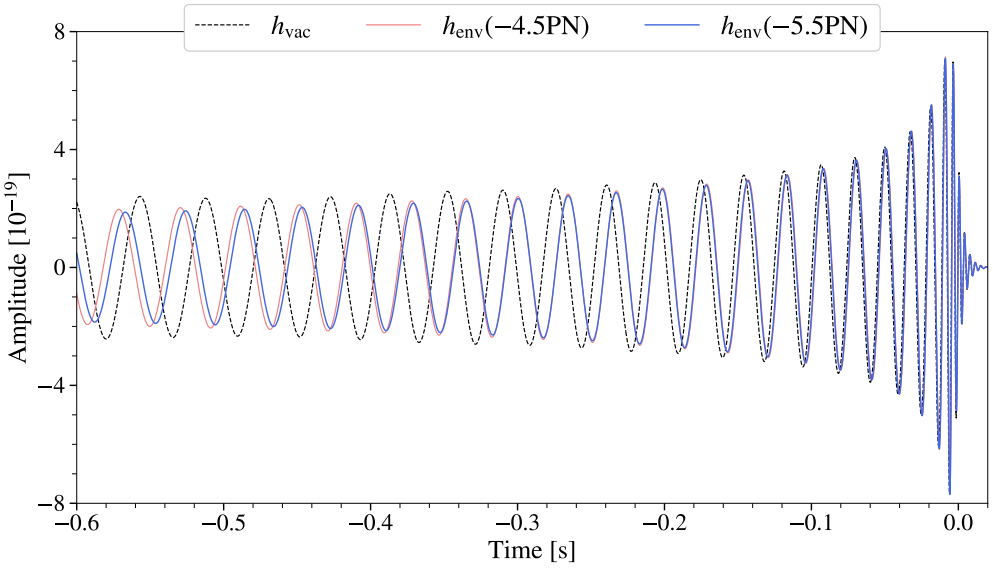

Figure 4.1: *Time-domain gravitational waveforms demonstrating environmental dephasing effects for a representative binary system. The vacuum waveform (black dashed) is compared against waveforms modified by collisionless accretion (CA, red) and combined dynamical friction/Bondi-Hoyle-Lyttleton accretion (DF/BHLA, blue). The progressive phase shift accumulates during the inspiral, with CA ($-4.5PN$) introducing earlier deviations due to its less negative PN order compared to DF/BHLA ($-5.5PN$). All waveforms are generated using the* `IMRPhenomPv2` *model with identical binary parameters, highlighting how environmental effects can be captured through the dephasing parameter $\delta\Phi_k$ in Eq. 4.5.*

sign sensitivity curve have demonstrated that low-mass systems, such as binary NSs, are particularly sensitive to even minute environmental dephasing. This is because they sweep through many more GW cycles in-band, allowing small phase deviations to accrue more significantly and thereby produce larger mismatches. By computing $\mathcal{MM}(h_{\rm vac}, h_{\rm env})$, we establish a direct, observational criterion: a mismatch significantly exceeding the 3% threshold indicates that environmental dephasing would be detectable, with low-mass binaries offering the most promising signals for distinguishing these effects from vacuum inspirals.

4.3 Bayesian Framework

We employ a Bayesian framework to measure the environmental dephasing parameter $\delta\Phi_k$ and to assess its statistical significance. The analysis follows a model-agnostic philosophy, in which deviations from the vacuum predictions of GR are encoded as an additive phase correction at a specified PN order k. This framework is implemented using the TIGER pipeline [120]. We use the phase model defined in Eq. 4.4:

$$\phi_{\rm env}(f) = \phi_{\rm vac}(f) + \frac{3}{128\eta}\,\delta\Phi_k\, v^{k-5},$$

where f is the GW frequency, η is the symmetric mass ratio, $v = (\pi M_z f)^{1/3}$ is the characteristic orbital velocity, and k specifies the PN order at which the environmental

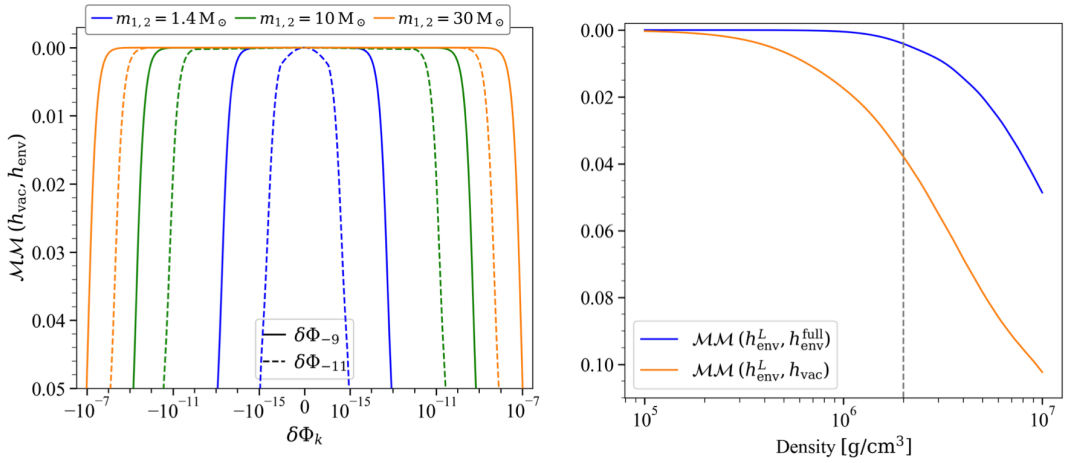

Figure 4.2: ***Right:*** *Mismatch as a function of the ambient medium density ρ for a GW150914-like binary, calculated using the event's actual noise power spectral density. The vertical line indicates the approximate 90% upper bound on ρ from our analysis (see Fig.* **??**) *for dynamical friction (DF) and black hole mass loss accretion (BHLA). The curves $h^L_{\rm env}$ and $h^{\rm full}_{\rm env}$ correspond to the environmentally perturbed waveform at linear order in ρM^2 and the full numerical solution, respectively.* ***Left:*** *Mismatch between vacuum ($h_{\rm vac}$) and environmentally modified ($h_{\rm env}$) waveforms as a function of the dephasing parameter $\delta\Phi_k$ for a set of non-spinning, equal-mass binaries. The solid and dashed lines represent the effects of cloud accretion (CA, $k = -9$) and the combined effects of BHLA or DF ($k = -11$), respectively.*

effect enters. For example, $k = -9$ corresponds to CA, while $k = -11$ describes both DF and BHLA. We test two competing hypotheses:

- $\mathcal{H}_{\rm vac}$: the vacuum model, in which no environmental effects are present ($\delta\Phi_k = 0$);
- $\mathcal{H}_{\rm env}$: the environmental model, in which $\delta\Phi_k$ is a free parameter describing phase deviations at PN order k.

A zero-centered uniform prior is adopted for $\delta\Phi_k$, wide enough to encompass physically plausible values while ensuring numerical stability and convergence of the sampling algorithm. This choice is particularly relevant for low-mass systems, whose longer inspiral durations make them more sensitive to cumulative dephasing.
The relative statistical support for the two hypotheses is quantified via the Bayes factor,

$$B^{\rm env}_{\rm vac} = \frac{p(d \mid \mathcal{H}_{\rm env})}{p(d \mid \mathcal{H}_{\rm vac})}, \tag{4.9}$$

where $p(d \mid \mathcal{H})$ denotes the marginal likelihood of the data d under hypothesis $\mathcal{H}$. Both Bayes factors and posterior distributions are computed using nested sampling algorithms.
Waveform generation (see Section 3.5) is performed with the `IMRPhenomPv2` model for BBH systems, which incorporates spin precession, and with `IMRPhenomPv2_NRTidalv2` for BNS systems, which also includes tidal deformability. A lower frequency cutoff of 20 Hz is adopted in all analyses, except for GW170817 where a cutoff of 23 Hz is used due to data-quality limitations.

The posterior distributions of $\delta\Phi_k$ provide direct constraints on the magnitude of environmental dephasing. For high SNR events with long inspiral phases in the detectors' sensitive band, the posteriors typically differ from the prior, enabling the derivation of meaningful upper bounds on environmental effects. In contrast, for low-SNR events or those dominated by the merger–ringdown regime, the resulting constraints remain largely prior-dominated.

4.4 Results

Applying the framework outlined in the previous section to events from GWTC-1 and selected events from GWTC-2 catalogs yields no statistically significant evidence for environmental effects. As shown in Table 4.1, the logarithmic Bayes factors $\log_{10} B^{\rm env}_{\rm vac}$ are negative in all cases for both $k = -9$ and $k = -11$ dephasing parameters, revealing that none of the observed GW signals provide support for deviations from the isolated, vacuum model. Nevertheless, the resulting upper limits translate into astrophysically relevant constraints on the density and composition of the medium surrounding compact binaries.

4.4.1 Evidence for Environmental Effects

Table 4.1 reports the computed Bayes factors for each analyzed event. For GW170729

Table 4.1: *Logarithmic Bayes factors* $\log_{10} B^{\rm env}_{\rm vac}$ *for the environmental versus vacuum models, for PN orders* $k = -9$ *and* $k = -11$.

Event	$\log_{10} B^{\rm env}_{\rm vac}$ $(k = -9)$	$\log_{10} B^{\rm env}_{\rm vac}$ $(k = -11)$
GW150914	-2.09	-3.30
GW151226	-4.20	-5.52
GW170104	-1.29	-3.33
GW170608	-4.95	-6.17
GW170809	-1.91	-2.59
GW170814	-3.17	-2.81
GW170817	-5.45	-6.47
GW190425	-10.0	-11.6
GW190924	-5.5	-6.4

and GW170823, the posterior distributions of the dephasing parameter $\delta\Phi_k$ were uninformative, closely mirroring the prior due to the low inspiral SNR. By contrast, GW151012 and GW170818 analyses failed to converge, likely owing to difficulties navigating a challenging posterior landscape.

4.4.2 Upper Limits on Environmental Density

Since no statistically significant environmental effect was detected, the posterior distributions for $\delta\Phi_k$ are used to place upper bounds on the effective ambient density $\tilde{\rho}$. These bounds represent the maximum density that could be present without producing observable dephasing in the detected signals. To compute these limits, we

map posterior samples of $\delta\Phi_k$ to density using Eq.4.5, restrict to physically motivated $\delta\Phi_k < 0$ values, and extract their 90% credible upper quantiles. The resulting constraints, shown in Fig. 4.3, span $\tilde{\rho} \lesssim (2\times10^1)$–$(2\times10^6)\ \mathrm{g/cm^3}$ across most events. While such densities are far above those expected in typical astrophysical environments, they nevertheless exclude extreme scenarios, for instance, binaries embedded in highly compact gas configurations analogous to stellar fragmentation channels. The tightest constraint arises from GW170817, whose long inspiral enables sensitivity to even small cumulative phase shifts, yielding $\tilde{\rho} \lesssim 21\ \mathrm{g/cm^3}$, comparable to the density of gold. A clear trend emerges: low-mass binaries (e.g., GW170817, GW151226, GW170608), with many inspiral cycles in band, provide the strongest constraints, whereas high-mass mergers with limited inspiral leverage return only weak, essentially non-informative bounds.

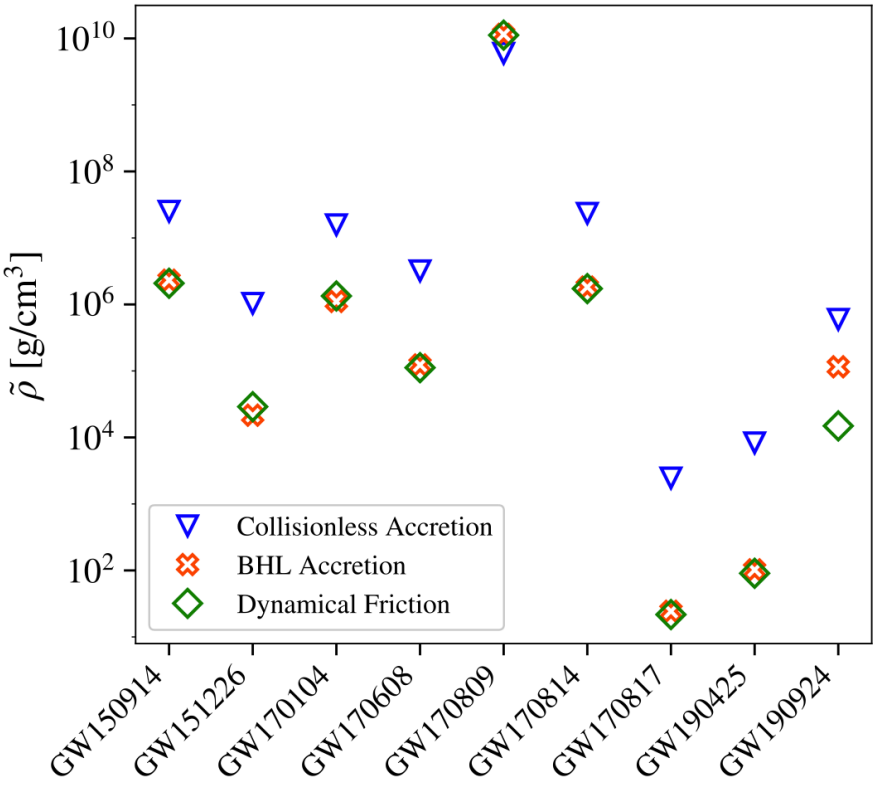

Figure 4.3: *90% credible upper bounds on environmental density $\tilde{\rho}$ for CA, BHLA, and DF , derived from posterior distributions of $\delta\Phi_k$. The tightest constraints are from low-mass events, especially GW170817.*

4.4.3 Systematic Effects and Parameter Biases

Even for environmentally perturbed signals that remain statistically indistinguishable from vacuum waveforms—indicated by Bayes factors $\log_{10} B^{\mathrm{env}}_{\mathrm{vac}} \lesssim 0$—the use of vacuum models in parameter estimation can nonetheless introduce systematic biases in the inferred intrinsic binary parameters. These biases, summarized in Fig. 4.4, exhibit consistent trends across all cases. First, the chirp mass is systematically overestimated

when environmental dephasing is present but unmodeled: the parameter estimation process, constrained by vacuum templates, compensates for the enhanced orbital decay by inferring a higher total mass. Second, the mass ratio tends to be underestimated under the same incorrect vacuum assumption. Third, the effective aligned spin, $\chi_{\rm eff}$, is biased toward higher values when environmental effects are neglected. Our analysis shows, however, that for the current population of detected events, environmental effects are too weak to produce statistically significant biases or to compromise tests of general relativity. The consistent absence of evidence for environmental dephasing ($\log_{10} B^{\rm env}_{\rm vac} \lesssim 0$ across all sources) confirms that existing vacuum waveform models remain sufficient for astrophysical inference and fundamental physics tests at present detector sensitivities.

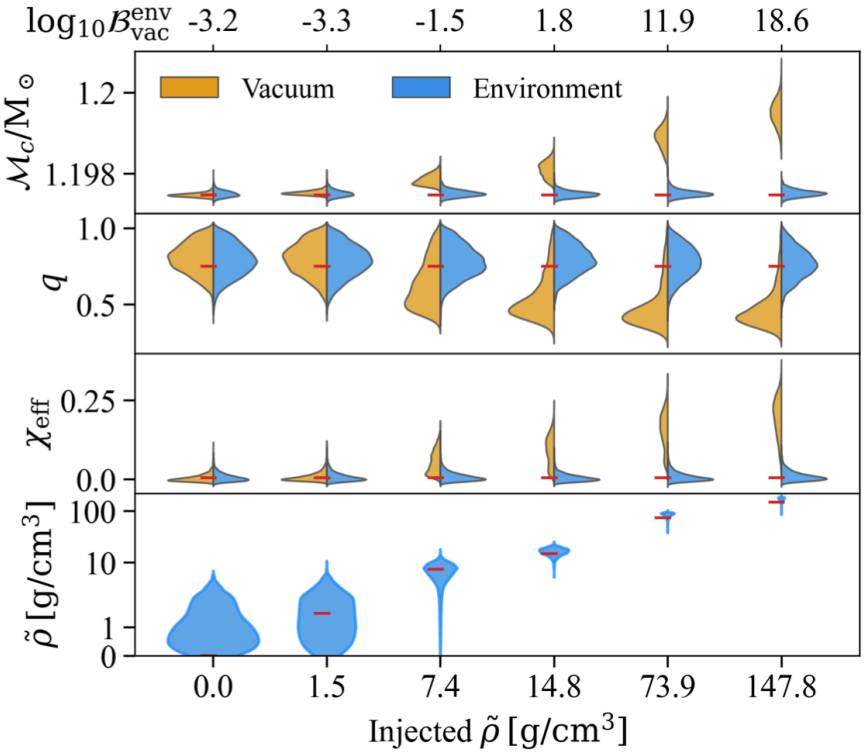

Figure 4.4: *Posterior distributions for the chirp mass ($\mathcal{M}_c$), mass ratio (q), and effective spin ($\chi_{\rm eff}$) recovered using vacuum templates ($h_{\rm vac}$) compared to environment-aware templates ($h_{\rm env}$) with non-zero $\delta\Phi_{-11}$. The analysis uses injected GW170817-like waveforms modified by dynamical friction effects across a range of environmental densities (bottom x-axis), analyzed with the aLIGO design sensitivity curve. The top x-axis shows the logarithmic Bayes factor $\log_{10} B^{\rm env}_{\rm vac}$ comparing the evidence for environmental versus vacuum models. Small red markers indicate the true injected parameter values, revealing systematic biases in parameter recovery when environmental effects are present but unmodeled.*

These systematic trends nonetheless highlight the importance of accounting for potential environmental influences in precision GW astronomy. This consideration is especially relevant for low-mass systems, whose extended in-band inspiral makes them particularly susceptible to subtle dephasing effects. As detector sensitivity continues to improve, mitigating such systematic uncertainties will become essential for reliable astrophysical and fundamental-physics inference.

4.5 Prospects

To assess the detectability of environmental effects with current and future observatories, we performed a series of injection studies. Figure 4.5 summarizes the results, contrasting the capabilities of Advanced LIGO with the potential of next-generation detectors.

Our analysis with the Advanced LIGO (aLIGO) design sensitivity, using zero-noise injections, reveals distinct detection thresholds across different binary masses. The logarithmic Bayes factor, plotted as a function of ambient density (Fig. 4.5, left), shows that dynamical friction (DF) becomes detectable for effective densities of order $\tilde{\rho} \gtrsim (10, 4 \times 10^4, 10^6)\ \mathrm{g/cm^3}$ for GW170817-, GW170608-, and GW150914-like systems, respectively. Cloud accretion (CA) requires densities roughly one to two orders of magnitude larger to produce a comparable imprint, consistent with its weaker dephasing efficiency. While aLIGO can already place meaningful constraints—for instance, ruling out the dynamical fragmentation channel that requires densities $\gtrsim 10^7\ \mathrm{g/cm^3}$—the detection of more tenuous environments, such as thin accretion disks or dark matter overdensities, remains beyond its reach.

Third-generation ground-based observatories will substantially improve this sensitivity. The Einstein Telescope (ET), with a planned low-frequency cutoff of ~ 5 Hz, will probe DF and Bondi-Hoyle-Lyttleton accretion (BHLA) in environments as dilute as $\tilde{\rho} \sim 10^{-3}\ \mathrm{g/cm^3}$ (Fig. 4.5, right). This sensitivity would enable the detection of binaries embedded in dense nuclear accretion disks, superradiant boson clouds, or regions of dark matter overdensity.

Decihertz observatories such as B-DECIGO promise an even more transformative leap. Their low-frequency reach (~ 0.1 Hz) allows for precision measurements during the long inspiral phase, potentially constraining environmental effects down to $\tilde{\rho} \sim 10^{-12}\mathrm{g/cm^3}$. This would cover most astrophysically motivated scenarios, including accretion-disk models, bosonic field condensates, and cold dark matter spikes around massive black holes.

Our Bayesian forecasts yield density thresholds that are two to three orders of magnitude more conservative than earlier Fisher-matrix estimates. This discrepancy highlights the importance of a complete analysis: the Bayesian evidence naturally incorporates an Occam's razor penalty for the more complex environmental model, accounts for degeneracies with intrinsic binary parameters, and rigorously handles realistic noise properties. Consequently, while Fisher matrix calculations provide a useful first estimate, our full Bayesian inference offers more reliable and robust projections for future detectability.

4.6 Conclusion

Our systematic search for environmental effects in LIGO-Virgo data has yielded no significant detections, confirming that current vacuum waveform models remain ade-

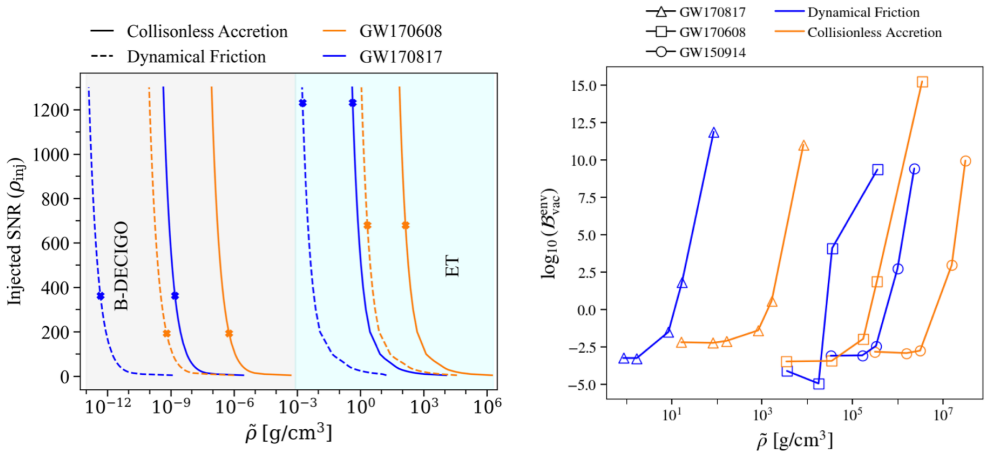

Figure 4.5: ***Left:*** *Logarithmic Bayes factor* $\log_{10} B^{\rm env}_{\rm vac}$ *as a function of ambient density* $\tilde{\rho}$*, showing the detectability of environmental effects using the aLIGO design sensitivity curve. The curves represent results for GW150914-, GW170608-, and GW170817-like injections in zero-noise realizations. The BHLA curve is omitted as it closely follows the DF trajectory.* ***Right:*** *Required signal-to-noise ratio (SNR) to achieve* $\log_{10} B^{\rm env}_{\rm vac} = 3$ *as a function of density, for the Einstein Telescope (ET, cyan band) and B-DECIGO (gray band). Dots represent the expected SNR for each system if observed by these future detectors. The BHLA curve is omitted due to its similarity with DF.*

quate for astrophysical inference and GR tests with present sensitivities.

Despite this null result, we have established the first population-wide upper limits on ambient density, with the most stringent constraint from GW170817 ruling out $\tilde{\rho} \gtrsim 21\ \mathrm{g/cm^3}$ for dynamical friction. While sub-threshold environmental effects could potentially bias parameter estimation, our analysis shows they remain undetectable in current observations.

Looking ahead, third-generation detectors will improve sensitivity by 9-15 orders of magnitude in density reach, transforming environmental searches from setting upper limits to direct detection and characterization of binary formation environments.

This work establishes the foundational methodology and current observational bounds for environmental GW astronomy, paving the way for future studies as detector sensitivity continues to improve.

5

Ringdown Data Analysis of O4 data

5.1 Overview of the BH Spectroscopy Program

The BH spectroscopy program, introduced in Section 1.1.3, aims to use the *ringdown* signal of a BH as a direct probe of its nature. As already mentioned in Section 1.3, the no-hair theorem dictates that an isolated, stationary BH in GR is uniquely described by its mass and spin. The final vibrations of the remnant BH, as it settles into this Kerr state, are described by a spectrum of QNMs, a direct consequence of BH stability as detailed in Section 1.3.2. The primary goal of spectroscopy is to measure these modes: a detection of the fundamental mode allows for an estimate of the mass and spin, while the measurement of a second, distinct mode provides a test of the Kerr hypothesis, as any deviation could indicate new physics. In practice, however, translating this theoretical concept into a robust GW data analysis pipeline is fraught with challenges. The idealized model of extracting clean, damped sinusoids from the data becomes highly non-trivial when confronted with real signals of low SNR, complex morphology, and significant uncertainties from the preceding inspiral and merger phases. This chapter lays the foundation for the ringdown analyses presented in this thesis. We begin by establishing the core methodological framework in Section 5.2, detailing the statistical and computational principles of ringdown data analysis. We then delve into ringdown parametrizations (see Section 5.3) used to model the QNM spectrum, a discussion of the ringdown systematics (see Section 5.4) arising from modeling choices and data quality issues, and a review of the detection criteria (see Section 5.4.3) employed to claim a robust QNM detection. All ringdown analyses presented here were conducted using the `pyRing` pipeline, which implements the Bayesian time-domain framework for ringdown inference [121, 122]. Following this methodological basis, we summarize past observational constraints and present new results from ringdown analyses of selected O4a events. We highlight key findings for special events such as GW230814 and

GW231123 and conclude with a detailed analysis of GW250114, the loudest ringdown observed to date. For this event, we report the first clear observation of two distinct QNMs and perform a test of the BH area law, obtaining the most stringent bound on its validity to date.

5.2 Formulation of Ringdown Data Analysis

The detection and characterization of ringdown signals in GW data can be pursued through two distinct paradigms: a *full-signal analysis* that models the entire binary coalescence (inspiral, merger, and ringdown), or a *ringdown-only analysis* that isolates and studies the post-merger damped sinusoids. In this work, we focus on the latter, aiming to characterize the remnant BH by fitting only the data following the merger. The primary objective of a ringdown-only analysis is to model the post-merger relaxation of the BH using a superposition of QNMs, as predicted by perturbation theory. Conceptually, this involves selecting a start time t_0 and analyzing the subsequent data segment. A common but flawed implementation is to simply zero-out the data before t_0 and perform a standard frequency-domain analysis. This method suffers from the *Gibbs phenomenon*, where the abrupt start time introduces spurious power across all frequencies. Furthermore, the Fourier transform of a damped sinusoid has a finite width, causing the ringdown's power to "leak" into frequency bands associated with the inspiral, and vice-versa. This frequency-mixing obscures the physical interpretation of the results and can bias parameter estimates [122]. To overcome these limitations, we employ a rigorous time-domain formalism, which is detailed in the following sections.

5.2.1 Bayesian Inference for Ringdown Analysis

We apply the general Bayesian framework of Section 3.2.1 to ringdown signals, analyzing only post-merger data $\mathbf{d}_{[t_0,t_0+T]}$. The posterior distribution for ringdown parameters $\boldsymbol{\theta}$ is:

$$p(\boldsymbol{\theta}|\mathbf{d},\mathcal{H}) \propto p(\mathbf{d}|\boldsymbol{\theta},\mathcal{H})\, p(\boldsymbol{\theta}|\mathcal{H}), \tag{5.1}$$

where the likelihood $p(\mathbf{d}|\boldsymbol{\theta},\mathcal{H})$ must account for the truncated time segment, introducing boundary correlations in the noise covariance matrix.

5.2.2 Time-Domain Likelihood for Truncated Data

Standard frequency-domain analyses require data segments where signals are isolated from edges to allow smooth windowing. For ringdown analysis, however, the signal begins at the segment boundary t_0, creating a challenge (Fig. Figure 5.1): windows extending before t_0 contaminate the ringdown with inspiral-merger content, while windows starting at or after t_0 corrupt the crucial ringdown onset. We overcome these limitations using a time-domain approach that operates directly on the truncated segment $[t_0, t_0+T]$. For wide-sense stationary noise, the covariance matrix $\mathbf{C}$ is a symmetric

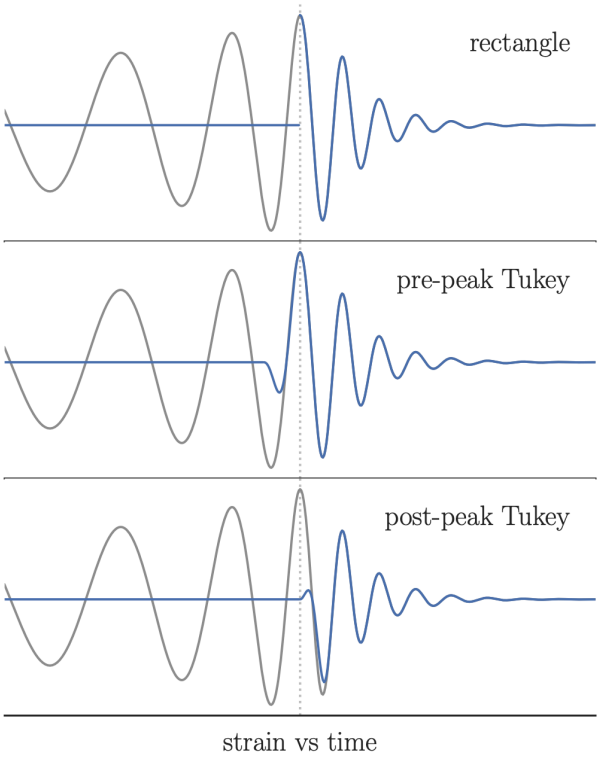

Figure 5.1: *Frequency-domain challenges for ringdown analysis. Taken from Ref.* [123].

Toeplitz matrix with elements $C_{ij} = \rho(|t_i - t_j|)$. The log-likelihood is:

$$\log p(\mathbf{d}|\boldsymbol{\theta}) = -\frac{1}{2}\left(\mathbf{d} - \mathbf{h}(\boldsymbol{\theta})\right)^{\top} \mathbf{C}^{-1} \left(\mathbf{d} - \mathbf{h}(\boldsymbol{\theta})\right) + \text{constant}. \tag{5.2}$$

Fig. Figure 5.2 shows this method in practice, with clean truncation at t_0 separating ringdown from preceding phases.

Autocorrelation Function Estimation

We estimate the autocorrelation function (ACF) from off-source data under wide-sense stationarity using standard procedures [124]:

1. Select a long stationary segment ($\bar{T} \sim \mathcal{O}(10^3)$ s)
2. Divide into N_s sub-chunks ($T_s = 4$ s typically)
3. Compute ACF estimates for each sub-chunk
4. Average to produce final low-variance ACF estimate

For discrete data n_j of length N, we use the unbiased estimator:

$$\hat{C}(m) = \frac{1}{N-m} \sum_{j=0}^{N-m-1} n_j n_{j+m}, \tag{5.3}$$

truncated to length T encompassing the ringdown signal.

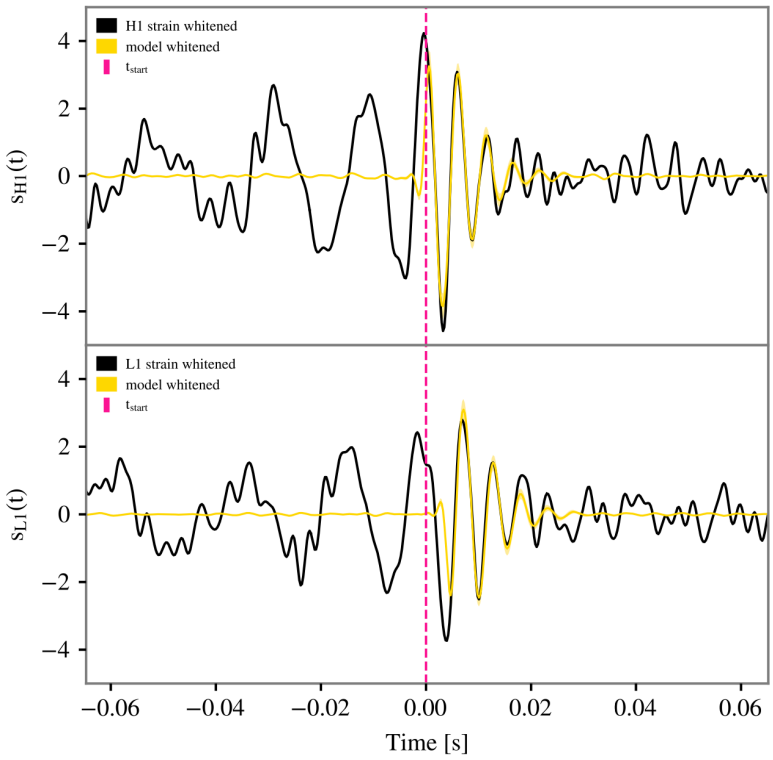

Figure 5.2: *Whitened waveform reconstruction demonstrating clean truncation at t_0.*

Computational Implementation

For efficiency, we factorize the covariance matrix using Cholesky decomposition:

$$\mathbf{C} = \mathbf{L}\mathbf{L}^\top, \tag{5.4}$$

enabling computation of whitened quantities $\bar{\mathbf{x}} = \mathbf{L}^{-1}\mathbf{x}$. This transforms the likelihood evaluation into a simple inner product:

$$\langle \mathbf{x}|\mathbf{y}\rangle\Big|_{t_0}^{t_0+T} = \mathbf{x}^\top \mathbf{C}^{-1}\mathbf{y} = \bar{\mathbf{x}}^\top \bar{\mathbf{y}}, \tag{5.5}$$

with corresponding matched-filter SNR:

$$\mathrm{SNR}(\mathbf{x},\mathbf{y})\Big|_{t_0}^{t_0+T} = \frac{\langle \mathbf{x}|\mathbf{y}\rangle\Big|_{t_0}^{t_0+T}}{\sqrt{\langle \mathbf{y}|\mathbf{y}\rangle\Big|_{t_0}^{t_0+T}}}. \tag{5.6}$$

5.2.3 Data Conditioning

Data conditioning, the selection of analysis segments and application of preprocessing steps like downsampling, filtering, and line cleaning, is essential before Bayesian inference on GW data. These steps reduce computational costs and improve likelihood evaluation quality, with particular importance for ringdown analyses. Public LVK data releases provide strain data at 4096 Hz or 16384 Hz, both high-pass filtered

at 8 Hz, with additional anti-aliasing applied to the 4096 Hz data. Calibrated data include built-in calibration filters and instrumental line subtraction. While data cleaning effects are well-characterized for frequency-domain analyses, their impact on time-domain ringdown likelihoods requires special attention. Previous work has quantified effects of downsampling, filtering, and line cleaning in ringdown contexts [125], while other studies have compared noise estimation strategies [126]. Once the ringdown start time t_0 is determined, two critical choices must be made: the segment duration and the sampling rate. Although one might expect the segment duration to match the signal's intrinsic decay timescale, this proves insufficient in practice. Detector noise is colored and Gaussian, creating temporal correlations that extend the effective segment length required for proper whitening. These correlations are particularly pronounced when narrow spectral lines are present in the noise PSD. Using segments that are too short artificially broadens posterior distributions, leading to overestimates of statistical uncertainty [127]. The choice of sampling rate involves a trade-off between computational efficiency and analysis fidelity. Lower sampling rates reduce computational costs but risk undersampling the signal. A practical guideline suggests that downsampling is safe when the Lorentzian peak associated with the fastest-decaying mode becomes negligible at the Nyquist frequency.[1] However, the downsampling method itself introduces complications: standard anti-aliasing filters can distort frequencies well below the Nyquist limit, and when significant signal power exists near Nyquist, these filters can produce template-data mismatches that measurably alter posterior distributions [125, 126]. These considerations explain why standard LVK ringdown analyses typically adopt conservative sampling rates (e.g., 4096 Hz in O3) [128, 129, 130, 131]. Alternative approaches include avoiding filtering entirely or constructing the autocorrelation function from a modified PSD that excludes affected frequency components [125].

5.3 Ringdown Parameterizations

The GW signal during the ringdown phase can be modeled as a superposition of QNMs, characteristic damped oscillations of the remnant BH. Different *ringdown models* parameterize these modes in terms of inferable parameters $\boldsymbol{\theta}$, with the choice of parameterization critically impacting the scientific inference. Restrictive models reduce flexibility and risk biasing results if their underlying assumptions are violated. Conversely, more general parameterizations can reveal additional physics but incur increased statistical uncertainty from additional degrees of freedom [129, 132, 133, 122, 124, 134, 135].

[1] The Nyquist frequency $f_{\mathrm{Nyq}} = f_s/2$ defines the maximum unambiguous frequency for sampling rate f_s.

5.3.1 Damped Sinusoids

The most agnostic approach, labeled *Damped Sinusoids*, represents the signal as a superposition of exponentially damped oscillations:

$$h_+ - ih_\times = \sum_j h_j, \quad h_j \equiv A_j\, e^{-(t-t_0)/\tau_j} e^{-2\pi i f_j (t-t_0) + i\phi_j}. \tag{5.7}$$

This parameterization captures the general features of ringdown signals without assuming relationships between modes, making it suitable for testing fundamental BH properties or searching for deviations from GR predictions. It can be motivated theoretically by the boundary conditions of BH perturbations [136, 137] or observationally by the exponentially decaying behavior of measured signals [129, 128]. In the stationary relaxation regime, where QNM amplitudes and the remnant mass and spin have stabilized, one can assume constant amplitudes A_j. The free parameters $\{f_j, \tau_j, A_j, \phi_j\}$ fully describe the signal within this model.

5.3.2 Kerr Template

Assuming the remnant is a Kerr BH, the QNM spectrum is uniquely determined by its mass M_f and spin a_f Section 1.3.1. The strain can be expressed as:

$$h_+ - ih_\times = \frac{M_f}{D_L} \sum_{l=2}^{\infty} \sum_{m=-l}^{l} \sum_{n=0}^{\infty} \left(h^+_{lmn} + h^-_{lmn} \right), \tag{5.8}$$

with

$$h^+_{lmn} = A^+_{lmn}\, {}_{-2}S_{lmn}(\iota, \varphi)\, e^{i[(t-t_0)\tilde{\omega}_{lmn} + \phi^+_{lmn}]}, \tag{5.9}$$

$$h^-_{lmn} = A^-_{lmn}\, {}_{-2}S_{l-mn}(\iota, \varphi)\, e^{-i[(t-t_0)\tilde{\omega}^*_{lmn} - \phi^-_{lmn}]}, \tag{5.10}$$

where $\tilde{\omega}_{lmn} = \omega_{lmn} + i/\tau_{lmn}$ is the complex ringdown frequency, expressed as a function of the remnant BH mass and spin, $\tilde{\omega}_{lmn} = \tilde{\omega}_{lmn}(M_f, a_f)$. The amplitudes $A^\pm_{lmn}$ and phases $\phi^\pm_{lmn}$ characterize the excitation of each mode. For binaries with spins aligned with the orbital angular momentum, reflection symmetry implies $A^-_{lmn} = (-1)^l A^{+*}_{lmn}$, halving the number of free parameters per mode. Here ι denotes the inclination of the BH final spin relative to the observer's line of sight, while φ is the azimuthal angle in the BH frame. ${}_{-2}S_{lmn}$ are the spin-weighted spheroidal harmonics and t_0 is a reference start time. Following the conventions of Lim et al. [138], $m > 0$ indices denote co-rotating modes, while counter-rotating modes are labeled by $m < 0$. Counter-rotating modes are weakly excited in the post-merger phase for typical LIGO-Virgo-Kagra binaries [139], though their potential relevance remains debated [140, 138]. This *Kerr* parameterization reduces the free parameters to $\{M_f, a_f, A_{lmn}, \phi_{lmn}\}$ and has been extensively applied to numerical relativity simulations [141, 142]. The model encodes the essential features of Kerr perturbations while retaining sufficient agnosticism to extract

significant information from ringdown signals.

5.3.3 `KerrPostmerger`

For times near the merger, constant-amplitude QNM models face significant limitations due to nonlinearities and transient effects that dominate the early post-merger phase. The `KerrPostmerger` model (introduced in [143]) addresses these limitations by incorporating time-dependent amplitudes and phases calibrated to numerical relativity simulations. This approach models the entire post-peak emission using a spherical decomposition of dominant modes (up to $l = 5$) with a resummation strategy that captures nonlinear contributions and overtone effects. The model employs phenomenological time-dependent functions:

$$A_{lm} = A_{lm}(t; m_1, m_2, \chi_1, \chi_2), \quad \phi_{lm} = \phi_{lm}(t; m_1, m_2, \chi_1, \chi_2), \tag{5.11}$$

and crucially accounts for time delays between different mode peaks. By including progenitor information (masses m_1, m_2 and spins χ_1, χ_2), it bridges IMR and ringdown-only analyses, enabling inference of initial binary parameters from the ringdown signal. This framework allows extraction of larger SNR from extended portions of the post-merger signal, though with reduced sensitivity to certain exotic deviations from Kerr relaxation compared to more agnostic models. The `KerrPostmerger` approach forms the basis for IMRPhenomTPHM [80] and has been systematically characterized in GWTC-3 analyses [133].

5.4 Systematic Challenges in Ringdown Analysis

BH spectroscopy from binary mergers faces fundamental systematic challenges that limit the precision and physical interpretation of measurements. These arise from the complex physical transition from merger to ringdown and the practical difficulties of analyzing real detector data.

5.4.1 The Start Time and Dynamical Remnant Problem

The primary systematic uncertainty arises from the ill-defined nature of the ringdown start time t_{start}. Unlike a sharp phase transition, the onset of the ringdown regime represents an approximate selection of the relaxation epoch rather than a physically distinct boundary. A more fundamental challenge stems from the intrinsically dynamical nature of the post-merger system. During the ringdown phase, we observe not a stationary Kerr BH subjected to well-defined perturbations, but rather a highly dynamical spacetime evolving toward equilibrium. The mass and spin of the remnant BH vary continuously during the early stages of this relaxation process. This distinction separates the problem of fitting the post-peak waveform with phenomenological damped sinusoids from the task of extracting the true physical vibrational spectrum

of the BH. These challenges originate in the complex physical evolution of BBH coalescence. The system undergoes an inherently non-linear transition from dynamical merger to quasi-stationary ringdown. Following inspiral, the waveform reaches its amplitude peak as the two horizons merge, producing an enormous burst of gravitational radiation dominated by non-linear effects. A dynamical horizon forms, far more complex than a stationary Kerr BH, which subsequently relaxes toward equilibrium. As the system evolves past the peak, the remnant approaches a quasi-stationary state characterized by QNM ringing. This physical evolution creates the fundamental tension between SNR, which favors early times, and theoretical validity, which requires later times when the system has stabilized. As illustrated in Fig. Figure 5.4, the choice of $t_{\rm start}$ dramatically affects both the quality and interpretation of ringdown fits. At early start times ($t_{\rm start} = 0M$), strong nonlinearities and evolving remnant parameters lead to poor agreement with perturbative predictions. By $t_{\rm start} = 15M$, the fits improve substantially but systematic residuals remain visible. At $t_{\rm start} = 30M$, the Kerr model provides excellent agreement with numerical relativity, demonstrating that the system has reached the perturbative regime, but this comes at the cost of substantial SNR loss.

5.4.2 Practical Start Time Selection

In our ringdown analyses with `pyRing`, the analysis start time is defined relative to a reference time t_0 determined through a robust statistical procedure. We begin by drawing $N = 10,000$ samples from the GR IMR parameter estimation posteriors, generating corresponding waveforms for each sample. For each waveform, we compute the peak time of the strain $h_+^2 + h_\times^2$, building a distribution of t_0 values. For most events, we use the NRSur7dq4 waveform [73]; when unavailable, we employ IMRPhenomXPHM [76]. We employ different start time strategies depending on the ringdown model: **`KerrPostmerger`:** As shown in Fig. Figure 5.3, we use the 90% credible interval of the peak time distribution (gray shaded region) divided into 9 segments (green vertical lines) to define our start time grid. The reference time t_0^{22} is computed as the peak of the h_{22} mode, consistent with its NR calibration. A critical optimization ensures that the spacing between start times exceeds the ringdown sampling rate, preventing redundant analyses while maintaining adequate coverage of the uncertainty range. **`Damped Sinusoids` and `Kerr`:** For these models, we use a two-tiered grid approach: a wide grid with $5M$ steps from $-10M$ to $20M$ relative to t_0, supplemented by a finer grid with $2M$ steps centered around t_0 to provide enhanced resolution near the expected validity regime. We analyze multiple starting times across all models to verify consistency with GR predictions, but report results at a single characteristic time $t_{\rm nom}$ set by each model's regime of validity: $t_{\rm nom} = 10M$ for `Damped Sinusoids` and `Kerr` templates, and $t_{\rm nom} = 0M$ for `KerrPostmerger` due to its phenomenological nature. Due to the truncated time-segment formulation [123], the sky location is fixed to the maximum-likelihood value from the full IMR analysis. As illustrated in Fig. Figure 5.4, the choice of $t_{\rm start}$ dramatically affects the quality and interpretation of ringdown fits

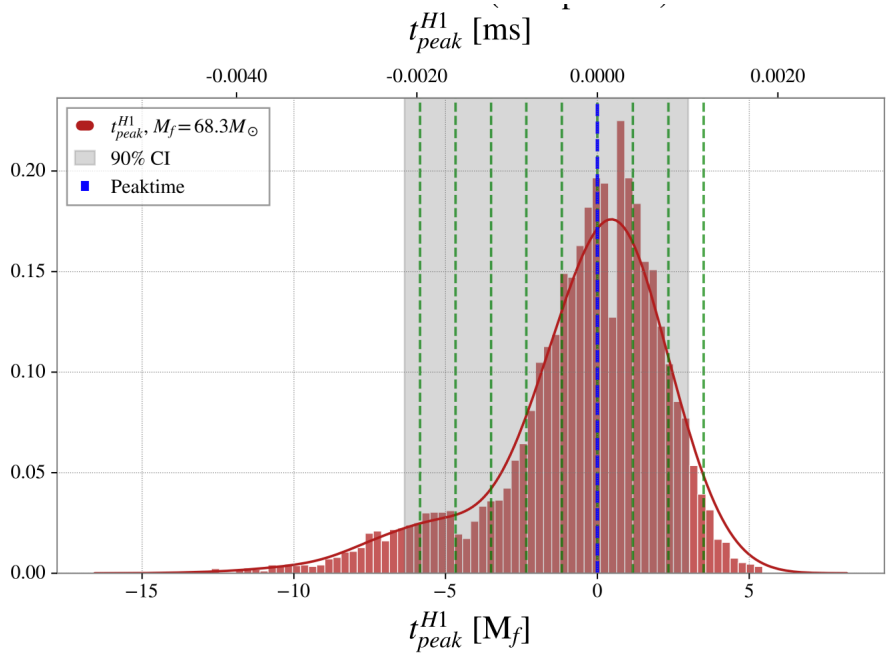

Figure 5.3: *Reference time distribution for* `KerrPostmerger` *analysis. The histogram (red bins) and KDE (solid line) show the distribution of t_0 values computed from 10^4 waveform samples using IMR posteriors. The distribution is shifted so that $t_0 = 0$ corresponds to the reference peak time (vertical dashed line). The gray shaded region indicates the 90% credible interval used for the start time grid. Green vertical dashed lines mark the 9-segment grid within this interval, with spacing optimized to exceed the ringdown sampling rate to ensure distinct analyses. Time is shown in both geometric units (bottom axis) and seconds (top axis) relative to the final mass M_f.*

across all waveform characteristics. At $t_{\rm start} = 0M$, both the waveform components and derived quantities (amplitude and frequency) show poor agreement with perturbation theory predictions, reflecting strong nonlinearities and rapidly evolving BH parameters. By $t_{\rm start} = 15M$, the fits improve substantially but systematic residuals remain visible, particularly in the frequency evolution. At $t_{\rm start} = 30M$, the Kerr model provides excellent agreement with numerical relativity across all four panels, demonstrating that the system has reached the perturbative regime, but this comes at the cost of substantial SNR loss from discarding the early post-merger signal. For typical SNRs in current observations, these residual systematics are smaller than statistical errors.

5.4.3 Assessing Mode Detectability

A primary objective of BH spectroscopy is the detection of multiple QNMs in the ringdown signal. A principled approach to this problem can be formulated within a Bayesian framework. Define the hypotheses H_n and H_m as the statements "n" or "m" detectable modes are present in the ringdown. The *odds ratio* between the two hypotheses is then

$$O_{n,m} \equiv \frac{p(H_n \,|\, d, I)}{p(H_m \,|\, d, I)} = \frac{p(H_n \,|\, I)\, p(d \,|\, H_n, I)}{p(H_m \,|\, I)\, p(d \,|\, H_m, I)} \equiv \frac{p(H_n \,|\, I)\, Z_n}{p(H_m \,|\, I)\, Z_m} \equiv \frac{p(H_n \,|\, I)}{p(H_m \,|\, I)}\, B_{n,m}, \quad (5.12)$$

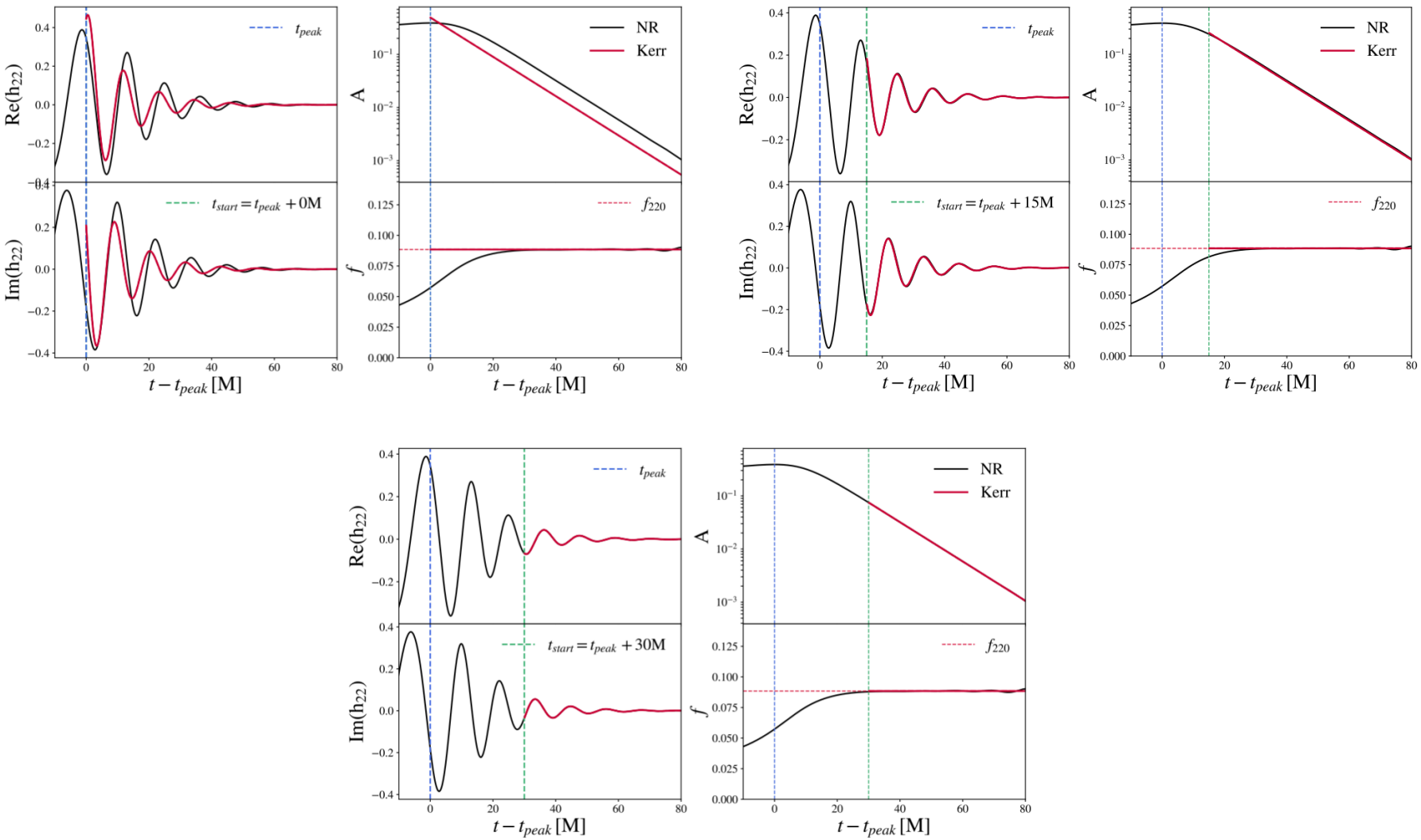

Figure 5.4: *Kerr model fits to the quadrupolar mode h_{22} from numerical relativity (SXS-0305) at different start times. Each of the three main panels contains four subplots:* ***left column*** *shows real (top) and imaginary (bottom) parts of h_{22};* ***right column*** *shows amplitude A (top) and instantaneous frequency f (bottom). All x-axes show time relative to peak amplitude in units of remnant mass $(t - t_{\rm peak})/M_f$.* ***Top left:*** *$t_{\rm start} = 0M$ shows poor agreement due to strong nonlinearities.* ***Top right:*** *$t_{\rm start} = 15M$ shows improved but imperfect fits with residual systematics.* ***Bottom center:*** *$t_{\rm start} = 30M$ provides excellent agreement but sacrifices significant SNR. Black solid lines: NR data; red solid lines: Kerr model fits; blue dashed lines: $t = 0M$ reference; green dashed lines: $t_{\rm start}$; red horizontal lines: perturbative prediction f_{220}.*

where Z_n and Z_m are the Bayesian evidences for the respective models, and $B_{n,m}$ is the Bayes factor (BF). If $\mathcal{O}_{n,m} > 1$, then H_n is more probable, and vice versa. For hypotheses with equal prior probability, $p(H_n|I) = p(H_m|I)$, the odds ratio reduces to the BF. Adding modes to a ringdown template increases the dimensionality of the parameter space. Even if the additional parameters improve the fit, the expanded prior volume naturally penalizes the evidence through the Occam factor [144]. Hence, unless an additional mode contributes substantially to the signal relative to the dominant $(l, m, n) = (2, 2, 0)$ mode, multi-mode templates are typically disfavored, especially at low SNR. One strategy to mitigate this effect is to adopt NR-informed parameterizations of mode amplitudes as functions of the progenitor parameters (see Section Section 5.3), allowing additional modes without increasing the effective dimensionality. This approach assumes the correctness of GR in the background information I [129, 132, 133], which enables "weaker" spectroscopic tests by permitting deviations in the spectrum, though these are less agnostic than models with free amplitudes. Using BFs to assess additional modes becomes nontrivial when dealing with nested models. For instance, a model with an additional mode reduces to a simpler model if the extra mode's amplitude is zero. In such cases, the BF strongly depends on the choice of priors, particularly for mode amplitudes, including regions not constrained by the likelihood [145, 146]. Consequently, support for a new mode can be arbitrarily diminished by enlarging the maximum allowed amplitude. The lack of physical guidance in setting priors exacerbates this issue. Owing to these subtleties, some studies avoid Bayes factors as detection statistics and instead rely on posterior-based criteria.For example, one may assess the significance of a nonzero amplitude using the ratio of the posterior mean (or median) to its standard deviation, or by computing the credible level of zero. The BF is related to the posterior support at zero, being the ratio of posterior to prior at that point[147]. Tracking the evolution of the amplitude posterior across different fitting times provides an additional safeguard against mismodeling: if the data are poorly described by any QNM model, a nonzero amplitude may appear at a given $t_{\rm start}$, but it will not evolve consistently with the expected QNM decay rate..

Noise Systematics

Detector noise can significantly impact evidence calculations and mode-detectability criteria, particularly for low-SNR ringdowns [148, 149]. Likelihood functions typically assume stationary, Gaussian noise, assumptions that are often violated in real data [150]. Additional modes can inadvertently fit nonstationarities, increasing false-detection probability. Incorporating multiple detectors helps mitigate this effect. The influence of noise can be assessed through injection studies: a simulated signal is added to (i) Gaussian noise and (ii) real noise surrounding the GW event. Repeating the second step at different times effectively samples the detector noise process, enabling quantification of its impact on detection metrics [129, 132]. These studies can be computationally expensive due to noise variability, signal-parameter uncertainties, and the

need to consider different QNM combinations and starting times.

5.5 Ringdown Observations and Multi-Mode Searches

5.5.1 The First Ringdown: GW150914

The ringdown of GW150914 provided the first definitive detection of a BH QNM. The high SNR of the event allowed for the isolation of the post-merger waveform and the extraction of the fundamental $(l, m, n) = (2, 2, 0)$ mode's characteristic frequency and damping time:

$$f_{220} \simeq 250 \text{ Hz}, \quad \tau_{220} \simeq 4 \text{ ms}. \tag{5.13}$$

The LIGO-Virgo-KAGRA (LVK) collaboration performed a single-QNM analysis starting at times $t_{\text{start}} \gtrsim 3 \text{ ms} \simeq 10M$ after the waveform peak. As shown in Fig. Figure 5.5, the measured frequency and damping time became consistent with the predictions of general relativity (GR) for sufficiently late start times, validating the QNM model. The robustness of this detection was later confirmed with more sophisticated time-domain methods. A decisive Bayes factor $B^{\text{signal}}_{\text{noise}} \simeq e^{14.6}$ favored a ringdown signal over pure noise, while no statistically significant evidence was found for the presence of additional modes (overtones or higher harmonics) in this event [122].

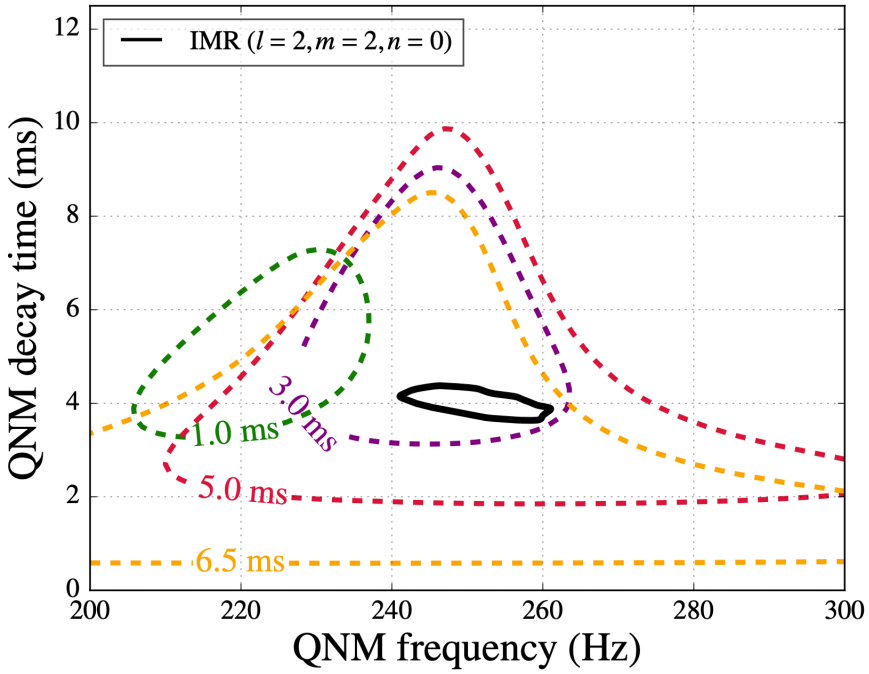

Figure 5.5: *Two-dimensional posterior distributions for the frequency and damping time of the fundamental* $(2, 2, 0)$ *QNM inferred from GW150914 data using single damped sinusoid fits at various analysis start times (dashed contours). The results demonstrate that for sufficiently late start times (approximately* $t_{peak} + 10M_f$*), the ringdown-only analysis converges to values consistent with the full inspiral-merger-ringdown (IMR) analysis (solid contour). This agreement validates the QNM model's applicability during the late-time ringdown phase. Adapted from* [122].

5.5.2 Population Studies in GWTC-3

The GWTC-3 catalog enabled the first population-wide studies of ringdown signals. Of the 90 compact binary coalescences, 48 met the criteria for testing GR, and 22 of those had sufficient ringdown SNR for detailed spectroscopic analysis. The primary analysis frameworks is the time-domain `pyRing` pipeline. The `pyRing` pipeline, which uses the truncated time-domain likelihood described in Section Section 5.2.2, typically follows a hierarchical strategy: starting with agnostic Damped Sinusoids (DS), then Kerr templates, and finally NR-informed models. Analyses are performed over a grid of start times to verify that parameter estimates stabilize and become consistent with GR predictions at late times. For the fundamental $(2, 2, 0)$ mode, the results across the 22 events are consistent with the predictions of BH perturbation theory. The inclusion of the first overtone in Kerr templates often improves the recovered SNR by capturing more of the early post-merger signal.

5.5.3 The Search for Higher-Order Modes

A key goal of BH spectroscopy is the detection of multiple, distinct QNMs. The LVK collaboration has performed extensive searches for higher-order modes—such as the $(3, 3, 0)$, $(3, 2, 0)$, and $(2, 1, 0)$ harmonics—using the `pyRing` pipeline. These searches involve rigorous model selection between templates of increasing complexity. To avoid spurious detections, physical constraints (like equatorial reflection symmetry) and empirical bounds on amplitude ratios (e.g., $A_{l,m,n}/A_{2,2,0} < 0.9$) are typically imposed. Despite these efforts, no statistically significant evidence for higher-order modes was found in the GWTC-3 population. An apparent higher-mode detection in GW191109_010717 was later attributed to noise non-stationarity. A few events, like GW200224_222234, showed weak, marginal hints of secondary modes, but the evidence was highly sensitive to the analysis start time and prior choices.

The Case of GW190521

GW190521, a massive, short-duration merger, has been a prime candidate for higher-mode searches due to its potentially asymmetric mass ratio. Some studies using agnostic Damped Sinusoids models reported features compatible with the $(3, 3, 0)$ mode. However, the Bayesian evidence for this additional mode was highly sensitive to the waveform model, amplitude priors, and start time. When physical constraints on amplitudes and symmetries were enforced, the preference for additional modes typically vanished. This highlights the challenge of distinguishing faint physical signals from systematic modeling effects.

5.5.4 Summary of Challenges

The robust detection of higher-order modes in the current LVK catalog remains elusive due to several interconnected challenges:

- **Low SNR:** For most events, the ringdown SNR is too low for a conclusive multi-mode detection.
- **Systematic Sensitivities:** Results are highly sensitive to the analysis start time t_0, prior choices for mode amplitudes, and the specific ringdown model used.
- **Short Ringdowns:** Massive mergers like GW190521 have ringdowns with few observable cycles.
- **Model Limitations:** Current QNM models struggle to accurately capture the early, non-linear post-merger dynamics.

In summary, while the fundamental $(2, 2, 0)$ mode has been consistently observed and is in agreement with GR, the detection of a clear, unambiguous higher harmonic requires louder signals and more robust analysis techniques. The following sections present new results from the O4 observing run, where several promising candidates have emerged.

5.6 Post-Merger Analysis of O4a Data with pyRing

This section presents the results of a systematic ringdown analysis for selected events from the O4a observing run, conducted within the pyRing framework. The analysis employs the time-domain likelihood and hierarchical template methodology detailed in previous sections to characterize remnant BHs and test the predictions of GR.

5.6.1 Event Selection and Configuration

We focus on events with confident ringdown signatures identified in the O4a data. Candidate selection follows the criterion $\log_{10}\mathcal{B} \gtrsim 1$ for `KerrPostmerger` templates, where $\mathcal{B}$ denotes the signal-versus-noise Bayes factor. This threshold ensures that the included events exhibit distinguishable ringdown signals while maintaining computational feasibility. We employ the hierarchical analysis strategy outlined in Section Section 5.3, progressing from the agnostic `Damped Sinusoids` model to the GR-constrained `Kerr` template, and finally to the NR-calibrated `KerrPostmerger` model. Analysis start times follow the procedures established in Section 5.4.2, with results reported at characteristic validity times $t_{\rm nom} = 10M$ for `DS` and `Kerr` templates, and $t_{\rm nom} = 0M$ for `KerrPostmerger`, consistent with its phenomenological nature and NR calibration. The selected events are analyzed with each of the three template families at their nominal start times, as summarized in Table Table 5.1.

5.6.2 Consistency of Remnant Properties

A primary outcome of this analysis is the robust agreement between remnant properties inferred from ringdown-only signals and those derived from full inspiral-merger-ringdown (IMR) studies. As summarized in Fig. Figure 5.6 and Table Table 5.1, the posterior distributions for the final mass M_f and dimensionless spin χ_f obtained using the `Damped Sinusoids`, `Kerr`, and `KerrPostmerger` templates all show significant

Event	Redshifted Final Mass $(1+z)M_{\rm f}/M_\odot$			Final Spin $\chi_{\rm f}$			$\log_{10}\mathcal{B}^{\rm HM}_{220}$	
	IMR	`Kerr`	`KerrPostmerger`	IMR	`Kerr`	`KerrPostmerger`	`Kerr`	`KerrPostmerger`
GW230601_224134	$GW230601_224134$	$199.78^{+227.95}_{-143.55}$	$179.09^{+13.15}_{-24.23}$	$GW230601_224134$	$0.83^{+0.15}_{-0.72}$	$0.86^{+0.07}_{-0.14}$	−0.73	−0.06
GW230609_064958	$GW230609_064958$	$81.75^{+388.32}_{-69.54}$	$93.53^{+12.25}_{-14.09}$	$GW230609_064958$	$0.41^{+0.46}_{-0.36}$	$0.81^{+0.10}_{-0.15}$	−0.68	0.11
GW230628_231200	$GW230628_231200$	$88.23^{+20.56}_{-24.90}$	$87.17^{+6.98}_{-9.20}$	$GW230628_231200$	$0.80^{+0.14}_{-0.48}$	$0.86^{+0.06}_{-0.11}$	−0.42	0.20
GW230811_032116	$GW230811_032116$	$74.31^{+123.08}_{-38.08}$	$74.54^{+11.12}_{-11.36}$	$GW230811_032116$	$0.56^{+0.38}_{-0.49}$	$0.80^{+0.10}_{-0.13}$	−1.22	0.12
GW230814_061920	$GW230814_061920$	$177.40^{+64.38}_{-41.70}$	$192.39^{+17.10}_{-21.33}$	$GW230814_061920$	$0.61^{+0.30}_{-0.52}$	$0.82^{+0.08}_{-0.12}$	−1.29	0.46
GW230824_033047	$GW230824_033047$	$166.38^{+51.07}_{-50.34}$	$160.22^{+13.74}_{-20.36}$	$GW230824_033047$	$0.78^{+0.17}_{-0.60}$	$0.83^{+0.08}_{-0.13}$	−0.98	−0.04
GW230914_111401	$GW230914_111401$	$143.88^{+34.50}_{-33.95}$	$144.91^{+11.39}_{-13.43}$	$GW230914_111401$	$0.66^{+0.22}_{-0.52}$	$0.81^{+0.09}_{-0.11}$	−1.15	0.23
GW230919_215712	$GW230919_215712$	$75.51^{+198.89}_{-25.25}$	$60.39^{+168.56}_{-9.99}$	$GW230919_215712$	$0.57^{+0.36}_{-0.50}$	$0.82^{+0.10}_{-0.18}$	−0.94	−0.14
GW230922_020344	$GW230922_020344$	$75.16^{+25.67}_{-14.44}$	$85.78^{+8.90}_{-10.58}$	$GW230922_020344$	$0.37^{+0.41}_{-0.33}$	$0.81^{+0.09}_{-0.13}$	−0.91	0.17
GW230922_040658	$GW230922_040658$	$227.50^{+65.04}_{-49.13}$	$238.63^{+16.73}_{-21.74}$	$GW230922_040658$	$0.62^{+0.28}_{-0.51}$	$0.81^{+0.09}_{-0.12}$	−0.96	0.17
GW230924_124453	$GW230924_124453$	$79.36^{+27.55}_{-25.20}$	$72.52^{+8.14}_{-10.14}$	$GW230924_124453$	$0.76^{+0.19}_{-0.60}$	$0.82^{+0.09}_{-0.13}$	−1.35	0.00
GW230927_043729	$GW230927_043729$	$218.76^{+192.81}_{-147.79}$	$91.29^{+11.74}_{-13.96}$	$GW230927_043729$	$0.43^{+0.45}_{-0.39}$	$0.81^{+0.10}_{-0.14}$	−0.74	−0.02
GW230927_153832	$GW230927_153832$	$44.28^{+14.39}_{-10.99}$	$47.87^{+3.80}_{-5.61}$	$GW230927_153832$	$0.65^{+0.27}_{-0.54}$	$0.83^{+0.08}_{-0.12}$	−0.77	0.14
GW230928_215827	$GW230928_215827$	$154.28^{+263.10}_{-127.54}$	$133.09^{+16.22}_{-21.20}$	$GW230928_215827$	$0.64^{+0.33}_{-0.56}$	$0.83^{+0.09}_{-0.15}$	−0.91	0.06
GW231001_140220	$GW231001_140220$	$171.55^{+41.71}_{-24.13}$	$214.22^{+16.27}_{-20.15}$	$GW231001_140220$	$0.24^{+0.41}_{-0.22}$	$0.80^{+0.10}_{-0.14}$	−0.49	0.55
GW231028_153006	$GW231028_153006$	$250.83^{+25.62}_{-31.71}$	$226.83^{+10.46}_{-11.22}$	$GW231028_153006$	$0.81^{+0.08}_{-0.17}$	$0.80^{+0.08}_{-0.07}$	0.01	−0.07
GW231102_071736	$GW231102_071736$	$152.05^{+48.80}_{-43.06}$	$164.83^{+12.41}_{-15.56}$	$GW231102_071736$	$0.76^{+0.16}_{-0.49}$	$0.80^{+0.09}_{-0.11}$	−0.70	−0.01
GW231108_125142	$GW231108_125142$	$45.43^{+98.36}_{-11.50}$	$50.25^{+5.76}_{-6.89}$	$GW231108_125142$	$0.40^{+0.45}_{-0.36}$	$0.83^{+0.09}_{-0.13}$	−0.82	−0.02
GW231206_233134	$GW231206_233134$	$126.59^{+26.29}_{-35.03}$	$99.05^{+8.92}_{-11.15}$	$GW231206_233134$	$0.90^{+0.07}_{-0.32}$	$0.83^{+0.08}_{-0.12}$	−1.17	0.10
GW231206_233901	$GW231206_233901$	$86.11^{+27.85}_{-19.58}$	$80.65^{+7.18}_{-8.60}$	$GW231206_233901$	$0.59^{+0.29}_{-0.49}$	$0.77^{+0.11}_{-0.14}$	−1.00	0.04
GW231213_111417	$GW231213_111417$	$86.60^{+33.75}_{-22.82}$	$104.53^{+11.06}_{-12.88}$	$GW231213_111417$	$0.55^{+0.33}_{-0.48}$	$0.81^{+0.09}_{-0.14}$	−1.23	0.01
GW231223_032836	$GW231223_032836$	$118.03^{+78.97}_{-72.05}$	$127.57^{+18.55}_{-20.54}$	$GW231223_032836$	$0.47^{+0.44}_{-0.42}$	$0.80^{+0.10}_{-0.15}$	−0.91	0.01
GW231226_101520	$GW231226_101520$	$96.91^{+16.75}_{-19.89}$	$86.20^{+5.30}_{-6.08}$	$GW231226_101520$	$0.72^{+0.16}_{-0.39}$	$0.75^{+0.12}_{-0.12}$	−1.15	0.02

Table 5.1: *The median and symmetric 90% credible intervals of the redshifted final mass and final spin, inferred from the full IMR analysis [151] and the* `pyRing` *analysis with two waveform models (*`Kerr` *and* `KerrPostmerger`*) at their nominal validity time $t_{\rm nom}$. A value of $\log_{10}\mathcal{B}^{\rm HM}_{220} > 1$ indicates support for higher modes (HMs) in the data.*

overlap with the results from full IMR analyses. This consistency, observed across multiple independent waveform models, reinforces the validity of the ringdown phase for remnant characterization. The evolution of the Bayes factor with analysis start time is summarized in Fig. 5.7, illustrating how evidence for higher modes varies across the posterior support of $t_{\rm start}$ for different template families.

5.6.3 Tests of GR via the Ringdown Spectrum

We performed a parametric test of GR by introducing fractional deviations to the fundamental $(2, 2, 0)$ QNM: $\delta\hat{f}_{220}$ (constrained to $[-1, 1]$) and $\delta\hat{\tau}_{220}$ (constrained to $[-0.9, 1]$) [129]. Using uniform priors for these deviation parameters, we conducted the analysis with the `KerrPostmerger` model including all higher modes to mitigate false deviations from unmodeled mode content. We hierarchically combined deviation measurements from all analyzed O4a events (Table Table 5.1), adopting a multivariate Gaussian distribution for the population [152]. Note that while pre-O4 events were analyzed with `KerrPostmerger` in [133], those results employed a peak-time approximation that can induce non-negligible shifts; a reanalysis will be incorporated in future work. The hierarchical constraints yield:

$$\delta\hat{f}_{220} = 0.11^{+0.22}_{-0.18}; \quad \delta\hat{\tau}_{220} = 0.18^{+0.26}_{-0.26} \tag{5.14}$$

The inferred deviations are centered close to zero, consistent with GR expectations within statistical uncertainties. To capture potential event-to-event variation, we further model the population distribution with hyperparameters:

$$\begin{aligned} \mu_{\delta\hat{f}_{220}} &= 0.11^{+0.22}_{-0.18}; \quad \sigma_{\delta\hat{f}_{220}} < 80.4 \\ \mu_{\delta\hat{\tau}_{220}} &= 0.18^{+0.26}_{-0.26}; \quad \sigma_{\delta\hat{\tau}_{220}} < 97.4 \\ \rho_{\delta\hat{f}_{220}\delta\hat{\tau}_{220}} &= 0.18^{+0.26}_{-0.26} \end{aligned} \tag{5.15}$$

As shown in Figure Figure 5.8, both deviation parameters are consistent with zero—the value predicted by GR—within their 90% credible intervals, though the distributions show slight positive tendencies. We quantified consistency with GR using the $Q^{\rm 4D}_{\rm GR}$ quantile [153], estimating uncertainties via bootstrapping with 1000 synthetic catalogs [154]. Applying a stricter selection criterion ($\log_{10}\mathcal{B} > 8$) increases agreement with GR but introduces higher variance due to the reduced event set. The results are consistent with GR, though the combined posterior shows that the GR value (0,0) lies near the edge of the 90% credible region, indicating that future data with higher sensitivity may provide more stringent constraints.

5.7 Special Events

This section presents detailed ringdown analyses of three significant events from the O4 observing run. These case studies demonstrate the application of BH spectroscopy,

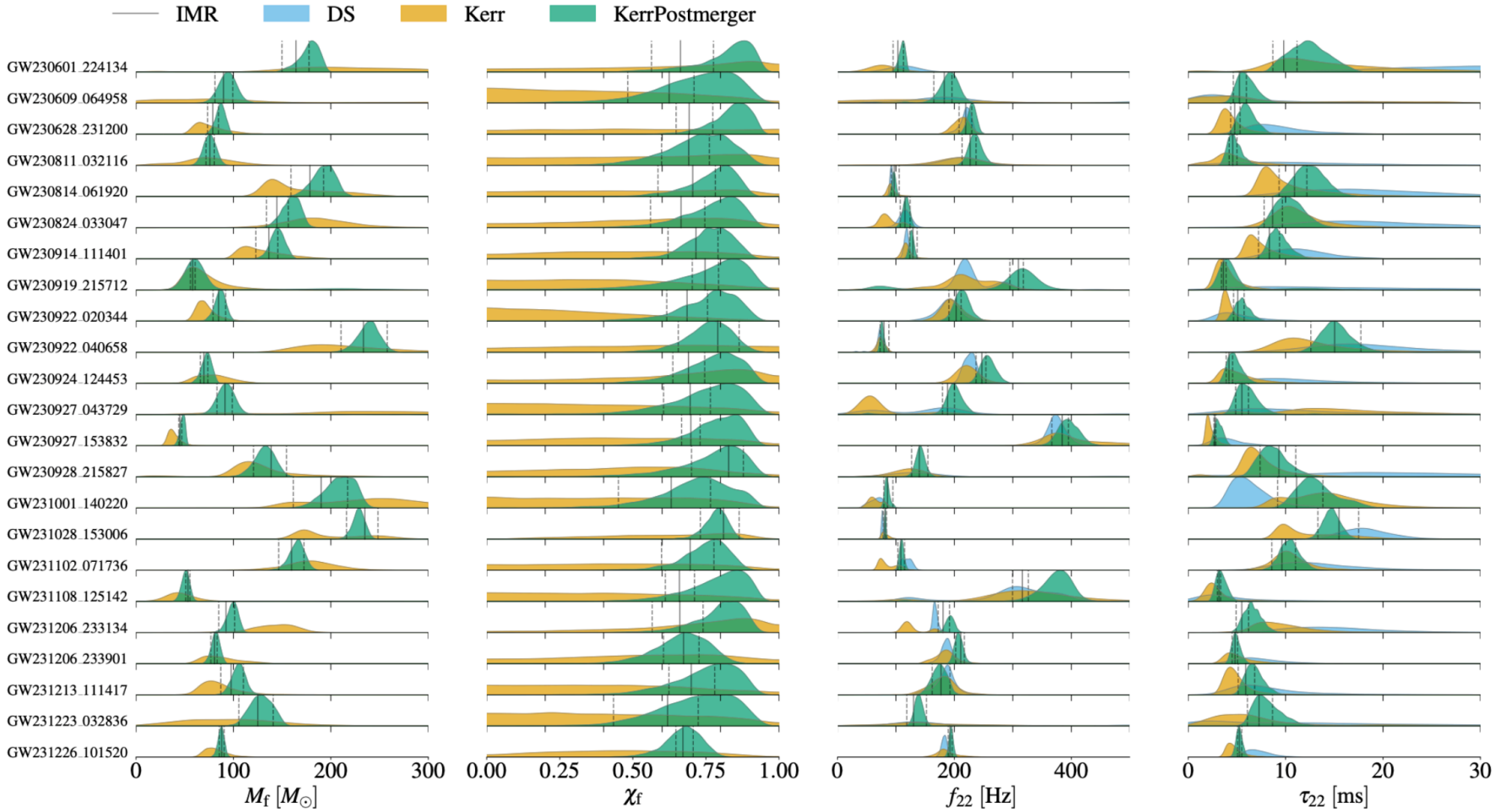

Figure 5.6: *Comparison of final mass, final spin, fundamental mode ringdown frequency and damping time at their nominal validity time $t_{\rm nom}$ for all events analyzed by* `pyRing`*. Different posterior colors represent the templates used in the analysis:* `DS` *with a single mode (blue), precessing* `Kerr` *with the highest evidence mode combination (yellow), and* `KerrPostmerger` *(green) using all available higher modes. The* `DS` *analysis provides results for f_{220} and τ_{220}. IMR parameter estimation median values (solid vertical black lines) with 90% credible intervals (dashed vertical black lines) from [151] are shown alongside the corresponding ringdown estimates, assessing consistency with GR expectations.*

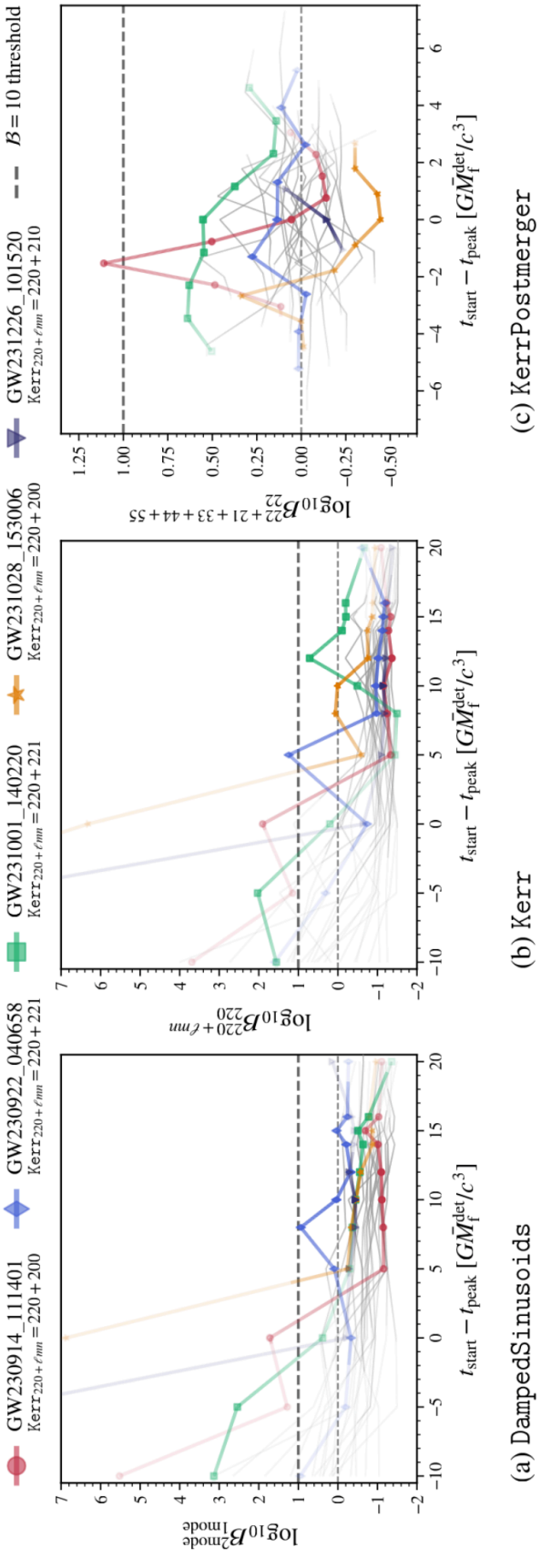

(a) DampedSinusoids (b) Kerr (c) KerrPostmerger

Figure 5.7: *Logarithmic Bayes factor vs. start times of the analysis, used to evaluate the evidence for higher modes (HMs) across different template families. The dashed horizontal lines mark the $\mathcal{B} = 1$ border and the $\mathcal{B} = 10$ detection threshold. The colored shading represents the t_{start} posterior, while regions outside the 90% credible interval have a constant faint shading. We highlight five events in color, while the bulk of events is depicted in gray. The second line of each legend reports the most favored HM combination for which the* `Kerr` *Bayes factor is computed. The* `KerrPostmerger` *analysis always includes the modes given in the vertical axis label. No statistically significant presence of multiple modes was found for all times in the t_{start} posterior.*

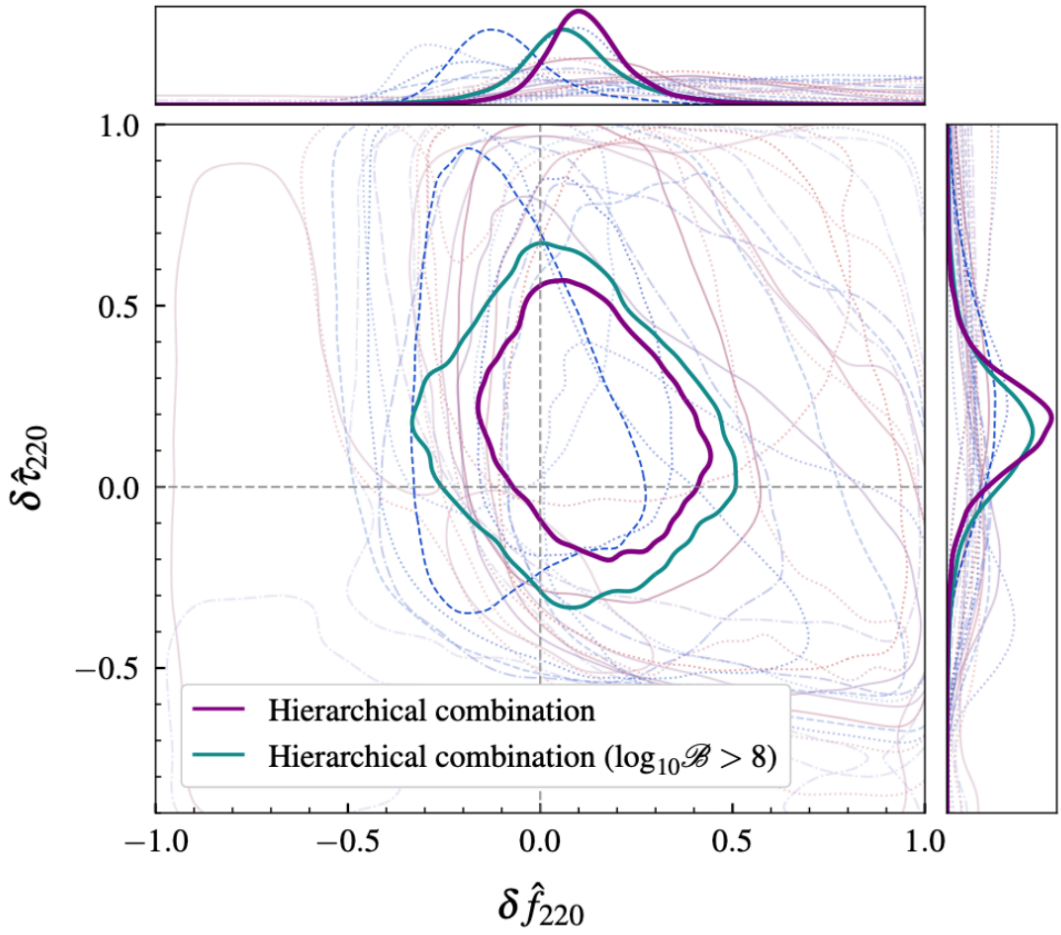

Figure 5.8: 90% *contours for the posterior probability distribution of frequency deviation* $\delta\hat{f}_{220}$ *and damping time* $\delta\hat{\tau}_{220}$ *for the analysis with a* `KerrPostmerger` *template including all HMs and fractional deviations on the* $(2,2,0)$ *mode (light curves), along with the hierarchically combined results (heavy curves), including with the* $\log_{10}\mathcal{B} > 8$ *constraint. The events plotted and hierarchical distribution are the O4a events listed in Table Table 5.1.*

detailed in Section 5.1, to test fundamental theoretical pillars established in Section 1.3—specifically the Kerr metric (Section 1.3.1), the no-hair theorem, and the laws of BH thermodynamics (Section 1.3.3).

5.7.1 GW230814: A High-SNR Laboratory for Ringdown Systematics

Detected by LIGO Livingston with a remarkable SNR of 42.4, GW230814 was the loudest signal in the GWTC-4.0 catalog. This BBH merger, with component masses $m_1 = 33.7^{+2.9}_{-2.2} M_\odot$, $m_2 = 28.2^{+2.2}_{-3.1} M_\odot$, and low effective inspiral spin $\chi_{\rm eff} = -0.01^{+0.06}_{-0.07}$, provided an excellent dataset to probe the ringdown phase with high precision.

Anomalous Features and Systematic Investigations

The `pyRing` analysis revealed an unusual bimodal structure in the posterior distributions for the fundamental $(2,2,0)$ QNM parameters. As shown in Fig. Figure 5.14, fits

starting at late times (~ 41 ms post-peak), where the exponential ringdown model is most reliable, yielded two distinct solutions:

- A primary component at $f \sim 68$ Hz, consistent with the fundamental QNM frequency predicted by the remnant's mass and spin.
- A secondary component at $f \sim 45$ Hz, with a larger amplitude, potentially corresponding to an unexpectedly excited higher angular mode.

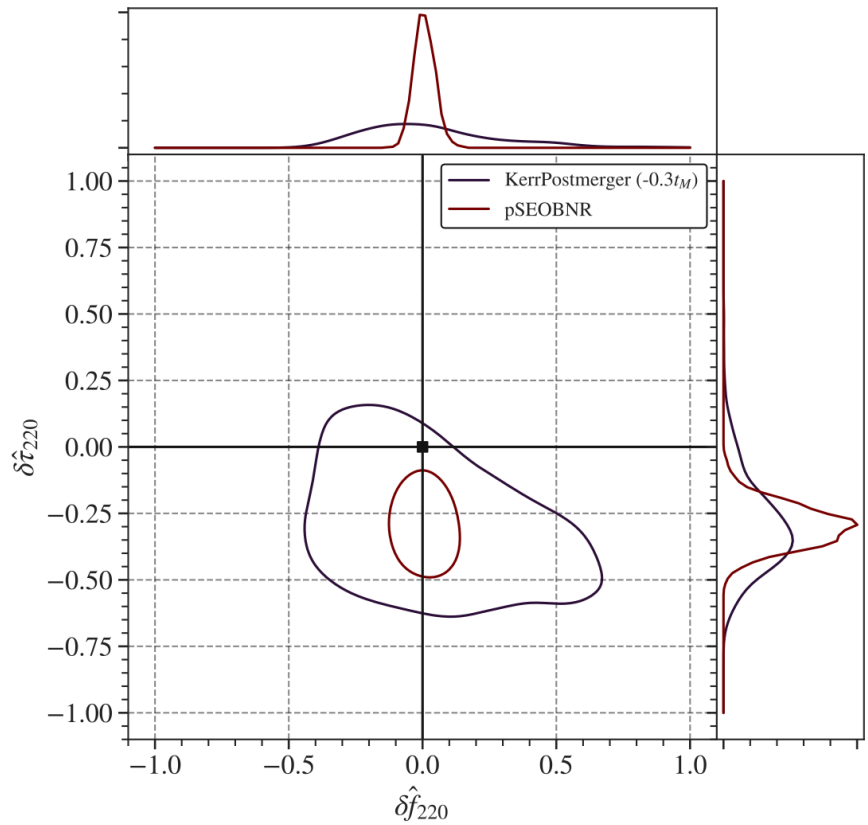

Figure 5.9: *Fractional deviations* $(\delta\hat{f}_{220}, \delta\hat{\tau}_{220})$ *from the GR-predicted QNM parameters for GW230814. Contours show 90% credible regions from the pSEOBNR* (*dashed-dotted maroon*) *and* `pyRing` *KerrPostmerger* (*solid black*) *analyses. The black square marks the GR prediction.*

This bimodality propagated to the inferred remnant properties, creating tension with the full IMR results. To determine the origin of these features, we performed extensive injections of GR signals into real detector noise. These studies revealed that similar anomalous deviations occur in $\sim 32\%$ of cases for the damping time and $\sim 20\%$ for the frequency, indicating they are consistent with statistical fluctuations and noise artifacts rather than a violation of the Kerr hypothesis.

5.7.2 GW231123: Confirming an Intermediate-Mass Black Hole

GW231123, observed with a network SNR of ~ 22.5, is a compelling candidate for the most massive BBH merger detected to date. The system comprised two highly spinning

BHs ($\chi_1 = 0.90^{+0.10}_{-0.19}$, $\chi_2 = 0.80^{+0.20}_{-0.51}$) with masses $137^{+22}_{-17} M_\odot$ and $103^{+20}_{-52} M_\odot$, resulting in a total mass of 189–$266 M_\odot$ that significantly exceeds that of GW190521.

Ringdown of a Massive Remnant

The signal's morphology was dominated by the merger-ringdown, with only ~ 5 inspiral cycles in the sensitive band. The ringdown itself began unusually late, ~ 19 ms after the polarization peak, a characteristic of extremely massive systems. The ringdown

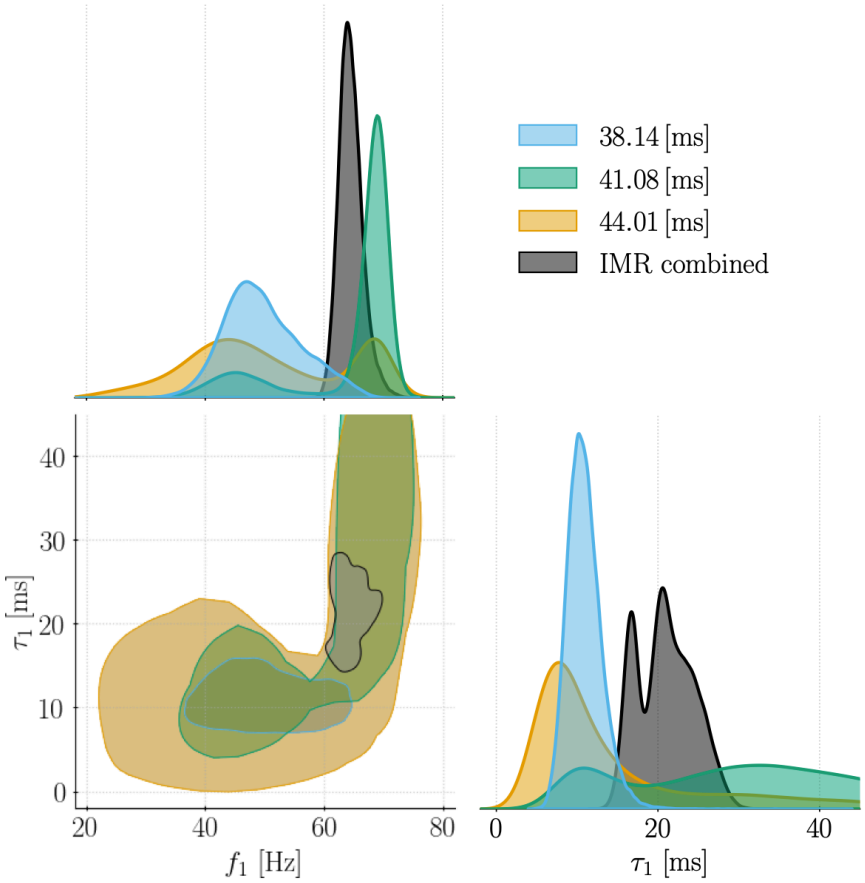

Figure 5.10: *Posterior distribution for the frequency and damping time of the fundamental mode in GW231123 from a single damped sinusoid fit (90% credible region), compared to the IMR prediction. The damping time axis is truncated for clarity.*

analysis, summarized in Fig. Figure 5.10, also indicated a bimodal structure. Crucially, unlike GW230814, both posterior components robustly inferred a final mass $\geq 200 M_\odot$ across all analysis start times. This provides strong, model-agnostic evidence for the formation of an intermediate-mass BH, consistent with the Kerr paradigm.

5.7.3 GW250114: A Landmark for BH Spectroscopy and Thermodynamics

GW250114 marks a watershed moment in GW astronomy. Detected with an unprecedented network SNR of ~ 80, this nearly equal-mass ($m_1 = 33.6 M_\odot$, $m_2 = 32.2 M_\odot$), low-spin ($\chi < 0.26$) binary provided the data quality necessary for transformative

tests of fundamental physics.

The First Confident Multi-Mode Detection

Applying the agnostic `Damped Sinusoids` model (Section 5.3), we achieved the first unambiguous detection of two QNMs. Figure Figure 5.11 illustrates the evolution of the mode amplitudes with start time:

- The **fundamental** $(2, 2, 0)$ **mode** was confidently detected $(> 7\sigma)$ for start times up to $20M$ post-peak.
- The **first overtone** $(2, 2, 1)$ was significant at $> 4\sigma$ for start times between $6M$ and $9M$, contributing for approximately one cycle before decaying away.

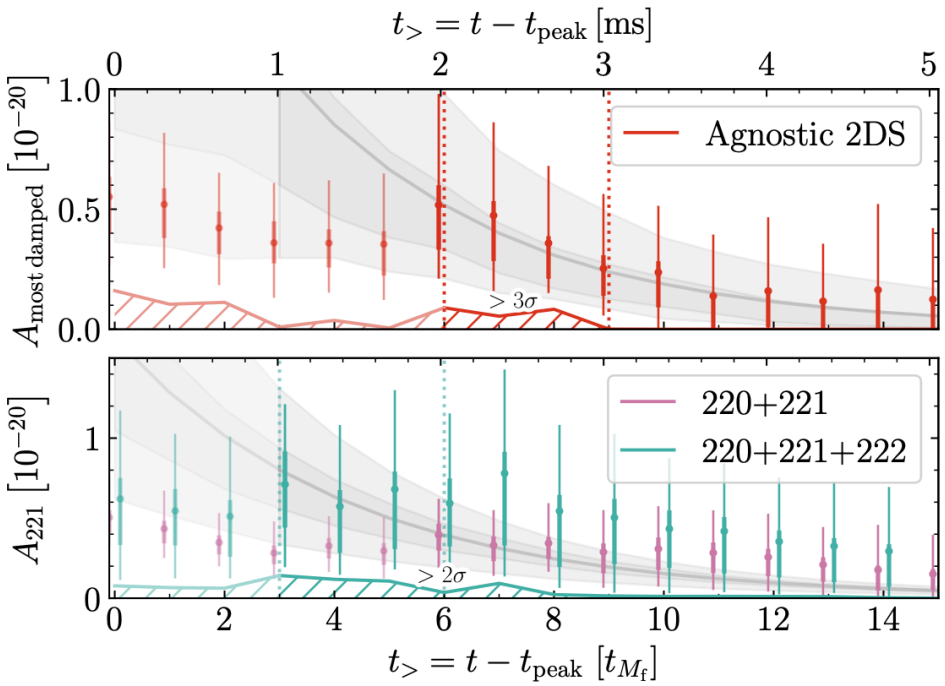

Figure 5.11: *Recovered strain amplitudes for the fundamental mode (top) and first overtone (bottom) in GW250114 as a function of analysis start time. Error bars show 90% (thin) and 50% (thick) credible intervals. The overtone is significantly detected for start times between $6M$ and $9M$.*

Precision Test of the Kerr Metric and No-Hair Theorem

The detection of two modes enabled a direct test of the Kerr spectrum, a key prediction of the no-hair theorem (Section 1.3). As shown in Figure 5.12, the measured frequencies of the fundamental mode and overtone were consistent with the unique spectrum of a Kerr BH (Section 1.3.1). We constrained deviations of the overtone frequency from the GR prediction to $\delta f_{221} \approx 0.1$, verifying the Kerr metric to within $\sim 30\%$ precision—the most stringent multi-mode constraint to date.

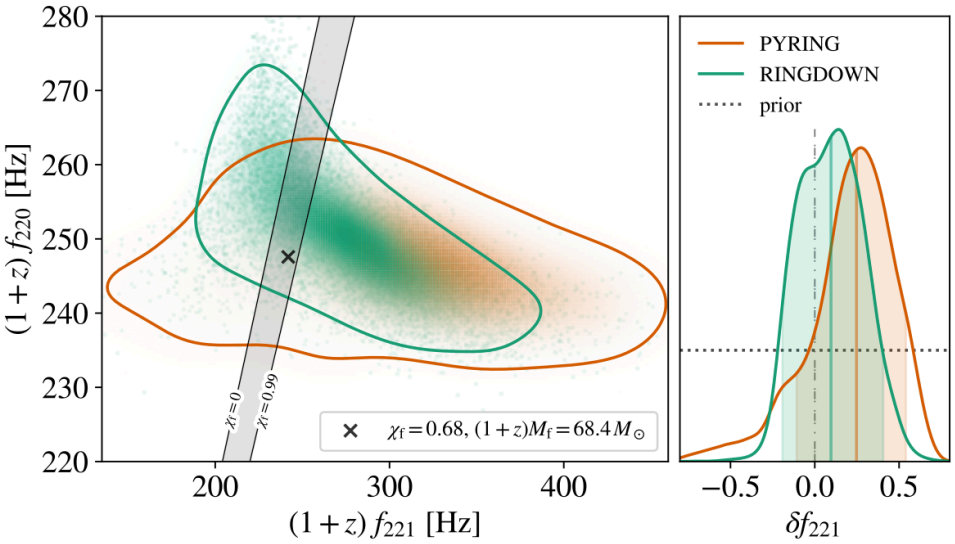

Figure 5.12: ***Left:*** *Measured QNM frequencies (90% credible regions) for GW250114 compared to the Kerr spectrum (black band).* ***Right:*** *Posterior for the fractional deviation of the overtone frequency from its Kerr prediction. The results are consistent with GR.*

The Most Stringent Test of the Area Law

Leveraging the signal's strength, we performed the most robust test yet of Hawking's area law (Section 1.3.3), which states that the total event horizon area cannot decrease. By independently estimating the initial and final BH areas from different segments of the signal, we confirmed an increase in total horizon area with 4.8σ credibility (Figure 5.13). This result provides the strongest experimental support for this cornerstone of BH thermodynamics, demonstrating that GW observations can directly probe thermodynamic laws in the most extreme curvature regime.

5.8 Conclusion

This chapter has demonstrated the maturation of BH spectroscopy through systematic, event-by-event ringdown analysis using the `pyRing` pipeline. Our time-domain Bayesian framework has enabled robust tests of GR across multiple significant detections from the O4 observing run.

The three special events analyzed here showcase the diverse science accessible through ringdown studies: GW230814 provided a high-SNR laboratory for understanding systematic uncertainties, GW231123 confirmed the formation of an intermediate-mass BH through consistent remnant mass estimates, and GW250114 delivered the first confident multi-mode detection enabling precision tests of the Kerr metric and Hawking's area law.

Collectively, these analyses find no evidence for deviations from GR in the ringdown phase. The consistency between ringdown-only and full IMR parameter estimates across all events reinforces the validity of the Kerr BH paradigm. The detection of

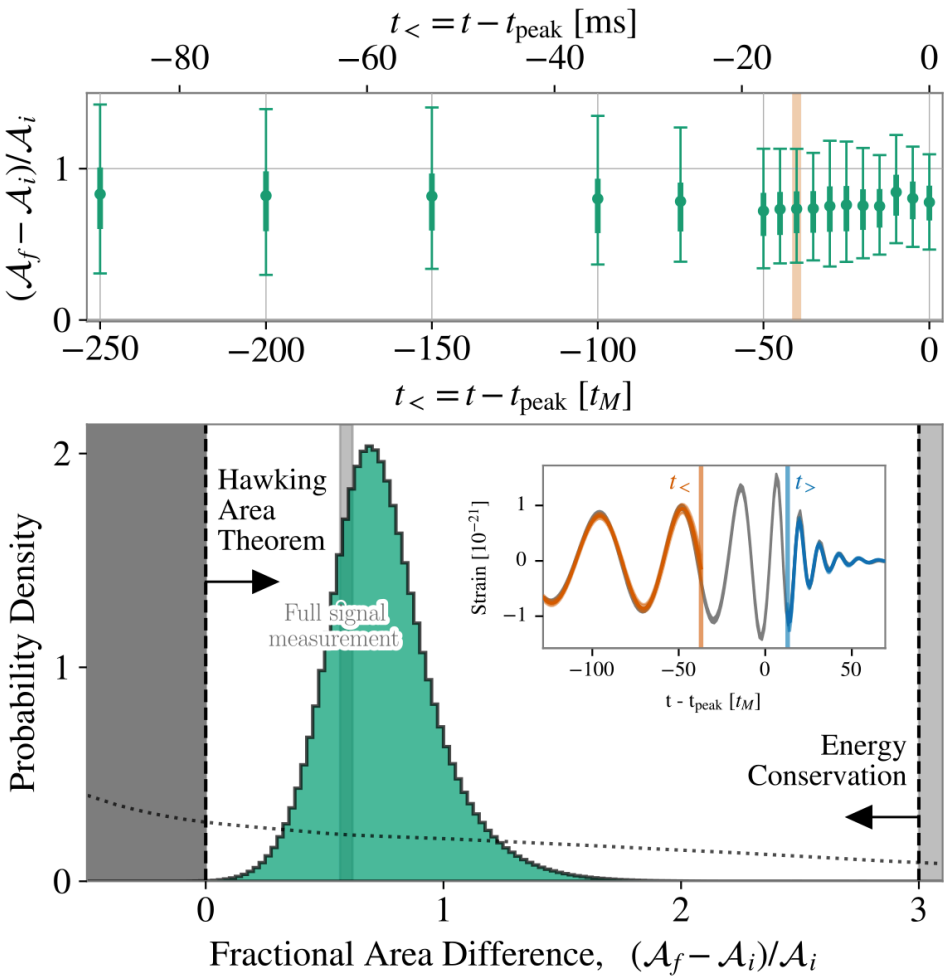

Figure 5.13: *Test of Hawking's area law with GW250114.* ***Top:*** *Fractional area increase for different pre-merger data truncations.* ***Bottom:*** *Posterior distribution for the area difference, showing a* 4.8σ *confirmation of the area increase law.*

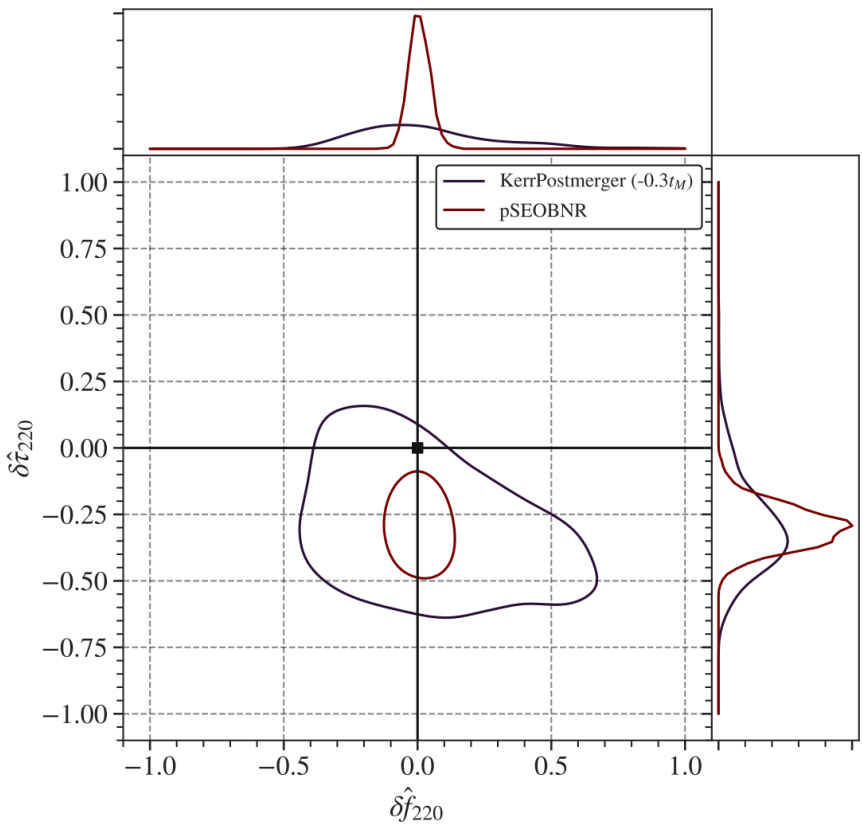

Figure 5.14: *The 90% credible regions for the posterior probability distribution of the fractional deviations in the frequency and damping time of the* $(2,2,0)$ *QNM,* $(\delta\hat{f}_{220}, \delta\hat{\tau}_{220})$ *for GW230814. The contours and corresponding marginalized posteriors are shown for the pSEOBNR (dashed–dotted maroon, see Section 3.3) and* `pyRing` *KerrPostmerger (solid black, see Section 3.4) analyses. The black square denotes the GR prediction* $\delta\hat{f}_{220} = \delta\hat{\tau}_{220} = 0$.

multiple QNMs in GW250114, combined with the 4.8σ confirmation of the area law, represents a fundamental advance—demonstrating that GW observations can now perform direct tests of fundamental BH properties.

As detector sensitivity continues to improve, the event-by-event approach established here will naturally evolve into population-level studies. The methodological foundation laid in this chapter positions us to transform future high-SNR detections into a precision spectroscopic survey of BHs in the strong-gravity regime.

6

Testing modified gravity with dark sirens

6.1 Modified GW Propagation

GWs provide a unique opportunity to test GR on cosmological scales, complementing traditional electromagnetic probes. While electromagnetic observations primarily constrain the background expansion history (the evolution of the scale factor $a(t)$ and Hubble parameter $H(z)$), GWs are sensitive both to the expansion and to the propagation of tensor perturbations through the large-scale structure of spacetime. This dual sensitivity makes them particularly powerful for testing modified gravity theories that predict deviations in the dynamics of GW propagation.
In many modified gravity theories, the GW propagation equation acquires additional friction-like terms that affect amplitude attenuation over cosmological distances. These effects appear observationally as a discrepancy between the GW luminosity distance, $d_L^{\rm GW}$ inferred from the waveform amplitude, and the electromagnetic luminosity distance $d_L^{\rm EM}$ derived from traditional probes. A statistically significant deviation between the two would constitute direct evidence for departures from GR. To quantify such deviations, we first review the standard GR prediction.

6.1.1 GR Framework

In GR, tensor perturbations on a Friedmann–Lemaître–Robertson–Walker (FLRW) background obey the propagation equation in Fourier space:

$$\tilde{h}'' + 2H\tilde{h}' + k^2\tilde{h} = 0, \tag{6.1}$$

where primes denote derivatives with respect to conformal time η, k is the comoving wavenumber, and $\tilde{h}$ represents the Fourier amplitude of the tensor perturbation.
This equation implies that the luminosity distance inferred from GW and electromag-

netic observations are identical:

$$d_L^{\mathrm{GW}}(z) = d_L^{\mathrm{EM}}(z). \tag{6.2}$$

This equivalence is a direct prediction of GR and provides a null test for possible deviations arising in modified gravity theories.

6.1.2 Modified Propagation Equations

Many extensions of GR predict modifications to Equation 6.2. These modifications typically introduce additional friction terms that alter the amplitude damping of GWs as they propagate across cosmological distances. The modified friction term changes the observed amplitude of GWs, producing a redshift-dependent deviation between the GW and electromagnetic luminosity distances. Below, we discuss three classes of models that capture distinct physical mechanisms responsible for such deviations.

Running Planck Mass Models

In several extensions of GR, particularly scalar–tensor and $f(R)$ theories, an additional friction term arises from a time-dependent, or 'running,' Planck mass $M_*(a)$ [155, 156, 157, 158, 159]. The quantity $M_*(a)$ determines the effective gravitational coupling

$$G_{\mathrm{eff}} = \frac{1}{8\pi M_*^2(a)},$$

so that variations in M_* directly modify the propagation of tensor perturbations.
In conformal time, the equation governing the propagation of GWs becomes

$$\tilde{h}'' + 2H\big[1 - \delta(\eta)\big]\,\tilde{h}' + k^2\tilde{h} = 0, \tag{6.3}$$

where primes denote derivatives with respect to conformal time. The function $\delta(\eta)$ quantifies deviations from GR through the logarithmic derivative of the effective Planck mass,

$$\delta(\eta) = \frac{1}{2}\frac{d\ln M_*^2}{d\ln a}. \tag{6.4}$$

In the GR limit, M_* is constant, $\delta = 0$, and the standard propagation equation is recovered.
The modified friction term alters the amplitude of GWs as they travel through the expanding Universe. This results in a mismatch between the GW and electromagnetic luminosity distances, given by

$$\frac{d_L^{\mathrm{GW}}(z)}{d_L^{\mathrm{EM}}(z)} = \exp\left[-\int_0^z \frac{\delta(z')}{1+z'}\,dz'\right]. \tag{6.5}$$

Thus, a nonzero $\delta(z)$ encodes how changes in $M_*(z)$ translate into an apparent amplification or dimming of the GW signal relative to GR expectations.

It is convenient to define a dimensionless parameter describing the rate of Planck-mass evolution,

$$\nu_M \equiv \frac{d \ln M_*^2}{d \ln a} = 2\,\delta(\eta), \tag{6.6}$$

which is often written as $c_M = -\nu_M$ in the literature. Positive ν_M values ($c_M < 0$) correspond to an effective Planck mass that increases with redshift, enhancing the gravitational coupling in the past and making GWs appear brighter than in GR. Conversely, negative ν_M ($c_M > 0$) implies a weaker past coupling and a dimmer signal. A widely used phenomenological parametrization assumes that the friction term scales with the fractional dark-energy density,

$$\delta(z) = -c_M \frac{\Omega_\Lambda(z)}{\Omega_{\Lambda,0}} = -\frac{c_M}{2} \frac{1}{(1+z)^3 \Omega_{m,0} + \Omega_{\Lambda,0}}, \tag{6.7}$$

where Ω_m and Ω_Λ are the present-day matter and dark-energy density parameters, as defined in Section 1.4.1. This simple form captures the key feature that deviations from GR become significant only at late times, when dark energy dominates. The model depends on a single constant c_M, making it efficient for data-analysis applications.

With this parametrization, assuming a flat ΛCDM cosmology, the ratio of GW to EM luminosity distances can be expressed analytically as

$$\frac{d_L^{\rm GW}(z)}{d_L^{\rm EM}(z)} = \exp\left[\frac{c_M}{2\Omega_\Lambda} \ln\left(\frac{\sqrt[3]{\Omega_m(1+z)^3 + \Omega_\Lambda}}{1+z}\right)\right], \tag{6.8}$$

explicitly showing how the deviation depends on the cosmological background and becomes more pronounced as dark energy grows.

Although the c_M parametrization provides a simple and phenomenologically useful framework for modified GW propagation, it does not accurately capture all modified-gravity scenarios, for instance, certain $f(R)$ models [160]. Nonetheless, its single-parameter nature allows efficient exploration of deviations from GR and has been widely adopted in analyses using both bright and dark standard sirens [161, 162]. This framework thus provides a consistent and testable link between cosmological gravity modifications and GW observations.

Extra-Dimensional Scenarios

In theories that extend spacetime beyond four dimensions, such as braneworld or Dvali–Gabadadze–Porrati (DGP) models [163, 164], GWs can partially propagate, or "leak," into the higher-dimensional bulk. This leakage leads to a scale-dependent suppression of the observed GW amplitude relative to GR predictions. A convenient phenomenological parametrization of this effect relates the GW and electromagnetic luminosity

distances as [164, 165]

$$\frac{d_L^{\rm GW}(z)}{d_L^{\rm EM}(z)} = \left[1 + \left(\frac{d_L^{\rm EM}(z)}{(1+z)R_c}\right)^n\right]^{\frac{D-4}{2n}}, \tag{6.9}$$

where D is the total number of spacetime dimensions, R_c denotes the (comoving) screening scale that marks the transition between the four- and higher-dimensional regimes, and n controls the sharpness of this transition.[1] At distances much smaller than the screening scale, $d_L^{\rm EM} \ll (1+z)R_c$, gravity is effectively confined to four dimensions and the general-relativistic limit $d_L^{\rm GW} \simeq d_L^{\rm EM}$ is recovered. At larger distances, $d_L^{\rm EM} \gg (1+z)R_c$, the gravitational field begins to probe the extra dimensions, leading to an amplitude suppression that scales as $d^{-(D-2)/2}$. The GR limit is restored when $D = 4$, irrespective of R_c. These models thus introduce a scale-dependent deviation in GW propagation that complements potential modifications to the cosmological background expansion. The parameter triplet (D, R_c, n) encapsulates the main phenomenological features of higher-dimensional scenarios and can be constrained through joint GW–EM standard siren analyses or, in the absence of counterparts, via dark-siren population studies.

Phenomenological Ξ_0 Parameterization

A widely used, model-independent description of modified GW propagation is given by

$$\frac{d_L^{\rm GW}(z)}{d_L^{\rm EM}(z)} = \Xi_0 + \frac{1-\Xi_0}{(1+z)^n}, \tag{6.10}$$

where Ξ_0 and n are free parameters, and the GR limit corresponds to $\Xi_0 = 1$ (regardless of n). This formulation captures the key phenomenology of many modified gravity theories while remaining agnostic about their microphysical origin. At low redshift ($z \ll 1$), the two luminosity distances coincide, $d_L^{\rm GW} \approx d_L^{\rm EM}$, in agreement with local gravity tests. At high redshift ($z \gg 1$), the ratio asymptotes to $d_L^{\rm GW} \to \Xi_0\, d_L^{\rm EM}$, corresponding to a constant amplitude rescaling. Values $\Xi_0 < 1$ imply a reduced effective damping, GWs appear brighter for a given $d_L^{\rm EM}$, whereas $\Xi_0 > 1$ indicates additional attenuation. The parameter n controls the redshift-dependent transition between these regimes. Although purely phenomenological, this parametrization reproduces the behavior of many explicit modified gravity models. In particular, nonlocal gravity theories with actions containing terms $\propto m^2 R\Box^{-2}R$ predict $\Xi_0 \approx 0.97$ and $n \approx 2.5$. In Horndeski and scalar–tensor frameworks, where the Lagrangian includes terms $G_4(\phi, X)R$, the parameters (Ξ_0, n) encode the time evolution of the effective Planck mass $M_{\rm Pl,eff}^2 \propto G_4$. Similar correspondences arise in Degenerate Higher-Order Scalar–Tensor (DHOST) and certain $f(R)$ models, where the modified friction term in the tensor propagation equation drives the amplitude variation. From an observational

[1] The parameter n is defined differently from the convention used in [164].

standpoint, modifications to GW propagation generally produce more pronounced effects than changes in the dark energy equation of state. This is because degeneracies among cosmological parameters such as H_0 and Ω_m can mask variations in $w_{\rm DE}(z)$, whereas modified propagation directly alters the ratio $d_L^{\rm GW}/d_L^{\rm EM}$ by a factor Ξ_0, independently of such compensations. For typical models with $|w_{\rm DE}(z)+1| \sim 0.1$ and $|\Xi_0 - 1| \sim 0.03$, the propagation effect can therefore dominate the observable signal. Sensitivity to these parameters depends on the redshift range of the observed sources. At low redshift ($z \ll 1$), deviations scale approximately as $\Delta d_L/d_L \sim (1-\Xi_0)nz$, limiting the constraining power of nearby events such as GW170817. The intermediate redshift regime ($z \sim 0.5$–2) offers optimal sensitivity for next-generation detectors like the Einstein Telescope, where deviations become significant while systematic uncertainties remain moderate. At high redshift ($z \gg 1$), the ratio approaches a constant Ξ_0, providing a clean probe of asymptotic propagation effects. Although degeneracies between Ξ_0 and n can hinder constraints near the GR limit, a sufficiently broad population of sources across redshift can break these degeneracies and reveal the evolution encoded in n. A comparative summary of these parameterizations is provided in Table 6.1.

Table 6.1: *Comparison of modified gravity parametrizations for GW propagation. The three models probe complementary aspects of modified gravity through distinct physical mechanisms and observational signatures.*

Model	Free Parameters	GR Limit	Primary Signature
(Ξ_0, n)	Ξ_0, n	$\Xi_0 = 1$	Phenomenological friction; constant ratio $d_L^{\rm GW}/d_L^{\rm EM}$ at high-z
Extra Dimensions	D, R_c, n	$D = 4$	Screening scale; distance-dependent transition between dimensional regimes
c_M (Running Planck Mass)	c_M	$c_M = 0$	Dark energy coupling; late-time modification during dark energy domination

6.2 Methodological Framework

This section outlines the hierarchical Bayesian framework for cosmological inference using GW observations. The central challenge is the mass–redshift degeneracy, which prevents direct inference of the source redshift from GW signals alone. We focus on two complementary strategies to break this degeneracy: the *spectral siren* method, which constrains cosmology through the source-frame mass distribution, and the *galaxy catalog* method, which statistically assigns redshifts using external galaxy surveys. The `icarogw` code implements a unified framework that links the compact binary coalescence (CBC) merger rate to galaxy number density, enabling a joint hierarchical analysis over cosmology and population parameters.

6.2.1 Source-Frame Mass Model: The Spectral Siren Foundation

The spectral siren method infers cosmological parameters by assuming a functional form for the source-frame mass distribution, leveraging the redshift relation $m^d = (1 + z)m^s$. In this work, we adopt the **Power Law + Peak** (PLP) model [166] as our primary population model, which has been used in previous GW catalog analyses [167].
This empirically motivated model provides a parametric approximation of the observed BH mass distribution, which shows two prominent features: a broad peak at lower masses ($\sim 10M_\odot$) and a distinct Gaussian peak around $\sim 35M_\odot$, superimposed on a power-law continuum. The PLP model captures these features by combining a power-law component with a Gaussian peak, while also incorporating a smooth low-mass cutoff and a high-mass cutoff. The model is characterized by eight population parameters. The PLP model is characterized by eight population parameters:

Table 6.2: *PLP population parameters and their descriptions*

Parameter	Description
α	Spectral index for the power-law component of the primary mass distribution
β	Spectral index for the power-law mass ratio distribution
$m_{\min}, m_{\max}$	Minimum and maximum masses of the power-law component
λ_g	Fraction of the population in the Gaussian component
μ_g, σ_g	Mean and width of the Gaussian component around $\sim 35M_\odot$
δ_m	Range of mass tapering at the lower end for smooth cutoff

The joint mass distribution factorizes as:

$$p(m_1, m_2|\Lambda) = p(m_1|\Lambda)S_h(m_1|\Lambda) \times p(m_2|m_1, \Lambda)S_h(m_2|\Lambda), \tag{6.11}$$

where $p(m_2|m_1, \Lambda)$ is the conditional distribution of the secondary mass and $S_h(m|\Lambda)$ is a smoothing function (see [166] for details).

6.2.2 The Galaxy Catalog Method and Completeness

The galaxy catalog method statistically associates GW events with galaxies from astronomical surveys to build a probabilistic redshift prior. A critical limitation is *catalog completeness*, defined as the probability that a galaxy at a given redshift, luminosity, and sky position is included in the survey:

$$C(z, M) = \frac{N_{\text{observed}}(z, M)}{N_{\text{true}}(z, M)}. \tag{6.12}$$

Because most surveys are flux-limited, completeness decreases with redshift, and high-redshift catalogs provide limited constraining power. To correct for incompleteness,

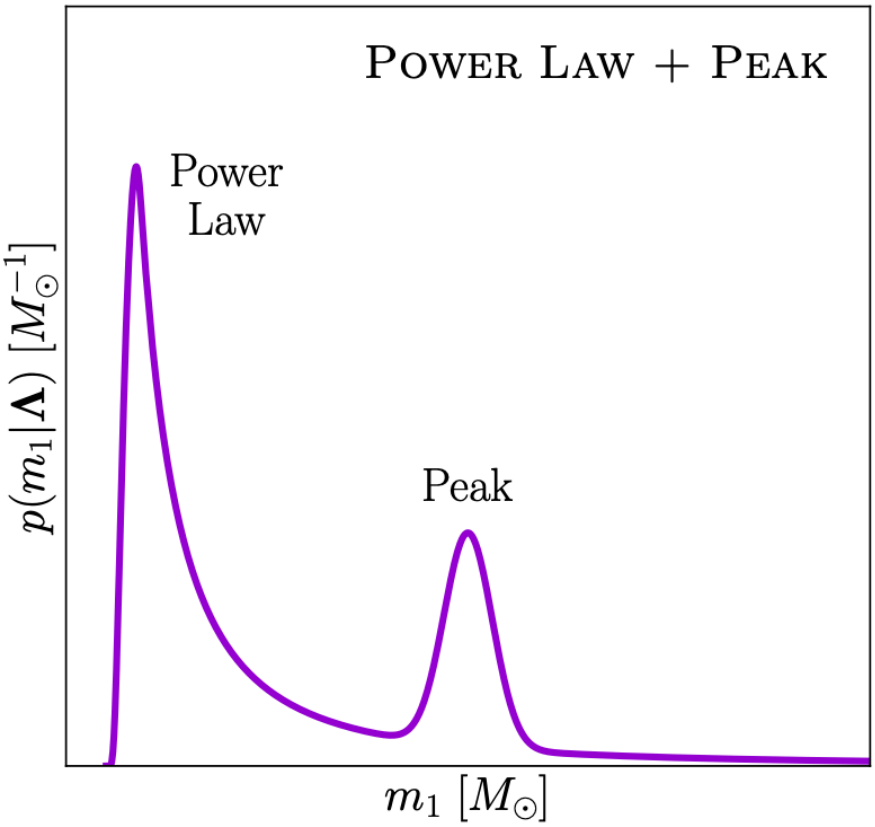

Figure 6.1: *Qualitative representation of the source-frame mass model of BHs (Power Law + Peak) used in this work. The model is empirically motivated, reflecting observed features in the mass distribution. The mass ranges shown are not to scale. Adapted from* [168].

the observed galaxy density is adjusted using the Schechter function, an empirical model for the galaxy luminosity function. Population assumptions enter this method in two key ways: (i) they introduce systematic preferences among host candidates at different redshifts, and (ii) they inform the *completeness correction*. A crucial parameter is ϵ, which describes how the probability of a galaxy hosting a CBC depends on its luminosity ($\epsilon > 0$ implies that brighter galaxies are more likely hosts). In the limiting case of zero catalog completeness, the galaxy catalog method reduces exactly to the spectral siren approach. Since CBC mergers trace the underlying galaxy density, incorrect modeling of the Schechter function can bias the inferred merger rate and cosmological parameters such as H_0.

The GLADE+ Catalog

For this analysis, we use the *Galaxy List for the Advanced Detector Era Plus* (GLADE+) catalog [169]. GLADE+ is a homogenized compilation from six major surveys, containing over 22 million galaxies and 750,000 quasars, with completeness extending to ~ 130 Mpc. A key advantage of GLADE+ is its inclusion of near-infrared (K-band) observations. Emission at $\sim 2.2\,\mu$m is less affected by dust and traces older stellar populations, making it a robust proxy for stellar mass. Consequently, GLADE+ provides reliable stellar mass estimates, which are crucial for weighting galaxies by their expected merger rates in our statistical dark-siren framework.

6.2.3 Hierarchical Likelihood for GW Events

We observe a set of $N_{\rm GW}$ GW events over an observing time $T_{\rm obs}$, where each event i yields data x_i in the form of strain time series or parameter-estimation samples. The population is described by a set of hyperparameters $\Lambda = \{\Lambda_p, \Lambda_c\}$, comprising population parameters Λ_p that describe source characteristics such as mass distributions and merger rates, and cosmological parameters Λ_c that include the Hubble constant H_0, modified gravity parameters such as Ξ_0, and other cosmological quantities. Since GW detections follow an inhomogeneous Poisson process, the joint likelihood for the observed events takes the form:

$$\mathcal{L}(\{x_i\} \mid \Lambda) \propto e^{-N_{\rm exp}(\Lambda)} \prod_{i=1}^{N_{\rm GW}} \int d\theta\, dz\, p_{\rm GW}(x_i \mid \theta, z, \Lambda_c)\, \frac{dN_{\rm CBC}}{d\theta\, dz\, dt_s}(\Lambda)\, \frac{1}{1+z}, \tag{6.13}$$

where $N_{\rm exp}(\Lambda)$ represents the expected number of detectable events given the hyperparameters Λ, accounting for selection biases in the detection process. This expression consists of a Poisson term for the total number of detections and a product of likelihoods for each individual event, marginalized over the unknown source parameters and redshift. This formulation explicitly links population-level properties, encoded in Λ_p, with cosmological parameters Λ_c, allowing the entire analysis to remain self-consistent under hierarchical inference. The term $p_{\rm GW}(x_i \mid \theta, z, \Lambda_c)$ denotes the GW

likelihood for event i, conditioned on source parameters θ such as masses, spins, and orientation, along with redshift z. The quantity $dN_{\rm CBC}/(d\theta\, dz\, dt_s)$ describes the intrinsic merger rate density in the source rest frame, expressed per unit redshift, source time, and source parameters. The factor $1/(1+z)$ accounts for cosmic time dilation between source time and detector-frame time, a crucial relativistic correction. In practical implementations, one often employs a scale-free formulation of the likelihood by marginalizing over $N_{\rm exp}$, typically assuming a $1/N_{\rm exp}$ prior. This approach yields an expression that does not depend explicitly on $N_{\rm exp}$ while still properly accounting for selection biases. The resulting hierarchical likelihood takes the form:

$$\mathcal{L}(\{x_i\} \mid \Lambda) \propto \prod_{i=1}^{N_{\rm GW}} \frac{\int d\theta\, dz\, p_{\rm GW}(x_i \mid \theta, z)\, \pi_{\rm pop}(\theta, z \mid \Lambda)}{\int d\theta\, dz\, P_{\rm det}(\theta, z; \Lambda)\, \pi_{\rm pop}(\theta, z \mid \Lambda)}, \tag{6.14}$$

where $P_{\rm det}(\theta, z)$ represents the detection probability or selection function, and $\pi_{\rm pop}$ denotes the prior predictive distribution for the source parameters and redshifts. This formulation marginalizes over the overall rate normalization R_0, reducing sensitivity to its absolute value.

6.2.4 Modeling Compact Binary Coalescence Merger Rates and Populations

A fundamental component of the hierarchical framework is the model for the compact binary coalescence merger rate density as a function of redshift, mass, and other source parameters. Two complementary approaches are commonly employed in the literature. The spectral siren parametrization expresses the merger rate per comoving volume as:

$$\frac{dN_{\rm CBC}}{d\theta\, dz\, dt_s} = R_0\, \psi(z; \Lambda_p)\, p_{\rm pop}(\theta \mid \Lambda_p)\, \frac{dV_c}{dz\, d\Omega}, \tag{6.15}$$

where R_0 represents the local merger rate, $\psi(z)$ describes the redshift evolution of the merger rate normalized such that $\psi(0) = 1$, and $p_{\rm pop}(\theta)$ gives the normalized distribution of source parameters, typically assumed to be independent of redshift in the simplest models. The comoving volume element $dV_c/(dz\, d\Omega)$ provides the crucial link between redshift and spatial volume. Alternatively, the galaxy-informed parametrization, also known as the galaxy density method, assumes that mergers occur within galaxies and expresses the merger rate in terms of galaxy number densities and properties such as luminosity or stellar mass. Formally, this approach writes:

$$\frac{dN_{\rm CBC}}{d\theta\, d\Omega\, dz\, dt_s} = \int dM\, \frac{dN_{\rm CBC}}{dN_{\rm gal}\, d\theta\, dt_s}(M, z)\, \frac{dN_{\rm gal}}{dz\, d\Omega\, dM}, \tag{6.16}$$

where M represents galaxy properties (e.g., absolute magnitude, stellar mass), $dN_{\rm gal}/(dz\, d\Omega\, dM)$ gives the galaxy number density corrected for catalog incompleteness, and $dN_{\rm CBC}/(dN_{\rm gal} \cdot d\theta\, dt_s)$ describes the merger rate per galaxy, which may depend on both M and z. The key insight unifying these approaches is that the galaxy-informed method encompasses the spectral-siren approach in the limit of a fully complete galaxy catalog.

This unified treatment provides a consistent framework for cosmological inference that leverages all available information, from the intrinsic CBC population to the observed galaxy distribution, while remaining robust to catalog incompleteness and population uncertainties.

6.2.5 Treatment of Selection Bias Through Detection Probability

The detection probability $P_{\rm det}(\theta, z)$ quantifies the probability that a source with parameters (θ, z) would be observed, meaning it passes the detection threshold established by the analysis pipeline. This probability depends on various factors including the source's distance, masses, orientation relative to the detectors, and the instrumental sensitivity characteristics. In the hierarchical likelihood framework, this term enters as a normalization factor in the denominator, serving to correct for selection biases by ensuring that inferences are conditioned only on the events we actually observed. Mathematically, the expected number of detectable events is given by:

$$N_{\rm exp}(\Lambda) = T_{\rm obs} \int d\theta\, dz\, P_{\rm det}(\theta, z)\, \frac{dN_{\rm CBC}}{d\theta\, dz\, dt_s}, \tag{6.17}$$

or equivalently, it appears in the denominator of the scale-free likelihood as the integral $\int d\theta\, dz\, P_{\rm det}(\theta, z)\, \pi_{\rm pop}(\theta, z \mid \Lambda)$. This normalization ensures that parameter inferences remain unbiased despite the fact that we only detect the loudest, most observable events, preventing systematic errors that would otherwise arise from ignoring the population of undetected sources. This normalization prevents inferences from being biased towards the types of loud, nearby sources that are easiest to detect.

6.2.6 Marginalization Over Host Galaxy Redshift for Dark Sirens

For dark sirens, events without electromagnetic counterparts, the redshift must be inferred statistically by marginalizing over possible host galaxies using information from galaxy catalogs. The posterior distribution for the hyperparameters Λ, obtained through Bayes' theorem, includes integrals over redshift space:

$$\mathcal{L}_i(\Lambda) = \int dz\, p(z \mid \text{galaxy catalog}, \Omega) \int d\theta\, p_{\rm GW}(x_i \mid \theta, z)\, \pi_{\rm pop}(\theta, z \mid \Lambda), \tag{6.18}$$

where $p(z \mid \text{catalog}, \Omega)$ represents the redshift probability distribution conditional on sky position Ω, constructed from catalog galaxies with appropriate modeling of catalog incompleteness. These individual event likelihoods $\mathcal{L}_i$ are then incorporated into the hierarchical likelihood product across all events, with proper division by the selection normalization as described previously. In practice, the galaxy density method extends this framework by tying the merger rate per galaxy directly to galaxy number densities, allowing simultaneous treatment of catalog incompleteness and host uncertainty. This method offers a natural framework for handling incomplete catalogs and provides a principled approach to redshift marginalization that properly accounts for

uncertainties in galaxy identification and characterization.

6.3 Results: Testing Modified Gravity with GWTC-3 BBHs

We apply the hierarchical Bayesian framework introduced in Section 6.2 to constrain the three phenomenological models of modified gravity described in Section 6.1.2. The analysis uses 42 BBH events from GWTC-3, selected with signal-to-noise ratio $\mathrm{SNR} > 11$ and inverse false alarm rate $\mathrm{IFAR} > 4$ years.

6.3.1 Analysis Configuration

To mitigate strong degeneracies betweeen the Hubble constant and modified gravity parameters (Section 6.2), we fix the Hubble constant to $H_0 = 67.7$ km s^{-1} Mpc^{-1} in all analyses. Given the current sample size, simultaneous inference of H_0 and modified gravity parameters remains statistically limited. The BBH population model follows the Power Law + Peak mass distribution with Madau–Dickinson redshift evolution [170]. Population hyperparameters are allowed to vary within the prior ranges listed in Table 6.3. For each modified gravity scenario, we perform two complementary anal-

Table 6.3: *Prior distributions adopted for modified gravity parameters. $\mathcal{U}(a,b)$ denotes a uniform distribution between a and b, while Log-$\mathcal{U}$ indicates a log-uniform distribution.*

Model	Parameter	Description	Prior Range
Ξ_0	Ξ_0	Deviation amplitude	$\mathcal{U}(0.1, 50)$
Ξ_0	n_{Ξ_0}	Redshift power-law index	$\mathcal{U}(1, 10)$
Extra Dimensions	D	Number of spacetime dimensions	$\mathcal{U}(3.6, 8)$
Extra Dimensions	n_D	Scaling exponent	Log-$\mathcal{U}(0.1, 100)$
Extra Dimensions	R_c	Screening distance	Log-$\mathcal{U}(10, 10^5)$ Mpc
Running Planck	c_M	Planck mass evolution parameter	$\mathcal{U}(-10, 50)$

yses: (1) a *spectral siren* approach (Section 6.2.1), which extracts cosmological information solely from the source-frame mass distribution, and (2) a *catalog+spectral* method (Section 6.2.2), which incorporates redshift information from the GLADE+ galaxy catalog, weighted by K-band luminosity ($\epsilon = 1$).

6.3.2 Results: Constraints on Modified Gravity Parameters

Running Planck Mass Model

The marginalized posterior distribution for the running Planck mass parameter c_M is shown in Figure 6.2. The parameter quantifies deviations in the effective Planck mass, which would alter the amplitude–distance relation of GWs described in Equation 6.7. Both analyses yield results consistent with GR within 1σ, with no significant evidence for a time-varying Planck mass:

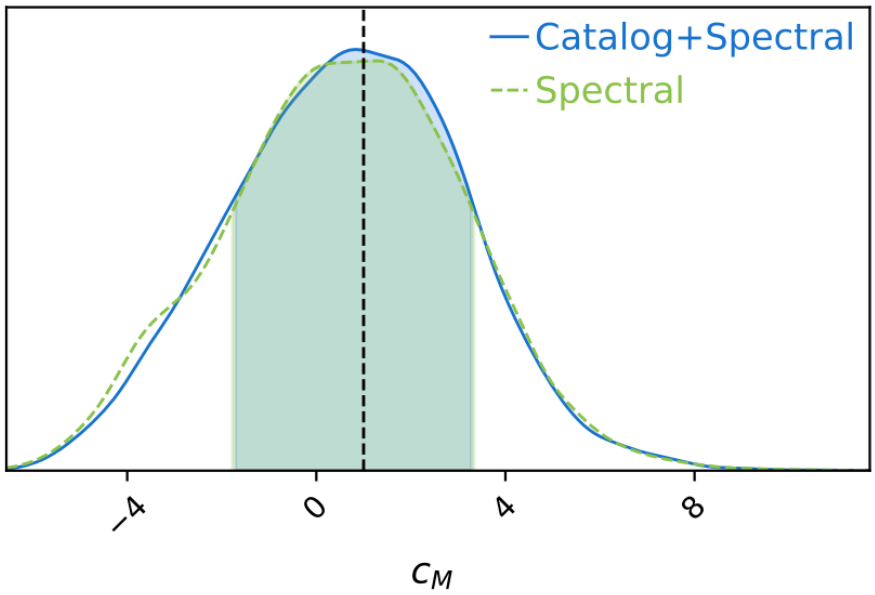

Figure 6.2: *Marginalized posterior distribution for the running Planck mass parameter c_M. The blue solid line represents the catalog+spectral analysis incorporating galaxy survey information, while the green dashed line shows the spectral-only analysis. The vertical black dashed line marks the GR prediction ($c_M = 0$). Shaded regions indicate 68.3% and 90% credible intervals.*

- c_M (Catalog+Spectral): $1.0^{+2.6}_{-3.4}$
- c_M (Spectral Only): $1.6^{+2.2}_{-4.0}$

The similarity between the two approaches reflects that most GWTC-3 BBHs lie at redshifts $z > 0.1$ where galaxy catalog incompleteness becomes significant, making both methods rely primarily on the mass distribution.

Ξ_0 Model

Figure 6.3 displays the joint and marginalized posteriors for the phenomenological Ξ_0 model parameters, which describe deviations in the GW luminosity distance relative to the electromagnetic one through the relation in Equation 6.10.
We find:

- Ξ_0 (Catalog+Spectral): $1.44^{+1.17}_{-0.93}$
- Ξ_0 (Spectral Only): $1.37^{+1.36}_{-0.90}$
- n_{Ξ_0}: The redshift-evolution parameter remains unconstrained within its prior range $[1, 10]$ for both analyses, reflecting the limited leverage of current BBH data in distinguishing redshift-dependent deviations.

The Ξ_0 posteriors peak near unity, consistent with GR. The lack of constraint on the redshift-evolution parameter n_{Ξ_0} reflects the limited leverage of the BBH sample in distinguishing potential redshift dependencies of deviations.

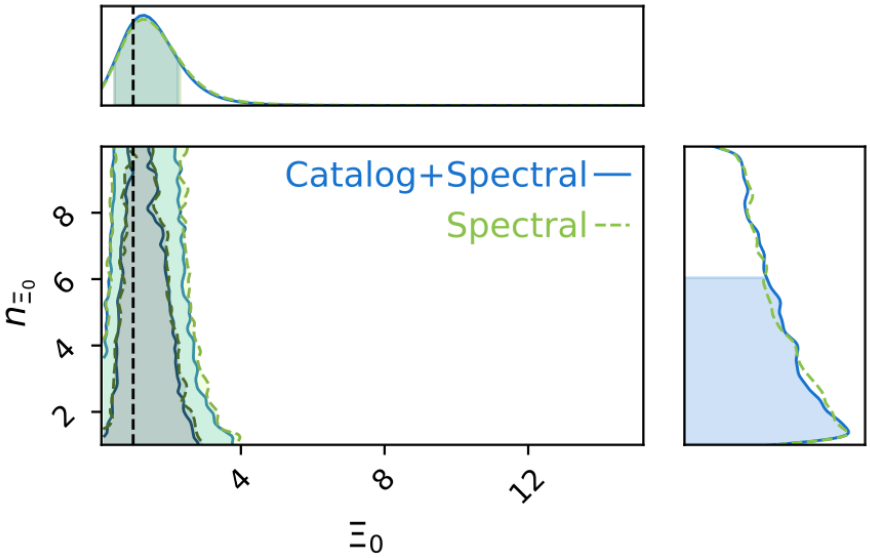

Figure 6.3: *Joint and marginalized posterior distributions for the Ξ_0 model parameters. The 2D contours show 68.3% and 90% credible regions, with blue representing catalog+spectral and green representing spectral-only analyses. The vertical black dashed line in the Ξ_0 panel marks the GR value ($\Xi_0 = 1$). Diagonal plots show marginalized 1D posteriors with 68.3% credible intervals annotated.*

Extra Dimensions Model

The extra-dimensional scenario tests modifications to the GW amplitude due to leakage into higher-dimensional space, described by the luminosity distance ratio in Equation 6.8. The corresponding posteriors are shown in Figure 6.4.
We observe broad, highly degenerate posteriors across all three parameters, with strong correlations between D, n_D, R_c:

- D: Spans most of the prior range $[3.6, 8]$
- R_c: Extends across $[10, 10^5]$ Mpc with strong degeneracy
- n_D: Broad posterior distribution

When $R_c \lesssim 100$ Mpc, deviations would be apparent in nearby events, allowing D to be constrained to values consistent with GR. For larger R_c, deviations occur at higher redshifts where population-model uncertainties dominate the inference. The correlated behavior of D, R_c, and n_D indicates that compensatory effects between parameters can reproduce similar observational signatures. Breaking these degeneracies will require (1) larger event catalogs, (2) improved host-galaxy localization, or (3) bright siren observations with directly measured redshifts.

6.3.3 Comparison: Spectral vs. Catalog+Spectral Methods

Table 6.4 summarizes the modified gravity parameter constraints from both approaches. Across all models, catalog+spectral and spectral-only analyses yield statistically consistent results. The consistent results between methods highlight a fundamental chal-

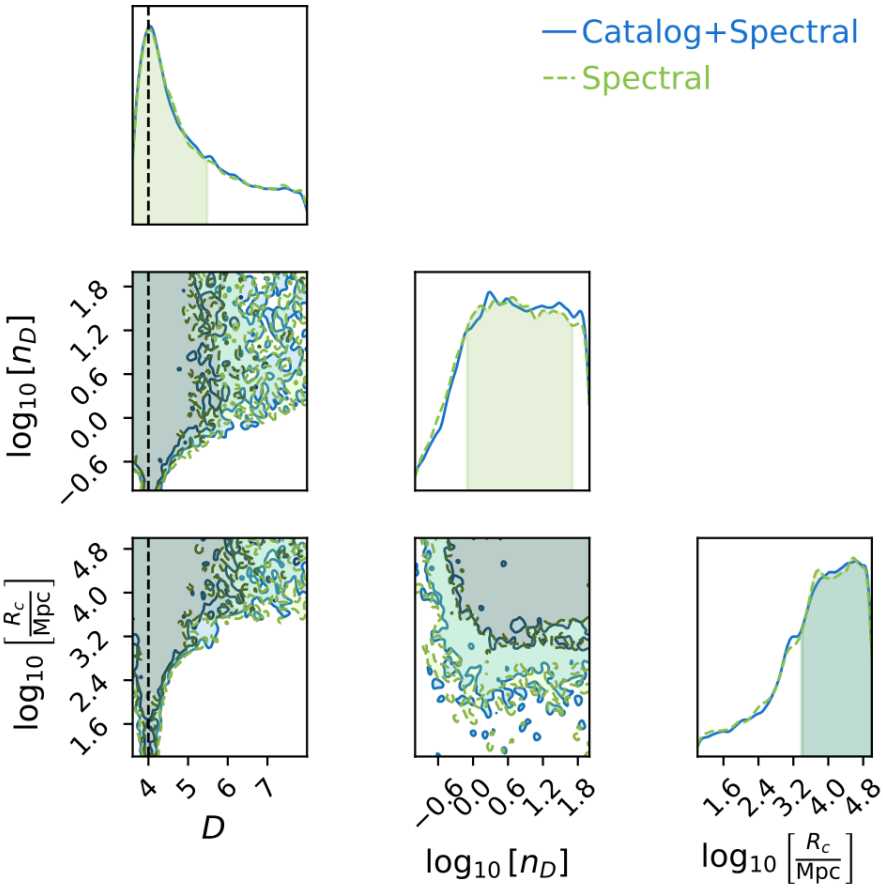

Figure 6.4: *Posterior distributions for extra dimensions model parameters (D, n_D, R_c). The plots display 2D contours at 68.3% and 90% credible levels, with marginalized 1D distributions along the diagonal. Blue contours: catalog+spectral; green contours: spectral-only. The vertical dashed line in the D panel indicates the GR value of four spacetime dimensions.*

Table 6.4: *Comparison of modified gravity parameter constraints from different analysis approaches. Values show maximum a posteriori estimates with symmetric 68.3% credible intervals where well constrained.*

Model	Parameter	Catalog+Spectral	Spectral Only
Running Planck	c_M	$1.0^{+2.6}_{-3.4}$	$1.6^{+2.2}_{-4.0}$
Ξ_0	Ξ_0	$1.44^{+1.17}_{-0.93}$	$1.37^{+1.36}_{-0.90}$
Ξ_0	n_{Ξ_0}	Unconstrained	Unconstrained
Extra Dimensions	D	Weakly constrained	Weakly constrained
Extra Dimensions	R_c [Mpc]	10–10^5	10–10^5
Extra Dimensions	n_D	Broad posterior	Broad posterior

lenge: at redshifts $z \gtrsim 0.1$ where most GWTC-3 BBHs reside, galaxy catalog incompleteness diminishes the additional constraining power of catalog information.

Future improvements are expected as (i) detector sensitivity increases, enabling detection of more nearby BBH mergers where catalogs such as GLADE+ are highly complete, and (ii) forthcoming wide-field surveys extend to fainter magnitudes, enhancing completeness at larger distances.

Our analysis of GWTC-3 BBHs finds no evidence for modified gravity in any of the three frameworks tested. All results are consistent with GR within statistical uncertainties. These represent the tightest constraints from dark siren analyses to date.

Population hyperparameters controlling the BBH mass distribution are summarized in Table 6.5. Their consistency across models confirms that the inferred GR consistency is robust against population model uncertainties.

Table 6.5: *BBH population hyperparameters for different modified gravity analyses. All values represent maximum a posteriori estimates with 68.3% credible intervals. The mass distribution follows the Power Law + Peak model. Consistency across rows demonstrates robustness of population inference to modified gravity assumptions.*

Model	**Analysis Type**	α	β	$m_{\rm min}\,[M_\odot]$	$\mu_g\,[M_\odot]$	$\sigma_g\,[M_\odot]$	λ_g
Ξ_0	C+S	$3.74^{+0.49}_{-0.41}$	$0.8^{+1.2}_{-1.1}$	$4.98^{+0.95}_{-0.64}$	$32.9^{+3.2}_{-2.2}$	-	$0.019^{+0.032}_{-0.018}$
Extra Dim.	C+S	$3.80^{+0.45}_{-0.48}$	$0.6^{+1.2}_{-1.1}$	$5.37^{+0.55}_{-1.02}$	$33.1^{+2.1}_{-2.4}$	$2.3^{+3.0}_{-1.9}$	$0.017^{+0.031}_{-0.015}$
Running Planck	C+S	$3.72^{+0.50}_{-0.45}$	$0.41^{+1.49}_{-0.82}$	$5.08^{+0.78}_{-0.81}$	$32.9^{+2.7}_{-2.8}$	-	$0.018^{+0.031}_{-0.017}$
Ξ_0	S	$3.71^{+0.49}_{-0.40}$	$0.7^{+1.4}_{-1.1}$	$5.14^{+0.77}_{-0.79}$	$33.3^{+2.7}_{-3.1}$	$3.7^{+3.2}_{-2.5}$	$0.018^{+0.035}_{-0.015}$
Extra Dim.	S	$3.86^{+0.42}_{-0.50}$	$0.7^{+1.2}_{-1.1}$	$5.13^{+0.84}_{-0.70}$	33.0 ± 2.3	$2.4^{+3.0}_{-2.0}$	$0.016^{+0.032}_{-0.014}$
Running Planck	S	$3.79^{+0.46}_{-0.50}$	$0.7^{+1.2}_{-1.1}$	$5.22^{+0.64}_{-0.90}$	$32.7^{+2.6}_{-2.7}$	$3.0^{+2.4}_{-2.6}$	$0.017^{+0.032}_{-0.015}$

Looking ahead, third-generation detectors such as the Einstein Telescope and Cosmic Explorer will provide orders of magnitude more detections, improved sky localization, and enhanced redshift inference through expanded catalogs and bright-siren events, significantly strengthening constraints on deviations from GR.

6.4 Conclusion

We have applied a hierarchical Bayesian framework to constrain three phenomenological models of modified gravity using 42 BBH events from GWTC-3. Our analysis combines spectral siren information from the source-frame mass distribution with galaxy catalog data from GLADE+, providing complementary approaches to break the mass-redshift degeneracy.

Across all tested models—running Planck mass, phenomenological Ξ_0, and extra-dimensional scenarios—we find no statistically significant evidence for deviations from general relativity. The running Planck mass parameter is constrained to $c_M = 1.0^{+2.6}_{-3.4}$, the Ξ_0 parameter to $1.44^{+1.17}_{-0.93}$, and extra-dimensional parameters remain weakly constrained within their prior ranges. All results are consistent with GR predictions within measurement uncertainties.

The consistent outcomes between spectral-only and catalog+spectral methods highlight a fundamental limitation of current dark siren analyses: at redshifts $z \gtrsim 0.1$ where most BBHs reside, galaxy catalog incompleteness reduces the additional constraining power of external galaxy data. Consequently, both approaches rely primarily on the source-frame mass distribution for cosmological inference.

These results represent the most comprehensive constraints on modified gravity from dark sirens to date. Future observations with third-generation detectors and deeper galaxy surveys will significantly enhance sensitivity to potential deviations, potentially revealing new physics beyond general relativity or further strengthening its empirical foundation.

7

Discussion and Conclusions

The advent of GW astronomy has opened an unprecedented testing ground for fundamental physics. This thesis has leveraged this new observational window to perform stringent tests of GR and probe the nature of compact objects. The collective results from searches for environmental effects, black hole spectroscopy, and modified gravity, presented in Chapter 4, Chapter 5, and Chapter 6, paint a coherent picture: GR remains robust under a diverse array of novel and extreme probes. Although the analyses explored distinct physical regimes, they converge toward a common conclusion: the standard model of isolated compact binaries evolving under GR provides an excellent description of current GW observations.

- **Environmental effects:** In Chapter 4, a Bayesian search for matter-induced dephasing yielded no detections. This null result supports the validity of the vacuum-binary approximation for the observed population and establishes the first population-level upper limits on ambient density. The most stringent constraint, derived from GW170817, excludes $\tilde{\rho} \gtrsim 21\ \mathrm{g/cm^3}$ for dynamical friction.
- **Black hole spectroscopy:** In Chapter 5, the analysis of O4 data marked a milestone in observational black hole spectroscopy. The confident detection of two quasinormal modes in GW250114 enabled a direct test of the Kerr metric, constraining deviations at the $\sim 30\%$ level. The same event provided a 4.8σ confirmation of Hawking's area theorem, offering the first empirical validation of a cornerstone of black hole thermodynamics.
- **Modified gravity and cosmology:** In Chapter 6, a hierarchical Bayesian analysis of dark sirens constrained phenomenological modifications to GW propagation. The inferred parameters, the running Planck mass, $c_M = 1.0^{+2.6}_{-3.4}$, and the deviation parameter, $\Xi_0 = 1.44^{+1.17}_{-0.93}$, are fully consistent with GR, providing independent constraints on gravitational dynamics at cosmological scales.

Together, these findings highlight the remarkable internal consistency of GW observations with the predictions of GR. Far from being a mere null result, this agreement establishes a quantitative baseline for the next era of GW cosmology and fundamen-

tal physics. The methodologies developed throughout this work lay the groundwork for the next generation of GW science. Third-generation detectors such as the Einstein Telescope and Cosmic Explorer will transform these early tests into precision measurements. They will convert current upper limits on environmental effects into potential detections, enable statistical black hole spectroscopy across thousands of events, and use large samples of dark sirens to probe modified gravity at the sub-percent level. Although GR has withstood every test presented in this thesis, it is ultimately a classical theory, and its reconciliation with quantum mechanics remains one of the greatest challenges in physics. The ultimate goal of these efforts is not confirmation, but discovery. As detector sensitivity and observational reach continue to expand, we probe regimes where quantum gravitational effects may become apparent. Any deviation from GR, however small, would be a monumental discovery, guiding us toward a deeper and more complete quantum theory of gravity.

This page intentionally left blank.

Bibliography

[1] Giada Caneva Santoro et al. "First Constraints on Compact Binary Environments from LIGO-Virgo Data". In: *Phys. Rev. Lett.* 132.25 (2024), p. 251401. DOI: 10.1103/PhysRevLett.132.251401. arXiv: 2309.05061 [gr-qc].

[2] Giada Caneva Santoro et al. "First constraints on binary black hole environments with LIGO-Virgo observations". In: *PoS* EPS-HEP2023 (2024), p. 068. DOI: 10.22323/1.449.0068.

[3] Emanuele Berti et al. "Black hole spectroscopy: from theory to experiment". In: (May 2025). arXiv: 2505.23895 [gr-qc].

[4] LIGO Scientific Collaboration, Virgo Collaboration, and KAGRA Collaboration. "Tests of GR with GWTC-4 III. Tests of the Remnants". In preparation. 2025.

[5] "Black Hole Spectroscopy and Tests of General Relativity with GW250114". In: (Sept. 2025). arXiv: 2509.08099 [gr-qc].

[6] A. G. Abac et al. "GW250114: Testing Hawking's Area Law and the Kerr Nature of Black Holes". In: *Phys. Rev. Lett.* 135.11 (2025), p. 111403. DOI: 10.1103/kw5g-d732. arXiv: 2509.08054 [gr-qc].

[7] "GW230814: investigation of a loud gravitational-wave signal observed with a single detector". In: (Sept. 2025). arXiv: 2509.07348 [gr-qc].

[8] A. G. Abac et al. "GW231123: a Binary Black Hole Merger with Total Mass 190-265 $M_\odot$". In: (July 2025). arXiv: 2507.08219 [astro-ph.HE].

[9] Simone Mastrogiovanni et al. "ICAROGW: A python package for inference of astrophysical population properties of noisy, heterogeneous, and incomplete observations". In: *Astron. Astrophys.* 682 (2024), A167. DOI: 10.1051/0004-6361/202347007. arXiv: 2305.17973 [astro-ph.CO].

[10] Simone Mastrogiovanni et al. "Joint population and cosmological properties inference with gravitational waves standard sirens and galaxy surveys". In: *Phys. Rev. D* 108.4 (2023), p. 042002. DOI: 10.1103/PhysRevD.108.042002. arXiv: 2305.10488 [astro-ph.CO].

[11] Albert Einstein. "The foundation of the general theory of relativity." In: *Annalen Phys.* 49.7 (1916). Ed. by Jong-Ping Hsu and D. Fine, pp. 769–822. DOI: 10.1002/andp.19163540702.

[12] Valeria Ferrari, Leonardo Gualtieri, and Paolo Pani. *General Relativity and its Applications*. CRC Press, Dec. 2020. ISBN: 978-0-429-49140-5, 978-0-367-62532-0. DOI: 10.1201/9780429491405.

[13] Maximiliano Isi. "Parametrizing gravitational-wave polarizations". In: *Class. Quant. Grav.* 40.20 (2023), p. 203001. DOI: 10.1088/1361-6382/acf28c. arXiv: 2208.03372 [gr-qc].

[14] Alessandra Buonanno and Bangalore S. Sathyaprakash. "Sources of Gravitational Waves: Theory and Observations". In: *arXiv preprint* (Oct. 2014). arXiv: 1410.7832 [gr-qc].

[15] Luc Blanchet. "Post-Newtonian Theory for Gravitational Waves". In: *Living Rev. Rel.* 17 (2014), p. 2. DOI: 10.12942/lrr-2014-2. arXiv: 1310.1528 [gr-qc].

[16] Luc Blanchet. "Second postNewtonian generation of gravitational radiation". In: *Phys. Rev. D* 51 (1995), pp. 2559–2583. DOI: 10.1103/PhysRevD.51.2559. arXiv: gr-qc/9501030.

[17] Thibault Damour. "Coalescence of two spinning black holes: an effective one-body approach". In: *Phys. Rev. D* 64 (2001), p. 124013. DOI: 10.1103/PhysRevD.64.124013. arXiv: gr-qc/0103018.

[18] K. G. Arun et al. "Parameter estimation of inspiralling compact binaries using 3.5 post-Newtonian gravitational wave phasing: The Non-spinning case". In: *Phys. Rev. D* 71 (2005). [Erratum: Phys.Rev.D 72, 069903 (2005)], p. 084008. DOI: 10.1103/PhysRevD.71.084008. arXiv: gr-qc/0411146.

[19] Alessandra Buonanno et al. "Comparison of post-Newtonian templates for compact binary inspiral signals in gravitational-wave detectors". In: *Phys. Rev. D* 80 (2009), p. 084043. DOI: 10.1103/PhysRevD.80.084043. arXiv: 0907.0700 [gr-qc].

[20] Curt Cutler and Eanna E. Flanagan. "Gravitational waves from merging compact binaries: How accurately can one extract the binary's parameters from the inspiral wave form?" In: *Phys. Rev. D* 49 (1994), pp. 2658–2697. DOI: 10.1103/PhysRevD.49.2658. arXiv: gr-qc/9402014.

[21] Alessandra Buonanno and Thibault Damour. "Transition from inspiral to plunge in binary black hole coalescences". In: *Phys. Rev. D* 62 (2000), p. 064015. DOI: 10.1103/PhysRevD.62.064015. arXiv: gr-qc/0001013.

[22] Thomas W. Baumgarte and Stuart L. Shapiro. *Numerical Relativity: Solving Einstein's Equations on the Computer*. Cambridge University Press, 2010. DOI: 10.1017/CBO9781139193344.

[23] Jorg Frauendiener. "Miguel Alcubierre: Introduction to 3 + 1 numerical relativity". In: *Gen. Rel. Grav.* 43 (2011), pp. 2931–2933. DOI: 10.1007/s10714-011-1195-5.

[24] T. Nakamura. "Numerical relativity". In: *13th Conference on General Relativity and Gravitation (GR-13)*. 1993, pp. 373–379.

[25] Frans Pretorius. "Evolution of binary black hole spacetimes". In: *Phys. Rev. Lett.* 95 (2005), p. 121101. DOI: 10.1103/PhysRevLett.95.121101. arXiv: gr-qc/0507014.

[26] Saul A. Teukolsky. "Perturbations of a rotating black hole. 1. Fundamental equations for gravitational electromagnetic and neutrino field perturbations". In: *Astrophys. J.* 185 (1973), pp. 635–647. DOI: 10.1086/152444.

[27] William H. Press and Saul A. Teukolsky. "Perturbations of a Rotating Black Hole. II. Dynamical Stability of the Kerr Metric". In: *Astrophys. J.* 185 (1973), pp. 649–674. DOI: 10.1086/152445.

[28] E. W. Leaver. "An Analytic representation for the quasi normal modes of Kerr black holes". In: *Proc. Roy. Soc. Lond. A* 402 (1985), pp. 285–298. DOI: 10.1098/rspa.1985.0119.

[29] W. Rindler. "Visual Horizons in World Models". In: *Mon. Not. Roy. Astron. Soc.* 116.6 (1956), pp. 662–677. DOI: 10.1093/mnras/116.6.662.

[30] Karl Schwarzschild. "On the gravitational field of a mass point according to Einstein's theory". In: *Sitzungsber. Preuss. Akad. Wiss. Berlin (Math. Phys.)* 1916 (1916), pp. 189–196. arXiv: physics/9905030.

[31] David Finkelstein. "Past-Future Asymmetry of the Gravitational Field of a Point Particle". In: *Phys. Rev.* 110 (1958), pp. 965–967. DOI: 10.1103/PhysRev.110.965.

[32] Roy P. Kerr. "Gravitational field of a spinning mass as an example of algebraically special metrics". In: *Phys. Rev. Lett.* 11 (1963), pp. 237–238. DOI: 10.1103/PhysRevLett.11.237.

[33] H. Reissner. "Über die Eigengravitation des elektrischen Feldes nach der Einsteinschen Theorie". In: *Annalen Phys.* 355.9 (1916), pp. 106–120. DOI: 10.1002/andp.19163550905.

[34] Gunnar Nordstrom. "On the Energy of the Gravitation field in Einstein's Theory". In: *Kon. Ned. Akad. Wetensch. Proc.* 20.2 (2018), pp. 1238–1245.

[35] E T. Newman et al. "Metric of a Rotating, Charged Mass". In: *J. Math. Phys.* 6 (1965), pp. 918–919. DOI: 10.1063/1.1704351.

[36] Werner Israel. "Event horizons in static electrovac space-times". In: *Commun. Math. Phys.* 8 (1968), pp. 245–260. DOI: 10.1007/BF01645859.

[37] B. Carter. "Axisymmetric Black Hole Has Only Two Degrees of Freedom". In: *Phys. Rev. Lett.* 26 (1971), pp. 331–333. DOI: 10.1103/PhysRevLett.26.331.

[38] D. C. Robinson. "Uniqueness of the Kerr black hole". In: *Phys. Rev. Lett.* 34 (1975), pp. 905–906. DOI: 10.1103/PhysRevLett.34.905.

[39] Tullio Regge and John A. Wheeler. "Stability of a Schwarzschild singularity". In: *Phys. Rev.* 108 (1957), pp. 1063–1069. DOI: 10.1103/PhysRev.108.1063.

[40] Frank J. Zerilli. "Effective potential for even parity Regge-Wheeler gravitational perturbation equations". In: *Phys. Rev. Lett.* 24 (1970), pp. 737–738. DOI: 10.1103/PhysRevLett.24.737.

[41] D. Christodoulou. "Reversible and irreversible transforations in black hole physics". In: *Phys. Rev. Lett.* 25 (1970), pp. 1596–1597. DOI: 10.1103/PhysRevLett.25.1596.

[42] S. W. Hawking. "Black holes in general relativity". In: *Commun. Math. Phys.* 25 (1972), pp. 152–166. DOI: 10.1007/BF01877517.

[43] S. W. Hawking. "Particle Creation by Black Holes". In: *Commun. Math. Phys.* 43 (1975). Ed. by G. W. Gibbons and S. W. Hawking. [Erratum: Commun.Math.Phys. 46, 206 (1976)], pp. 199–220. DOI: 10.1007/BF02345020.

[44] James M. Bardeen, B. Carter, and S. W. Hawking. "The Four laws of black hole mechanics". In: *Commun. Math. Phys.* 31 (1973), pp. 161–170. DOI: 10.1007/BF01645742.

[45] Jacob D. Bekenstein. "Black holes and entropy". In: *Phys. Rev. D* 7 (1973), pp. 2333–2346. DOI: 10.1103/PhysRevD.7.2333.

[46] A. Friedman. "On the Curvature of space". In: *Z. Phys.* 10 (1922), pp. 377–386. DOI: 10.1007/BF01332580.

[47] Georges Lemaître. "Un univers homogène de masse constante et de rayon croissant rendant compte de la vitesse radiale des nébuleuses extra-galactiques". In: *Annales de la Société Scientifique de Bruxelles, Série A* 47 (1927). Also published in translation as "A homogeneous universe of constant mass and increasing radius accounting for the radial velocity of extra-galactic nebulae", pp. 49–59. DOI: 10.1007/s10714-013-1548-3.

[48] Edwin Hubble. "A relation between distance and radial velocity among extra-galactic nebulae". In: *Proc. Nat. Acad. Sci.* 15 (1929), pp. 168–173. DOI: 10.1073/pnas.15.3.168.

[49] L. Verde, T. Treu, and A. G. Riess. "Tensions between the Early and the Late Universe". In: *Nature Astron.* 3 (2019), p. 891. DOI: 10.1038/s41550-019-0902-0. arXiv: 1907.10625 [astro-ph.CO].

[50] Eleonora Di Valentino et al. "Snowmass2021 - Letter of interest cosmology intertwined II: The hubble constant tension". In: *Astropart. Phys.* 131 (2021), p. 102605. DOI: 10.1016/j.astropartphys.2021.102605. arXiv: 2008.11284 [astro-ph.CO].

[51] N. Aghanim et al. "Planck 2018 results. VI. Cosmological parameters". In: *Astron. Astrophys.* 641 (2020). [Erratum: Astron.Astrophys. 652, C4 (2021)], A6. DOI: 10.1051/0004-6361/201833910. arXiv: 1807.06209 [astro-ph.CO].

[52] Adam G. Riess et al. "Cosmic Distances Calibrated to 1% Precision with Gaia EDR3 Parallaxes and Hubble Space Telescope Photometry of 75 Milky Way Cepheids Confirm Tension with ΛCDM". In: *Astrophys. J. Lett.* 908.1 (2021), p. L6. DOI: 10.3847/2041-8213/abdbaf. arXiv: 2012.08534 [astro-ph.CO].

[53] Eleonora Di Valentino et al. "In the realm of the Hubble tension—a review of solutions". In: *Class. Quant. Grav.* 38.15 (2021), p. 153001. DOI: 10.1088/1361-6382/ac086d. arXiv: 2103.01183 [astro-ph.CO].

[54] Bernard F. Schutz. "Determining the Hubble Constant from Gravitational Wave Observations". In: *Nature* 323 (1986), pp. 310–311. DOI: 10.1038/323310a0.

[55] Daniel E. Holz and Scott A. Hughes. "Using gravitational-wave standard sirens". In: *Astrophys. J.* 629 (2005), pp. 15–22. DOI: 10.1086/431341. arXiv: astro-ph/0504616.

[56] B. P. Abbott et al. "A gravitational-wave standard siren measurement of the Hubble constant". In: *Nature* 551.7678 (2017), pp. 85–88. DOI: 10.1038/nature24471. arXiv: 1710.05835 [astro-ph.CO].

[57] Rich Abbott et al. "Open data from the first and second observing runs of Advanced LIGO and Advanced Virgo". In: *SoftwareX* 13 (2021), p. 100658. DOI: 10.1016/j.softx.2021.100658. arXiv: 1912.11716 [gr-qc].

[58] B. S. Sathyaprakash et al. "Extreme Gravity and Fundamental Physics". In: (Mar. 2019). arXiv: 1903.09221 [astro-ph.HE].

[59] Nur Ismail et al. "Fabry-Pérot resonator: spectral line shapes, generic and related Airy distributions, linewidths, finesses, and performance at low or frequency-dependent reflectivity". In: *Optics Express* 24.15 (July 2016), p. 16366. DOI: 10.1364/OE.24.016366.

[60] Alba Romero Rodríguez. "Study of Gravitational Waves using the LIGO/Virgo data". PhD thesis. Barcelona, Autonoma U., 2022.

[61] Michele Maggiore. *Gravitational Waves. Vol. 1: Theory and Experiments*. Oxford University Press, 2007. ISBN: 978-0-19-171766-6, 978-0-19-852074-0. DOI: 10.1093/acprof:oso/9780198570745.001.0001.

[62] J. Abadie et al. "A Gravitational wave observatory operating beyond the quantum shot-noise limit: Squeezed light in application". In: *Nature Phys.* 7 (2011), pp. 962–965. DOI: 10.1038/nphys2083. arXiv: 1109.2295 [quant-ph].

[63] J. Aasi et al. "Enhancing the sensitivity of the LIGO gravitational wave detector by using squeezed states of light". In: *Nature Photon.* 7 (2013), pp. 613–619. DOI: 10.1038/nphoton.2013.177. arXiv: 1310.0383 [quant-ph].

[64] Lucia Trozzo and Francesca Badaracco. "Seismic and Newtonian Noise in the GW Detectors". In: *Galaxies* 10.1, 20 (Jan. 2022), p. 20. DOI: 10.3390/galaxies10010020.

[65] V. B. Braginsky, M. L. Gorodetsky, and S. P. Vyatchanin. "Thermodynamical fluctuations and photo-thermal shot noise in gravitational wave antennae". In: *Physics Letters A* 264.1 (Dec. 1999), pp. 1–10. DOI: 10.1016/S0375-9601(99)00785-9. arXiv: cond-mat/9912139 [cond-mat.mtrl-sci].

[66] R. Flaminio. "Thermal Noise in Laser Interferometer Gravitational Wave Detectors". In: *Advanced Interferometers and the Search for Gravitational Waves*. Ed. by M. Bassan. Cham: Springer International Publishing, 2014, pp. 285–336. ISBN: 978-3-319-03792-9. DOI: 10.1007/978-3-319-03792-9_8.

[67] Lisa Barsotti et al. *Updated Advanced LIGO Sensitivity Design Curve*. Tech. rep. LIGO-T1800044-v5. Technical note summarizing the update of the Advanced LIGO design curve informed by recent measurement of coating thermal noise. LIGO Laboratory, Mar. 2018. URL: https://dcc.ligo.org/LIGO-T1800044/public.

[68] Piotr Jaranowski and Andrzej Krolak. "Gravitational-Wave Data Analysis. Formalism and Sample Applications: The Gaussian Case". In: *Living Rev. Rel.* 8 (2005), p. 3. DOI: 10.12942/lrr-2012-4. arXiv: 0711.1115 [gr-qc].

[69] Benjamin J. Owen and B. S. Sathyaprakash. "Matched filtering of gravitational waves from inspiraling compact binaries: Computational cost and template placement". In: *Phys. Rev. D* 60 (1999), p. 022002. DOI: 10.1103/PhysRevD.60.022002. arXiv: gr-qc/9808076.

[70] B. P. Abbott et al. "Observation of Gravitational Waves from a Binary Black Hole Merger". In: *Phys. Rev. Lett.* 116.6 (2016), p. 061102. DOI: 10.1103/PhysRevLett.116.061102. arXiv: 1602.03837 [gr-qc].

[71] R. Abbott et al. "GWTC-3: Compact Binary Coalescences Observed by LIGO and Virgo during the Second Part of the Third Observing Run". In: *Phys. Rev. X* 13.4 (2023), p. 041039. DOI: 10.1103/PhysRevX.13.041039. arXiv: 2111.03606 [gr-qc].

[72] Charlie Hoy. "Accelerating multimodel Bayesian inference, model selection, and systematic studies for gravitational wave astronomy". In: *Phys. Rev. D* 106.8 (2022), p. 083003. DOI: 10.1103/PhysRevD.106.083003. arXiv: 2208.00106 [gr-qc].

[73] Vijay Varma et al. "Surrogate models for precessing binary black hole simulations with unequal masses". In: *Phys. Rev. Research.* 1 (2019), p. 033015. DOI: 10.1103/PhysRevResearch.1.033015. arXiv: 1905.09300 [gr-qc].

[74] Serguei Ossokine et al. "Multipolar Effective-One-Body Waveforms for Precessing Binary Black Holes: Construction and Validation". In: *Phys. Rev. D* 102.4 (2020), p. 044055. DOI: 10.1103/PhysRevD.102.044055. arXiv: 2004.09442 [gr-qc].

[75] Roberto Cotesta et al. "Enriching the Symphony of Gravitational Waves from Binary Black Holes by Tuning Higher Harmonics". In: *Phys. Rev. D* 98.8 (2018), p. 084028. DOI: 10.1103/PhysRevD.98.084028. arXiv: 1803.10701 [gr-qc].

[76] Geraint Pratten et al. "Computationally efficient models for the dominant and subdominant harmonic modes of precessing binary black holes". In: *Phys. Rev. D* 103.10 (2021), p. 104056. DOI: 10.1103/PhysRevD.103.104056. arXiv: 2004.06503 [gr-qc].

[77] Cecilio García-Quirós et al. "Multimode frequency-domain model for the gravitational wave signal from nonprecessing black-hole binaries". In: *Phys. Rev. D* 102.6 (2020), p. 064002. DOI: 10.1103/PhysRevD.102.064002. arXiv: 2001.10914 [gr-qc].

[78] Patricia Schmidt, Mark Hannam, and Sascha Husa. "Towards models of gravitational waveforms from generic binaries: A simple approximate mapping between precessing and non-precessing inspiral signals". In: *Phys. Rev. D* 86 (2012), p. 104063. DOI: 10.1103/PhysRevD.86.104063. arXiv: 1207.3088 [gr-qc].

[79] Mark Hannam et al. "Simple Model of Complete Precessing Black-Hole-Binary Gravitational Waveforms". In: *Phys. Rev. Lett.* 113.15 (2014), p. 151101. DOI: 10.1103/PhysRevLett.113.151101. arXiv: 1308.3271 [gr-qc].

[80] Héctor Estellés et al. "New twists in compact binary waveform modeling: A fast time-domain model for precession". In: *Phys. Rev. D* 105.8 (2022), p. 084040. DOI: 10.1103/PhysRevD.105.084040. arXiv: 2105.05872 [gr-qc].

[81] Héctor Estellés et al. "Time-domain phenomenological model of gravitational-wave subdominant harmonics for quasicircular nonprecessing binary black hole coalescences". In: *Phys. Rev. D* 105.8 (2022), p. 084039. DOI: 10.1103/PhysRevD.105.084039. arXiv: 2012.11923 [gr-qc].

[82] E. Capote et al. "Advanced LIGO detector performance in the fourth observing run". In: *Phys. Rev. D* 111.6 (2025), p. 062002. DOI: 10.1103/PhysRevD.111.062002. arXiv: 2411.14607 [gr-qc].

[83] B. P. Abbott et al. "GWTC-1: A Gravitational-Wave Transient Catalog of Compact Binary Mergers Observed by LIGO and Virgo during the First and Second Observing Runs". In: *Phys. Rev. X* 9.3 (2019), p. 031040. DOI: 10.1103/PhysRevX.9.031040. arXiv: 1811.12907 [astro-ph.HE].

[84] R. Abbott et al. "GWTC-2: Compact Binary Coalescences Observed by LIGO and Virgo During the First Half of the Third Observing Run". In: *Phys. Rev. X* 11 (2021), p. 021053. DOI: 10.1103/PhysRevX.11.021053. arXiv: 2010.14527 [gr-qc].

[85] R. Abbott et al. "GWTC-2.1: Deep extended catalog of compact binary coalescences observed by LIGO and Virgo during the first half of the third observing run". In: *Phys. Rev. D* 109.2 (2024), p. 022001. DOI: 10.1103/PhysRevD.109.022001. arXiv: 2108.01045 [gr-qc].

[86] Simon F. Portegies Zwart and Stephen McMillan. "Black hole mergers in the universe". In: *Astrophys. J. Lett.* 528 (2000), p. L17. DOI: 10.1086/312422. arXiv: astro-ph/9910061.

[87] Carl L. Rodriguez et al. "Binary Black Hole Mergers from Globular Clusters: Implications for Advanced LIGO". In: *Phys. Rev. Lett.* 115.5 (2015). [Erratum: Phys.Rev.Lett. 116, 029901 (2016)], p. 051101. DOI: 10.1103/PhysRevLett.115.051101. arXiv: 1505.00792 [astro-ph.HE].

[88] Carl L. Rodriguez et al. "Illuminating Black Hole Binary Formation Channels with Spins in Advanced LIGO". In: *Astrophys. J. Lett.* 832.1 (2016), p. L2. DOI: 10.3847/2041-8205/832/1/L2. arXiv: 1609.05916 [astro-ph.HE].

[89] Fabio Antonini et al. "Coalescing black hole binaries from globular clusters: mass distributions and comparison to gravitational wave data from GWTC-3". In: *Mon. Not. Roy. Astron. Soc.* 522.1 (2023), pp. 466–476. DOI: 10.1093/mnras/stad972. arXiv: 2208.01081 [astro-ph.HE].

[90] Kyle Kremer. "Compact Objects in Globular Clusters". In: (Aug. 2025). arXiv: 2508.14308 [astro-ph.HE].

[91] Ryan M. O'Leary, Bence Kocsis, and Abraham Loeb. "Gravitational waves from scattering of stellar-mass black holes in galactic nuclei". In: *Mon. Not. Roy. Astron. Soc.* 395.4 (2009), pp. 2127–2146. DOI: 10.1111/j.1365-2966.2009.14653.x. arXiv: 0807.2638 [astro-ph].

[92] Bao-Minh Hoang et al. "Black Hole Mergers in Galactic Nuclei Induced by the Eccentric Kozai–Lidov Effect". In: *Astrophys. J.* 856.2 (2018), p. 140. DOI: 10.3847/1538-4357/aaafce. arXiv: 1706.09896 [astro-ph.HE].

[93] Sourav Chatterjee, Carl L. Rodriguez, and Frederic A. Rasio. "Binary Black Holes in Dense Star Clusters: Exploring the Theoretical Uncertainties". In: 834.1, 68 (Jan. 2017), p. 68. DOI: 10.3847/1538-4357/834/1/68. arXiv: 1603.00884 [astro-ph.GA].

[94] Fabio Antonini and Frederic A. Rasio. "Merging black hole binaries in galactic nuclei: implications for advanced-LIGO detections". In: *Astrophys. J.* 831.2 (2016), p. 187. DOI: 10.3847/0004-637X/831/2/187. arXiv: 1606.04889 [astro-ph.HE].

[95] B McKernan et al. "Intermediate mass black holes in AGN discs–I. Production and growth". In: *Monthly Notices of the Royal Astronomical Society* 425.1 (2012), pp. 460–469.

[96] Jillian M. Bellovary et al. "Migration Traps in Disks Around Supermassive Black Holes". In: *Astrophys. J. Lett.* 819.2 (2016), p. L17. DOI: 10.3847/2041-8205/819/2/L17. arXiv: 1511.00005 [astro-ph.GA].

[97] Nicholas C. Stone, Brian D. Metzger, and Zoltán Haiman. "Assisted inspirals of stellar mass black holes embedded in AGN discs: solving the 'final au problem'". In: *Mon. Not. Roy. Astron. Soc.* 464.1 (2017), pp. 946–954. DOI: 10.1093/mnras/stw2260. arXiv: 1602.04226 [astro-ph.GA].

[98] Imre Bartos et al. "Rapid and Bright Stellar-mass Binary Black Hole Mergers in Active Galactic Nuclei". In: *Astrophys. J.* 835.2 (2017), p. 165. DOI: 10.3847/1538-4357/835/2/165. arXiv: 1602.03831 [astro-ph.HE].

[99] B. Mckernan et al. "Constraining Stellar-mass Black Hole Mergers in AGN Disks Detectable with LIGO". In: *Astrophys. J.* 866.1 (2018), p. 66. DOI: 10.3847/1538-4357/aadae5. arXiv: 1702.07818 [astro-ph.HE].

[100] B. McKernan et al. "Ram-pressure stripping of a kicked Hill sphere: Prompt electromagnetic emission from the merger of stellar mass black holes in an AGN accretion disk". In: *Astrophys. J. Lett.* 884.2 (2019), p. L50. DOI: 10.3847/2041-8213/ab4886. arXiv: 1907.03746 [astro-ph.HE].

[101] Alexandre Toubiana et al. "Detectable environmental effects in GW190521-like black-hole binaries with LISA". In: *Phys. Rev. Lett.* 126.10 (2021), p. 101105. DOI: 10.1103/PhysRevLett.126.101105. arXiv: 2010.06056 [astro-ph.HE].

[102] A. Derdzinski et al. "Evolution of gas disc–embedded intermediate mass ratio inspirals in the *LISA* band". In: *Mon. Not. Roy. Astron. Soc.* 501.3 (2021), pp. 3540–3557. DOI: 10.1093/mnras/staa3976. arXiv: 2005.11333 [astro-ph.HE].

[103] Lorenz Zwick et al. "Dirty waveforms: multiband harmonic content of gas-embedded gravitational wave sources". In: *Mon. Not. Roy. Astron. Soc.* 511.4 (2022), pp. 6143–6159. DOI: 10.1093/mnras/stac299. arXiv: 2110.09097 [astro-ph.HE].

[104] Philippa S. Cole et al. "Distinguishing environmental effects on binary black hole gravitational waveforms". In: *Nature Astron.* 7.8 (2023), pp. 943–950. DOI: 10.1038/s41550-023-01990-2. arXiv: 2211.01362 [gr-qc].

[105] Vitor Cardoso and Caio F. B. Macedo. "Drifting through the medium: kicks and self-propulsion of binaries within accretion discs and other environments". In: *Mon. Not. Roy. Astron. Soc.* 498.2 (2020), pp. 1963–1972. DOI: 10.1093/mnras/staa2396. arXiv: 2008.01091 [astro-ph.HE].

[106] H. Bondi and F. Hoyle. "On the mechanism of accretion by stars". In: *Mon. Not. Roy. Astron. Soc.* 104 (1944), p. 273.

[107] H. Bondi. "On spherically symmetrical accretion". In: *Mon. Not. Roy. Astron. Soc.* 112 (1952), p. 195. DOI: 10.1093/mnras/112.2.195.

[108] Loren I. Petrich et al. "Accretion onto a Moving Black Hole: A Fully Relativistic Treatment". In: 336 (Jan. 1989), p. 313. DOI: 10.1086/167013.

[109] Subrahmanyan Chandrasekhar. "Dynamical Friction. I. General Considerations: the Coefficient of Dynamical Friction". In: *Astrophys. J.* 97 (1943), p. 255. DOI: 10.1086/144517.

[110] M. A. Ruderman and E. A. Spiegel. "Galactic Wakes". In: 165 (Apr. 1971), p. 1. DOI: 10.1086/150870.

[111] Y. Rephaeli and E. E. Salpeter. "Flow past a massive object and the gravitational drag". In: 240 (Aug. 1980), pp. 20–24. DOI: 10.1086/158202.

[112] S. Tremaine and M. D. Weinberg. "Dynamical friction in spherical systems." In: *Mon. Not. Roy. Astron. Soc.* 209 (Aug. 1984), pp. 729–757. DOI: 10.1093/mnras/209.4.729.

[113] Eve C. Ostriker. "Dynamical friction in a gaseous medium". In: *Astrophys. J.* 513 (1999), p. 252. DOI: 10.1086/306858. arXiv: astro-ph/9810324 [astro-ph].

[114] Enrico Barausse. "Relativistic dynamical friction in a collisional fluid". In: *Mon. Not. Roy. Astron. Soc.* 382 (2007), pp. 826–834. DOI: 10.1111/j.1365-2966.2007.12408.x. arXiv: 0709.0211 [astro-ph].

[115] Enrico Barausse, Vitor Cardoso, and Paolo Pani. "Environmental Effects for Gravitational-wave Astrophysics". In: *J. Phys. Conf. Ser.* 610.1 (2015). Ed. by Giacomo Ciani, John W. Conklin, and Guido Mueller, p. 012044. DOI: 10.1088/1742-6596/610/1/012044. arXiv: 1404.7140 [astro-ph.CO].

[116] Abraham Loeb. "Electromagnetic Counterparts to Black Hole Mergers Detected by LIGO". In: *Astrophys. J. Lett.* 819.2 (2016), p. L21. DOI: 10.3847/2041-8205/819/2/L21. arXiv: 1602.04735 [astro-ph.HE].

[117] Paolo Gondolo and Joseph Silk. "Dark matter annihilation at the galactic center". In: *Phys. Rev. Lett.* 83 (1999), pp. 1719–1722. DOI: 10.1103/PhysRevLett.83.1719. arXiv: astro-ph/9906391.

[118] Laleh Sadeghian, Francesc Ferrer, and Clifford M. Will. "Dark matter distributions around massive black holes: A general relativistic analysis". In: *Phys. Rev. D* 88.6 (2013), p. 063522. DOI: 10.1103/PhysRevD.88.063522. arXiv: 1305.2619 [astro-ph.GA].

[119] Richard Brito, Vitor Cardoso, and Paolo Pani. "Superradiance: New Frontiers in Black Hole Physics". In: *Lect. Notes Phys.* 906 (2015), pp.1–237. DOI: 10.1007/978-3-319-19000-6. arXiv: 1501.06570 [gr-qc].

[120] Michalis Agathos et al. "TIGER: A data analysis pipeline for testing the strong-field dynamics of general relativity with gravitational wave signals from coalescing compact binaries". In: *Phys. Rev. D* 89.8 (2014), p. 082001. DOI: 10.1103/PhysRevD.89.082001. arXiv: 1311.0420 [gr-qc].

[121] Gregorio Carullo, Walter Del Pozzo, and John Veitch. *pyRing: a time-domain ringdown analysis python package*. git.ligo.org/lscsoft/pyring. Version 2.3.0. July 2023. DOI: 10.5281/zenodo.8165507. URL: https://doi.org/10.5281/zenodo.8165507.

[122] Gregorio Carullo, Walter Del Pozzo, and John Veitch. "Observational Black Hole Spectroscopy: A time-domain multimode analysis of GW150914". In: *Phys. Rev. D* 99.12 (2019). [Erratum: Phys.Rev.D 100, 089903 (2019)], p. 123029. DOI: 10.1103/PhysRevD.99.123029. arXiv: 1902.07527 [gr-qc].

[123] Maximiliano Isi and Will M. Farr. "Analyzing black-hole ringdowns". In: (July 2021). arXiv: 2107.05609 [gr-qc].

[124] Maximiliano Isi et al. "Testing the no-hair theorem with GW150914". In: *Phys. Rev. Lett.* 123.11 (2019), p. 111102. DOI: 10.1103/PhysRevLett.123.111102. arXiv: 1905.00869 [gr-qc].

[125] Harrison Siegel, Maximiliano Isi, and Will M. Farr. "Analyzing black-hole ringdowns. II. Data conditioning". In: *Phys. Rev. D* 111.4 (2025), p. 044070. DOI: 10.1103/PhysRevD.111.044070. arXiv: 2410.02704 [gr-qc].

[126] Hai-Tian Wang and Lijing Shao. "Effect of noise estimation in time-domain ringdown analysis: A case study with GW150914". In: *Phys. Rev. D* 108.12 (2023), p. 123018. DOI: 10.1103/PhysRevD.108.123018. arXiv: 2311.13300 [gr-qc].

[127] Maximiliano Isi and Will M. Farr. "Comment on "Analysis of Ringdown Overtones in GW150914"". In: *Phys. Rev. Lett.* 131.16 (2023), p. 169001. DOI: 10.1103/PhysRevLett.131.169001. arXiv: 2310.13869 [astro-ph.HE].

[128] R. Abbott et al. "Tests of general relativity with binary black holes from the second LIGO-Virgo gravitational-wave transient catalog". In: *Phys. Rev. D* 103.12 (2021), p. 122002. DOI: 10.1103/PhysRevD.103.122002. arXiv: 2010.14529 [gr-qc].

[129] R. Abbott et al. "Tests of General Relativity with GWTC-3". In: (Dec. 2021). arXiv: 2112.06861 [gr-qc].

[130] R. Abbott et al. "Properties and Astrophysical Implications of the 150 $M_\odot$ Binary Black Hole Merger GW190521". In: *Astrophys. J. Lett.* 900.1 (2020), p. L13. DOI: 10.3847/2041-8213/aba493. arXiv: 2009.01190 [astro-ph.HE].

[131] R. Abbott et al. "GW190521: A Binary Black Hole Merger with a Total Mass of $150M_\odot$". In: *Phys. Rev. Lett.* 125.10 (2020), p. 101102. DOI: 10.1103/PhysRevLett.125.101102. arXiv: 2009.01075 [gr-qc].

[132] Elisa Maggio et al. "Tests of general relativity in the nonlinear regime: A parametrized plunge-merger-ringdown gravitational waveform model". In: *Phys. Rev. D* 108.2 (2023), p. 024043. DOI: 10.1103/PhysRevD.108.024043. arXiv: 2212.09655 [gr-qc].

[133] Vasco Gennari, Gregorio Carullo, and Walter Del Pozzo. "Searching for ringdown higher modes with a numerical relativity-informed post-merger model". In: *Eur. Phys. J. C* 84.3 (2024), p. 233. DOI: 10.1140/epjc/s10052-024-12550-x. arXiv: 2312.12515 [gr-qc].

[134] Eliot Finch and Christopher J. Moore. "Frequency-domain analysis of black-hole ringdowns". In: *Phys. Rev. D* 104.12 (2021), p. 123034. DOI: 10.1103/PhysRevD.104.123034. arXiv: 2108.09344 [gr-qc].

[135] Collin D. Capano et al. "Multimode Quasinormal Spectrum from a Perturbed Black Hole". In: *Phys. Rev. Lett.* 131.22 (2023), p. 221402. DOI: 10.1103/PhysRevLett.131.221402. arXiv: 2105.05238 [gr-qc].

[136] C. V. Vishveshwara. "Stability of the Schwarzschild Metric". Ph.D. Thesis. PhD thesis. University of Maryland, College Park, 1970. URL: https://drum.lib.umd.edu/handle/1903/22447.

[137] C. T. Cunningham, R. H. Price, and V. Moncrief. "Radiation from collapsing relativistic stars. I - Linearized odd-parity radiation". In: *Astrophys. J.* 224 (1978), p. 643. DOI: 10.1086/156413.

[138] Halston Lim et al. "Exciting black hole modes via misaligned coalescences: II. The mode content of late-time coalescence waveforms". In: *Phys. Rev. D* 100.8 (2019), p. 084032. DOI: 10.1103/PhysRevD.100.084032. arXiv: 1901.05902 [gr-qc].

[139] Emanuele Berti, Vitor Cardoso, and Clifford M. Will. "On gravitational-wave spectroscopy of massive black holes with the space interferometer LISA". In: *Phys. Rev. D* 73 (2006), p. 064030. DOI: 10.1103/PhysRevD.73.064030. arXiv: gr-qc/0512160.

[140] Arnab Dhani. "Importance of mirror modes in binary black hole ringdown waveform". In: *Phys. Rev. D* 103.10 (2021), p. 104048. DOI: 10.1103/PhysRevD.103.104048. arXiv: 2010.08602 [gr-qc].

[141] Vishal Baibhav et al. "Agnostic black hole spectroscopy: Quasinormal mode content of numerical relativity waveforms and limits of validity of linear perturbation theory". In: *Phys. Rev. D* 108.10 (2023), p. 104020. DOI: 10.1103/PhysRevD.108.104020. arXiv: 2302.03050 [gr-qc].

[142] Xiang Li et al. "Angular emission patterns of remnant black holes". In: *Phys. Rev. D* 105.2 (2022), p. 024016. DOI: 10.1103/PhysRevD.105.024016. arXiv: 2110.03116 [gr-qc].

[143] Thibault Damour and Alessandro Nagar. "A new analytic representation of the ringdown waveform of coalescing spinning black hole binaries". In: *Phys. Rev. D* 90.2 (2014), p. 024054. DOI: 10.1103/PhysRevD.90.024054. arXiv: 1406.0401 [gr-qc].

[144] E. T. Jaynes. *Probability Theory: The Logic of Science*. CUP, 2003. ISBN: 978-0-521-59271-0.

[145] Niayesh Afshordi et al. "Waveform Modelling for the Laser Interferometer Space Antenna". In: (Nov. 2023). arXiv: 2311.01300 [gr-qc].

[146] Maximiliano Isi, Will M. Farr, and Katerina Chatziioannou. "Comparing Bayes factors and hierarchical inference for testing general relativity with gravitational waves". In: *Phys. Rev. D* 106.2 (2022), p. 024048. DOI: 10.1103/PhysRevD.106.024048. arXiv: 2204.10742 [gr-qc].

[147] James M. Dickey. "The Weighted Likelihood Estimation of Symmetric Distributions". In: *The Annals of Mathematical Statistics* 42.1 (1971), pp. 204–223. DOI: 10.1214/aoms/1177693506. URL: https://www.jstor.org/stable/2958475.

[148] Anuradha Gupta et al. "Possible causes of false general relativity violations in gravitational wave observations". In: (May 2024). DOI: 10.21468/SciPostPhysCommRep.5. arXiv: 2405.02197 [gr-qc].

[149] Jack Y. L. Kwok et al. "Investigation of the effects of non-Gaussian noise transients and their mitigation in parameterized gravitational-wave tests of general relativity". In: *Phys. Rev. D* 105.2 (2022), p. 024066. DOI: 10.1103/PhysRevD.105.024066. arXiv: 2109.07642 [gr-qc].

[150] Benjamin P Abbott et al. "A guide to LIGO–Virgo detector noise and extraction of transient gravitational-wave signals". In: *Class. Quant. Grav.* 37.5 (2020), p. 055002. DOI: 10.1088/1361-6382/ab685e. arXiv: 1908.11170 [gr-qc].

[151] A. G. Abac et al. "GWTC-4.0: Updating the Gravitational-Wave Transient Catalog with Observations from the First Part of the Fourth LIGO-Virgo-KAGRA Observing Run". In: (Aug. 2025). arXiv: 2508.18082 [gr-qc].

[152] Haowen Zhong et al. "Multidimensional hierarchical tests of general relativity with gravitational waves". In: *Phys. Rev. D* 110.4 (2024), p. 044053. DOI: 10.1103/PhysRevD.110.044053. arXiv: 2405.19556 [gr-qc].

[153] Abhirup Ghosh et al. "Testing general relativity using gravitational wave signals from the inspiral, merger and ringdown of binary black holes". In: *Class. Quantum Grav.* 35.1 (2018), p. 014002. DOI: 10.1088/1361-6382/aa972e. arXiv: 1704.06784 [gr-qc].

[154] Costantino Pacilio, Davide Gerosa, and Swetha Bhagwat. "Catalog variance of testing general relativity with gravitational-wave data". In: *Phys. Rev. D* 109.8 (2024), p. L081302. DOI: 10.1103/PhysRevD.109.L081302. arXiv: 2310.03811 [gr-qc].

[155] Emilio Bellini and Ignacy Sawicki. "Maximal freedom at minimum cost: linear large-scale structure in general modifications of gravity". In: *JCAP* 07 (2014), p. 050. DOI: 10.1088/1475-7516/2014/07/050. arXiv: 1404.3713 [astro-ph.CO].

[156] Emilio Bellini, Raul Jimenez, and Licia Verde. "Signatures of Horndeski gravity on the Dark Matter Bispectrum". In: *JCAP* 05 (2015), p. 057. DOI: 10.1088/1475-7516/2015/05/057. arXiv: 1504.04341 [astro-ph.CO].

[157] Emilio Bellini et al. "Constraints on deviations from ΛCDM within Horndeski gravity". In: *JCAP* 02 (2016). [Erratum: JCAP 06, E01 (2016)], p. 053. DOI: 10.1088/1475-7516/2016/06/E01. arXiv: 1509.07816 [astro-ph.CO].

[158] David Alonso et al. "Observational future of cosmological scalar-tensor theories". In: *Phys. Rev. D* 95.6 (2017), p. 063502. DOI: 10.1103/PhysRevD.95.063502. arXiv: 1610.09290 [astro-ph.CO].

[159] S. Mastrogiovanni, D. Steer, and M. Barsuglia. "Probing modified gravity theories and cosmology using gravitational-waves and associated electromagnetic counterparts". In: *Phys. Rev. D* 102.4 (2020), p. 044009. DOI: 10.1103/PhysRevD.102.044009. arXiv: 2004.01632 [gr-qc].

[160] Eric V. Linder. "Challenges in connecting modified gravity theory and observations". In: *Phys. Rev. D* 95.2 (2017), p. 023518. DOI: 10.1103/PhysRevD.95.023518. arXiv: 1607.03113 [astro-ph.CO].

[161] S. Mastrogiovanni et al. "Gravitational wave friction in light of GW170817 and GW190521". In: *JCAP* 02 (2021), p. 043. DOI: 10.1088/1475-7516/2021/02/043. arXiv: 2010.04047 [gr-qc].

[162] Macarena Lagos et al. "Standard sirens with a running Planck mass". In: *Phys. Rev. D* 99.8 (2019), p. 083504. DOI: 10.1103/PhysRevD.99.083504. arXiv: 1901.03321 [astro-ph.CO].

[163] G. R. Dvali, Gregory Gabadadze, and Massimo Porrati. "4-D gravity on a brane in 5-D Minkowski space". In: *Phys. Lett. B* 485 (2000), pp. 208–214. DOI: 10.1016/S0370-2693(00)00669-9. arXiv: hep-th/0005016.

[164] Cedric Deffayet and Kristen Menou. "Probing Gravity with Spacetime Sirens". In: *Astrophys. J. Lett.* 668 (2007), pp. L143–L146. DOI: 10.1086/522931. arXiv: 0709.0003 [astro-ph].

[165] Maxence Corman et al. "Constraining cosmological extra dimensions with gravitational wave standard sirens: From theory to current and future multimessenger observations". In: *Phys. Rev. D* 105.6 (2022), p. 064061. DOI: 10.1103/PhysRevD.105.064061. arXiv: 2109.08748 [gr-qc].

[166] Colm Talbot and Eric Thrane. "Measuring the binary black hole mass spectrum with an astrophysically motivated parameterization". In: *Astrophys. J.* 856.2 (2018), p. 173. DOI: 10.3847/1538-4357/aab34c. arXiv: 1801.02699 [astro-ph.HE].

[167] R. Abbott et al. "Population of Merging Compact Binaries Inferred Using Gravitational Waves through GWTC-3". In: *Phys. Rev. X* 13.1 (2023), p. 011048. DOI: 10.1103/PhysRevX.13.011048. arXiv: 2111.03634 [astro-ph.HE].

[168] A. G. Abac et al. “GWTC-4.0: Constraints on the Cosmic Expansion Rate and Modified Gravitational-wave Propagation”. In: (Sept. 2025). arXiv: 2509.04348 [astro-ph.CO].

[169] G. Dálya et al. “GLADE+ : an extended galaxy catalogue for multimessenger searches with advanced gravitational-wave detectors”. In: *Mon. Not. Roy. Astron. Soc.* 514.1 (2022), pp. 1403–1411. DOI: 10.1093/mnras/stac1443. arXiv: 2110.06184 [astro-ph.CO].

[170] Piero Madau and Mark Dickinson. “Cosmic Star-Formation History”. In: 52 (Aug. 2014), pp. 415–486. DOI: 10.1146/annurev-astro-081811-125615. arXiv: 1403.0007 [astro-ph.CO].

List of Figures

This page intentionally left blank.

List of Tables

This page intentionally left blank.

This page intentionally left blank.